

12-19-2022

Application of Distributed Fiber-optic Sensing for Pressure Predictions and Multiphase Flow Characterization

Gerald Kelechi Ekechukwu

Louisiana State University and Agricultural and Mechanical College

Follow this and additional works at: https://repository.lsu.edu/gradschool_dissertations



Part of the [Applied Statistics Commons](#), [Data Science Commons](#), [Petroleum Engineering Commons](#), and the [Signal Processing Commons](#)

Recommended Citation

Ekechukwu, Gerald Kelechi, "Application of Distributed Fiber-optic Sensing for Pressure Predictions and Multiphase Flow Characterization" (2022). *LSU Doctoral Dissertations*. 6029.

https://repository.lsu.edu/gradschool_dissertations/6029

This Dissertation is brought to you for free and open access by the Graduate School at LSU Scholarly Repository. It has been accepted for inclusion in LSU Doctoral Dissertations by an authorized graduate school editor of LSU Scholarly Repository. For more information, please contact gradetd@lsu.edu.

APPLICATION OF DISTRIBUTED FIBER-OPTIC SENSING FOR PRESSURE PREDICTIONS AND MULTIPHASE FLOW CHARACTERIZATION

A Dissertation

Submitted to the Graduate Faculty of the
Louisiana State University and
Agricultural and Mechanical College
in partial fulfillment of the
requirements for the degree of
Doctor of Philosophy

in

The Craft and Hawkins Department of Petroleum Engineering

by
Gerald Kelechi Ekechukwu
B.Sc., University of Ibadan, 2014
M.S., Imperial College London, 2017
May 2023

To my Parents, Gregory Ekechukwu and Salome Ekechukwu, my dear wife Vivian Ekechukwu, my adorable daughters Amanda and Nora Ekechukwu, my brother and sisters and my in-laws for their absolute love and support all through the years till today. I would not be able to accomplish this great achievement without them.

Acknowledgments

I am grateful to the Almighty God for my journey in life and for being the best Potter ever. I want to express my gratitude to my advisor, Dr. Jyotsna Sharma, for allowing me to join her research team at LSU. I am honored to have her as an advisor. Her encouragement, patience, and support were instrumental in my research journey and are highly appreciated.

I appreciate Dr. Tyagi, Dr. Chen, Dr. Wu, and Dr. Bulut for serving on my graduate committee. Their time, recommendations and constructive feedback regarding my doctoral project are valued. I'd also like to thank Ms. Janet Dugas and Mrs. Andi Donmyer for their administrative and technical support. Special thanks to my parents, Mr. and Mrs. Ekechukwu; my sisters, Rosemary and Lilian and Brother Josey, for their support and strong believe in me. My family's unwavering love and determination to provide me with a good education were critical to my success and are greatly appreciated. I am eternally grateful to my dear wife, Vivian, for her love and unwavering support. I am grateful to have had her along for this journey and to have shared so many wonderful experiences with her. Special thanks to my kids, Amanda and Nora; their presence during this doctoral journey helped keep me calm and brought numerous cherished smiles.

I am appreciative to my research group members – Temitayo Adeyemi, Rishikesh Shetty and Dr. J. Tabjula and all my great friends that were a part of my support system during my doctoral journey.

Table of Contents

Acknowledgments.....	iii
Abstract.....	vi
Chapter 1. Introduction.....	1
1.1. Background.....	1
1.2. Applications of DFOS in the Oil and Gas Industry.....	8
1.3. Test Well Description.....	8
1.4. Aims and Objectives of this Research.....	9
Chapter 2. Distributed Pressure Sensing.....	13
2.1. Introduction.....	13
2.2. Background.....	13
2.3. Methodology.....	19
2.4. Results.....	25
2.5. Summary.....	28
Chapter 3. Automated Detection and Quantification of Gas Influx Velocity.....	30
3.1. Introduction.....	30
3.2. Methodology.....	30
3.3. Results.....	33
3.4. Summary.....	35
Chapter 4. Interface Tracking and Estimation of Gas Fraction Using Distributed Fiber-Optic Sensor and Downhole Pressure Data.....	36
4.1. Introduction.....	36
4.2. Methodology.....	37
4.3. Results.....	45
4.4. Summary.....	57
Chapter 5. Fiber Degradation Analysis and SNR Estimation.....	61
5.1. Introduction.....	61
5.2. Fiber Degradation Analysis Methodology.....	70
5.3. Fiber Degradation Analysis Results and Discussion.....	74
5.4. Signal-to-Noise (SNR) Estimation.....	88
5.5. Summary.....	91
Chapter 6. Conclusions and Recommendations for Future Work.....	94
6.1. Summary.....	94
6.2. Recommendations for Future Work.....	96
Appendix. Copyright Information.....	98
A.1. Scientific Reports Journal Copyright.....	98
A.2. Optical Publishing group Copyright Information.....	99

A.3. Journal of Petroleum Science and Engineering Copyright Information	100
References.....	101
Vita.....	109

Abstract

In the oil and gas industry, distributed fiber optics sensing (DFOS) has the potential to revolutionize well and reservoir surveillance applications. Using fiber optic sensors is becoming increasingly common because of its chemically passive and non-magnetic interference properties, the possibility of flexible installations that could be behind the casing, on the tubing, or run-on wireline, as well as the potential for densely distributed measurements along the entire length of the fiber. The main objectives of my research are to develop and demonstrate novel signal processing and machine learning computational techniques and workflows on DFOS data for a variety of petroleum engineering applications. This includes distributed pressure sensing using distributed temperature sensor (DTS) and distributed acoustic sensor (DAS) data, automated gas rise velocity detection, multiphase flow characterization, and fluid interface detection. The information obtained with DFOS installed in oil and gas wells contributes to improved efficiency, safety, and ultimate recovery.

In this study, fiber-optic DAS and DTS data are applied for the first time on a big scale to predict pressure. The data pattern was characterized using a combination of machine-learning and signal processing approach, and the created model was subsequently applied to anticipate pressure data at various depths. Additionally, it was shown how low-frequency DAS and DTS might be utilized to track distributed pressure on a well-scale. In addition, a novel methodology was developed to automatically estimate the real-time gas influx velocity into a wellbore, which offers a significant improvement over current approaches in which the gas velocity is largely identified by surface-based methods that suffer from time-delay issues. Furthermore, two independent techniques (velocity band energy plus downhole pressure data and speed of sound) were used to estimate the gas void fraction. Gas void fraction is critical for flow characterization in different

calculations such as two-phase viscosity, density, and pressure drop. A new analysis workflow is presented to delineate the gas-liquid interface in the presence of background noise caused by pump vibrations. Lastly, the effect of optical losses, fiber degradation, and noise on DFOS data quality are evaluated and quantified. In the final chapter of this dissertation, the overall findings of my work are summarized, and recommendations for future work are presented. The workflows and methods presented in this research will be beneficial to improve and validate fiber-optics-based interpretations and applications in petroleum engineering applications, including pressure prediction, flow characterization, and automated detection.

Chapter 1. Introduction

Fiber-optic sensors have the potential to be a game-changer in well and reservoir surveillance applications in the oil and gas industry. The chemically passive and non-magnetic interference nature of fiber-optic sensors, the potential for versatile installations that could be behind the casing, on the tubing, or a wireline, as well as the possibility of densely distributed measurements along the entire length of the fiber, are all reasons for using this increasingly popular technology. Information obtained from distributed fiber-optic sensors installed in oil and gas wells contributes to improving efficiency, safety, and ultimate recovery. In this chapter, a brief overview and working principle of fiber-optic sensor technology and typical optical cable design configuration are presented. The common acquisition data file type, as well as the main data pre-processing steps are briefly discussed, some of which are common to all chapters. The current applications of DFOS in the oil and gas industry are also mentioned. Lastly, the objectives of this research, as well as the general structure of this dissertation, are outlined.

1.1. Background

1.1.1. An Overview of Fiber-Optic Sensor Technology

Numerous fiber-optic sensing systems have been developed and commercially demonstrated over time. As shown in Figure 1, they can be divided into three main categories: interferometric sensors, grating-based sensors, and distributed sensors [1], [2]. Interferometric sensors work by inserting an intrinsic or extrinsic interferometric cavity along an optical channel [3]. Physical changes in the medium are reflected in changes in the optical phase difference between two interference light waves. Two well-known and practical interferometric sensors are Fabry-Perot interferometric sensors [3] and low-coherent interferometric sensors (SOFOTM interferometric sensors) [4]. It is

worth mentioning, though, those interferometric sensors are typically pointed sensors that can be multiplexed.

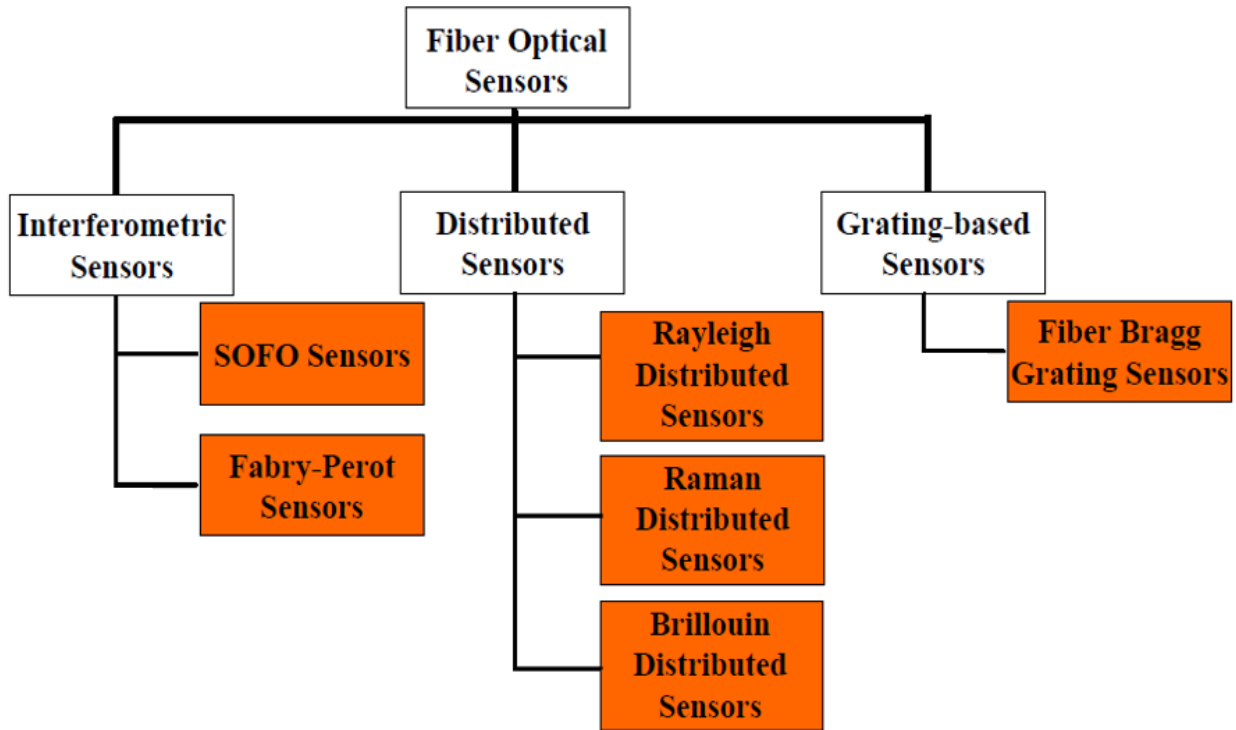


Figure 1. An overview of popular fiber-optics sensing technologies.

Fiber Bragg grating (FBG) sensors are the most well-established grating-based sensors with a wide range of applications [5]. An FBG sensor reflects a portion of the incoming light of a specific wavelength, known as the Bragg wavelength while allowing the rest of the incoming light to pass through unaffected. The Bragg wavelength is determined by the fiber's refractive index and grating pitch, which are both impacted by external factors such as vibration, strain, temperature, and other variables. Several measurands can be monitored with FBG sensors by observing the shift in Bragg wavelength. Multiplexing of FBGs via wavelength division multiplexing or time division multiplying could result in measuring the measurands at multiple points. However, to obtain a continuous high spatial resolution of the measurand, fully distributed sensors need to be used for

many applications. Since this research will be focused on distributed sensors, this technology is described in more detail in the following sections.

1.1.2. Distributed Fiber-Optic Sensing Technology Description

1.1.2.1. Signal Propagation in Optical Fibers

Distributed fiber-optics sensing (DFOS) is a cutting-edge non-invasive real-time sensing system that may convert data or measurements from the physical world, such as temperature, flow, pressure, or strain, into electronic signals [6]. In DFOS, the optical fibers serve as both the sensing component and the mode of conveyance for optical signals. They use optical time-domain reflectometry (OTDR), which utilizes the time-of-flight of the light to determine the location of the target measurand [7].

In the OTDR method, a series of short pulses of highly intense light/laser are launched into the fiber, causing interactions with the inherently non-homogenous sections of the crystalline core of the fiber-optic cable, sending backscattered light to the surface-located interrogation unit. These molecule-level heterogeneities occur intrinsically and inadvertently during the manufacturing of the fiber, resulting in a non-uniform refractive index distribution in the fiber. The fiber sections with refractive indices that deviate from the mean could be called scattering spots. The interactions of the light with the scattering regions along the fiber-optic core detect thermal, vibration, and pressure variations and disturbances resulting from activities near the fiber-optic cable.

In addition to the scattering loss, light may also be attenuated by absorption mechanisms along the fiber cable. These are electronic absorption ultraviolet (UV) bands that occur around 100 nm and molecular absorptions of mid-range infrared (IR) bands. Both the UV and IR absorption bands have tails that stretch into the visible light portion of the electromagnetic (EM) spectrum.

The power of the backscattered signal (P_{BS}) that is received at time $t = 2z/v_g$ at a distance z from the launching end can be calculated as [6], [8]:

$$P_{BS} = \frac{1}{2} C \times \alpha_s \times v_g \times \tau \times P_i \times e^{-2\alpha t} \quad 1.1$$

Where C is the capture coefficient, which is the fraction of the forward-moving ray that is returned during backscattering, α_s is the Rayleigh scattering coefficient, v_g is the group velocity in the fiber, P_i is the input power, α is the fiber loss coefficient, τ is the pulse width. The Rayleigh scattering coefficient is proportional to the inverse fourth power of wavelength, and in pure silica, its value is about $0.7 \text{ dB km}^{-1} \mu\text{m}^{-4}$. Therefore, at $1 \mu\text{m}$ for every meter of fiber that the light travels through, about 0.016% of the incident light is lost.

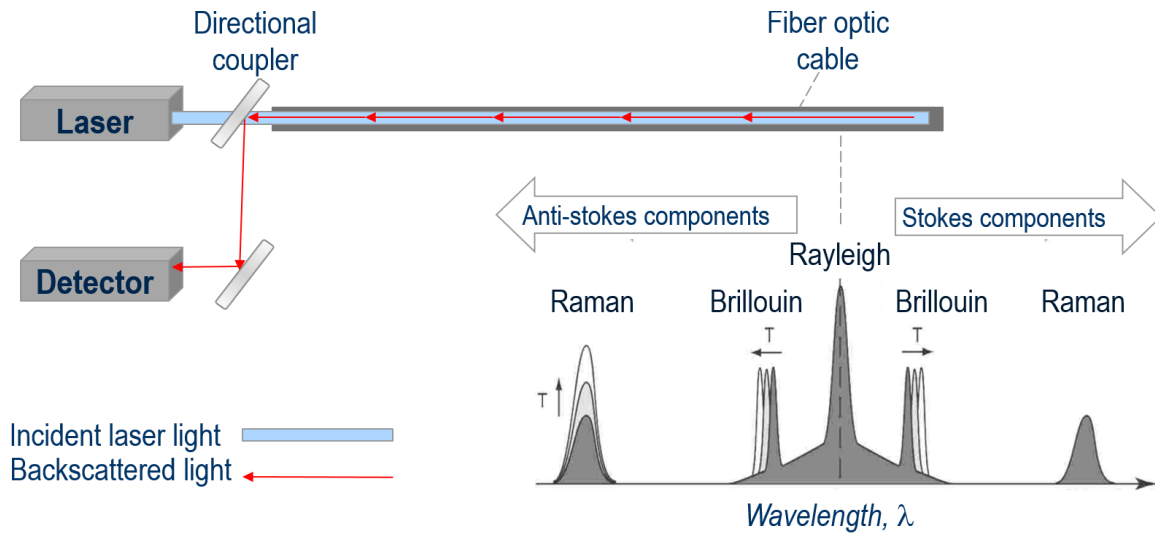


Figure 2. Schematic of a typical DFOS acquisition and the backscattered light spectrum.

Rayleigh, Brillouin, and Raman components make up the spectrum of backscattered signals (Figure 2). The backscattered Raman component is typically used in the distributed temperature sensor (DTS) to measure temperature. The intensity ratio between the two Raman scattering wavelength ranges, one of which is temperature-dependent (anti-Stokes) and the other not (Stokes), is used to calculate the temperature. Distributed acoustic sensors (DAS) use the phase

shifts of the backscattered Rayleigh component, which has the same wavelength as the incident light, to measure vibrations, while the Brillouin component is used by Distributed Strain Sensors (DSS) to measure strain. [6], [9].

The fiber-optic cable is the transmission medium or waveguide for the light wave being propagated. The complete fiber cable that is ready for deployment usually contains at least the core, cladding, buffer, and jacket, as shown in Figure 3. Optical fiber coatings/buffers protect the glass fiber from mechanical and environmental stresses during different applications. The primary coating may be applied in a single or dual layer. Common coating materials are acrylate, silicone, polyetheretherketone (PEEK), and other popular polymers. There are two main types of fiber-optic cables single-mode and multimode. As shown in Figure 4, the single-mode fibers have very thin cores that cause the light to travel as a single ray. The multimode fibers, on the other hand, have larger diameters resulting in many different ray paths. The number of modes that are guided through the cable is related to a parameter called normalized frequency, V , which is related to the core radius a , the laser wavelength λ , and the numerical aperture (NA). The NA is related to the refractive indices of the core and cladding and is usually 0.2 or more [6]. The typical optical wavelength used in a single-mode core of 8 μm is around 1550 nm, whereas multi-mode fibers have typical core diameters of 50 or 62.5 μm , and wavelengths between 850 and 1300 nm are typically used. The number of guided modes is $V^2/4$ for graded-index fiber [10]. Furthermore, a thin fiber (8 μm diameter) that supports single-mode transmission at wavelengths above 1250 nm can also support multiple modes at shorter wavelengths.

$$V = \frac{2\pi}{\lambda} \cdot a \cdot NA \quad 1.2a$$

$$NA = \sqrt{n_1^2 - n_2^2} \quad 1.2b$$

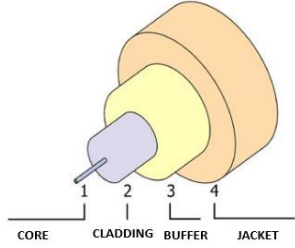


Figure 3. Optical fiber structure [6].

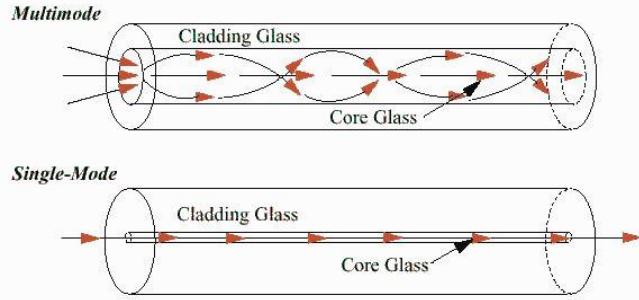


Figure 4. Schematics of multimode vs. single-mode fibers [6].

1.1.2.2. Fiber-optics Data Representation and Pre-processing.

The raw DAS data that is received from the service acquisition company is usually in the SEG-Y or hdf5 format. Both formats contain textual file headers, tape headers, and binary headers in addition to the trace numerical data. The time-series DAS vibration data are extracted in the form of a 2-dimensional time-depth matrix. One trace (each column of the matrix) corresponds to a single laser pulse traveling down the fiber cable in the well and back to the surface. Hence, sufficient time must be allowed for the pulse to travel and return to the surface before the next pulse is transmitted. This time interval is generally referred to as the sample interval or the sampling period. The inverse of which is referred to as the sampling frequency. The Shannon-Nyquist [11] criterion requires that the sampling frequency is at least two times that of the maximum frequency expected in our signal. The DAS data analyzed in this research was acquired at 10 kHz, thus the maximum signal frequency that can be analyzed is 5 kHz and the sampling interval is 100 μ s. The spatial samples typically correspond to the rows of the 2D matrix and a specific depth along the wellbore. Furthermore, the spatial resolution is the distance occupied by the pulse as it travels along the fiber. For example, a 10-ns pulse of light traveling at 0.2m/ns has a spatial resolution of 1 m. Spatial resolution, Δz , of the measurement can be expressed as:

$$\Delta z = \frac{1}{2n_g} c\tau_p \quad 1.3$$

Where c is the light propagation speed in the fiber, n_g is the group refractive index, τ_p is the pulse width. In the DAS data used in this study, the size of one SEG-Y file containing 10 s of data is about 920 MB. The full experimental matrix is formed by concatenating data from all SEG-Y files corresponding to the times of interest. As a result, the data size is quite huge, necessitating data compression. The well-known Fourier transform is then used to compress the row data, representing each depth, by keeping the most crucial Fourier coefficients. The process called “frequency band energy” (FBE) computation involves isolating the different frequencies in the data, which can then be processed in frequency bands. For all bands, the FBE file generated per record length (10 s) reduces the size from 920 MB to roughly 90 KB. Mathematically, this FBE conversion can be described as shown in equation 1.4 below [12]:

$$FBE_k(b, d) = \frac{2}{N_{FFT}} \times \sum_{f=f_2(b)}^{f=f_1(b)} |X(f, d)|^2 \quad 1.4$$

Where $X(f, d)$ is the FFT of the vibration data $x(t, d)$, $f_1(b)$ and $f_2(b)$ are respectively the lower and upper bounds of a pre-determined frequency band b , k is an integer used to differentiate the different bands considered, while N_{FFT} is the number of samples in the recording length.

1.1.2.3. Characteristics and Benefits of DFOS

A. Fiber-optic sensors offer many advantages compared to conventional gauges and offer higher reliability for long-term deployment. They are [6], [13], [14]:

- a. chemically passive,
- b. electrically insulating,
- c. immune to corrosion,
- d. able to withstand high temperature and pressure conditions,
- e. non-intrusive (due to small fiber diameter),

f. fast and more sensitive since they use light to convey information.

g. not sensitive nor cause electro-magnetic interference.

B. In addition to the above benefits, DFOS gives a high resolution of spatiotemporal data, which helps to detect and solve many problems in the oil and gas industry. This is because the entire fiber is a sensor; hence dynamic effects along the fiber can be seen.

1.2. Applications of DFOS in the Oil and Gas Industry

The different sectors of the oil and gas industry (upstream, midstream, and downstream) have implemented DFOS for a variety of applications. Pipeline inspection and process monitoring are the main applications of DFOS in the midstream and downstream sectors. Most of the applications are, however in the upstream industry. The very first use case of the technology was the use of DTS for in-well monitoring in the early 1980s [15]. In recent times, the use of changes in the thermal profile obtained using DTS has been increasing rapidly in both the oil and gas as well as geothermal energy applications. The first application of DAS was completed in Canada in 2009 for fracture monitoring [16]. Since then, several new applications have been added to the growing portfolio of DAS. This includes, fluid flow metering and calculation of in-situ phase fractions ([17]–[20], hydraulic fracture propagation monitoring [21]–[25], vertical seismic profiling (VSP) and detecting microseismic activity [26]–[29], electrical submersible pump performance surveillance [30], tubular and pipeline leak detection [31], [32], high pressure/temperature and geothermal applications [33], and gas-lift and wax deposition monitoring [34].

1.3. Test Well Description

The test well utilized in this study is located at the Petroleum Engineering Research, Training, and Testing (PERTT) lab facility at Louisiana State University. It consists of a 9-5/8 in. casing and a 2-7/8 in. production tubing, as shown in the schematic in Figure 5. In 2019, a DFOS control line

with pumped single-mode and multimode fibers for measuring DAS and DTS, respectively, was clamped to the outside of the 5025-ft-long production tubing. Both the single- and multimode fibers were pumped into the ¼” DFOS tube with 99.9% isopropyl alcohol (IPA) and then purged over 48 hours with nitrogen, before installation in the well. Table 1 summarizes the fiber specifications. Four downhole pressure and temperature gauges were also installed at 487 ft, 2023 ft, 3502 ft, and 5024 ft for measurements in the annular region. Since the DFOS installation in 2019, the wellbore has been exposed to different fluids such as water, nitrogen gas, and drilling mud. Several experiments using this setup have been performed since then. The maximum temperatures and pressures that have been recorded in the well are 130 °F and 3500 psi, respectively. In a static water column inside the test well, the geothermal gradient is 1.24 °F /100 ft (or 0.689 °C /100 ft) while the hydrostatic gradient is 0.43 psi/ft. The DTS acquired in the well utilizes the Raman backscatter component to estimate the distributed temperature profile, while the DAS utilized in this study is based on the Rayleigh backscattered light.

1.4. Aims and Objectives of this Research

The main objectives of this research are to implement techniques and workflows for distributed pressure sensing and multiphase flow characterization using DFOS data. More specifically, the objectives include:

Objective 1: To estimate distributed pressure from DAS and DTS data using a combination of machine learning and signal processing approach. Giallorenzi et al. [35] were the first to stipulate the idea of the frequency dependence of the elastic properties of the optical fiber. More recently, Becker et al. [33] observed experimentally the variation in pressure sensitivity with the frequency of the signals detected. Hence, we first needed to confirm that such dependency exists on a larger,

more representative scale and then propose a workflow on how to predict pressures based on our findings.

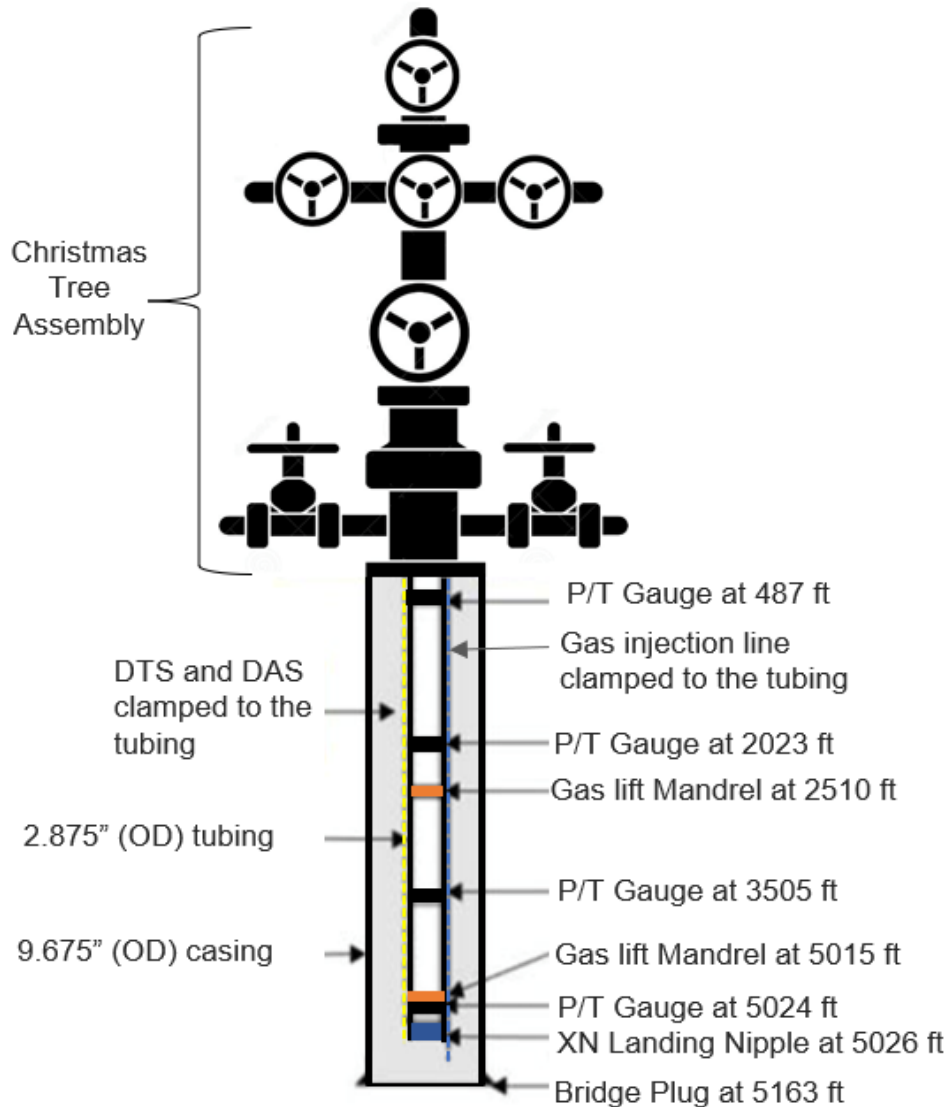


Figure 5. Test-well schematic showing the downhole instrumentations.

Objective 2: Develop automated workflows for gas influx detection and velocity estimation

Conventional gas-kick detection and monitoring generally suffer from time delay in the response between the occurrence of keep in the subsurface and its detection using surface-based techniques. This delay could lead to the loss of lives, massive investments, and environmental pollution; hence

the early detection of gas influx is crucial. This warranted us to seek solutions to help alleviate this problem. We present a novel workflow for the automated detection of gas-kick and estimation of the gas influx velocity using the real-time DAS data from the test wellbore used in this study.

Objective 3: Estimation of gas void fraction and detection of fluid interfaces using the pressure-difference method, speed of sound estimation, and velocity band energy methods

Understanding the exact location of the interface of fluids and, in effect, the gas slug height along a well is very important for several applications such as flow monitoring, gas influx detection, gas-oil contact determination for reserves estimation, gas lift operation optimization, and other remedial operations. The speed of sound changes depending on the composition and nature of the fluids through which the sound wave is traveling. This fundamental phenomenon is leveraged in the calculation of void fraction. In addition, we investigate the possibility of using an algorithm involving advanced signal processing and filtering steps to delineate the gas-liquid interface in the wellbore.

Objective 4: Fiber degradation analysis and signal-to-noise (SNR) estimation

The ability of the DFOS to provide accurate and repeatable information depends on the quality of the signal returning from the point of interest, optical losses, and the system noise. Thus, it is necessary to evaluate these effects periodically to ensure high-DFOS data quality and the ability to detect the signal of interest. The SNR is estimated on well-scale experimental data to monitor the displacement of a gas slug (gas-liquid mixture region) in a wellbore. Since the vibration and temperature changes introduced by the slow-moving gas bubbles in a circulating column are often very small, the optical losses, fiber degradation, and noise can impede our ability to detect gas in a circulating fluid, such as during gas-in-riser monitoring. These effects are analyzed qualitatively and quantitatively.

1.4.1. Dissertation Structure

This dissertation is organized into self-contained chapters. The common background material for all chapters is provided in Chapter 1. Additional and more specific background is provided in each subsequent chapter.

- In Chapter 2, titled “Distributed Pressure Sensing Using DTS And DAS” the objective-1 of the dissertations is addressed in detail.
- In Chapter 3, titled “Automated Detection and Quantification of Gas Influx Velocity in Wellbore from Fiber-Optic Sensor Data”, objective-2 is addressed in detail.
- In Chapter 4, titled “Interface Tracking and Estimation of Gas Fraction Using Fiber-optic and Pressure Data estimation of gas fractions and liquid holdups” the objective-3 is addressed.
- In Chapter 5, “Fiber degradation and SNR Estimation” objective-4 analysis is addressed.
- In Chapter 6, titled “Conclusions and Recommendations for Future Work”, the main conclusions based of this doctoral research and recommendations for future work are presented.

Chapter 2. Distributed Pressure Sensing

2.1. Introduction

Over the past few years, the oil and gas industry has seen a rapid increase in the deployment of DFOS, particularly DTS and DAS. However, the use of DTS and DAS to estimate distributed pressure has not been demonstrated and is the first objective of this doctoral study. Furthermore, an extensive literature review conducted as part of this study appears to indicate that, currently, most of the major oilfield service companies do not offer a commercially available distributed pressure measurement capability. While there is evidence of ongoing research in this area, examples of commercially successful applications of the technology were not readily found. In this chapter*, a well-scale demonstration of a detailed workflow that aims to predict pressures from DAS and DTS is presented.

2.2. Background

2.2.1. Rayleigh-Based Distributed Pressure Sensing

As briefly described earlier, an OTDR device measures the photocurrent of the detector generated by the optical signal arriving at the detector at the sampling time. The optical signal that is received by the detector is defined by the electric field of the optical wave that results from the continuous backscattering of the probe pulse as it propagates along the fiber cable. It can be characterized by the following phasor [8]:

$$\dot{E}(\tau) = A(\tau)e^{j\phi(\tau)} = |\dot{E}(\tau)| \cdot \exp\{j \cdot \arg[\dot{E}(\tau)]\} \quad 2.1$$

*Most of this chapter was previously published Ekechukwu, G.K., Sharma, J. Well-scale demonstration of distributed pressure sensing using fiber-optic DAS and DTS. *Sci Rep* 11, 12505 (2021). <https://doi.org/10.1038/s41598-021-91916-7>

Where $\vec{E}(\tau)$ is the electric field of the optical wave, τ is the two-way time of flight of the probe pulse, $A(\tau)$ is the amplitude, $\phi(\tau)$ the phase and $j = \sqrt{-1}$. Based on the sensing mechanism employed, Rayleigh-based techniques can be further classified into pressure-induced strain techniques and pressure-induced birefringence techniques. Birefringence is an optical property that is described by the presence of distinct refractive indices for two given orthogonally polarized light waves propagating in the fiber [6], [36]. A.J. Rogers [36], [37] was the first to propose the use of the polarization optical time-domain reflectometry (POTDR), which is the very first documented distributed optical fiber sensor ever proposed. The use of POTDR for pressure sensing is still an active area of research but here we would only discuss the pressure-induced strain in conventional fibers since that is the principle that was used in the method presented here. The following sets of equations describe the working principle of the pressure-induced strain in conventional fibers. When light travels through a fiber of length L and refractive index of n , the optical phase is given as:

$$\phi = nKL \quad 2.2a$$

where

$$K = 2\pi/\lambda \quad 2.2b$$

Direct pressure exposure induces changes in a phase differential which changes the properties of the optical fiber. The changes in the phase induce strain, modifies the index of refraction of the material (the photo-elasticity effect), and cause waveguide dispersion as shown below [38], [39]:

$$d\phi/\phi = dL/L + dn/n + dk/k \quad 2.3$$

Hocker [39] demonstrated that the third term, representing the consequence of mode dispersion, is insignificant. The delay in the phase due to the induced strain is shown below [35], [40].

$$\frac{d\phi}{\phi} = \varepsilon_{zg} - \frac{n^2}{2} [(P_{11} + P_{12})\varepsilon_{rg} + P_{12} \varepsilon_{zg}] \quad 2.4a$$

hence

$$d\phi/\phi = \xi\varepsilon_{zg} \quad 2.4b$$

where

$$\xi = 1 - \frac{n^2}{2} [P_{12} - v_g(P_{11} + P_{12})\varepsilon_{rg}] \quad 2.4c$$

Where P_i is the elasto-optic strain or Pockels coefficients, for silica, for example, $P_{12} = 0.27$, $P_{11} = 0.12$, $\xi = 0.79$ at typical wavelengths used in Rayleigh scattering.

Hence,

$$d\phi = 2\pi n L \xi \varepsilon_{zg} / \lambda \quad 2.5$$

Accounting for the double transit ($L = 2G$) and rearranged to show the strain sensitivity below [41]:

$$\varepsilon_{zg} = \lambda d\phi / 4\pi n G \xi \quad 2.6$$

Budiansky [38] then added the following expression for pressure sensitivity as a result of the induced strain:

$$\varepsilon_{zg}/p = -\frac{1-2(1-f)v_p-2fv_g}{fE_g+(1-f)E_p} \quad 2.7$$

The expression has been deemed accurate for $f = (a/b)^2 \ll 1$. Where ε_{zg} is the axial component of the induced strain, a is the radius of the fiber, b is the radius of the coating, E_g and v_g are Young's modulus and Poisson ratio of the glass and E_p and v_p are Young's modulus and Poisson ratio of the polymer coating.

Rogers et al. [14] investigated the potential of Rayleigh-based distributed sensing systems in measuring pressure. In particular, he estimated that a pressure of approximately 0.1 MPa should produce a phase shift equivalent to $1\mu\varepsilon$. Becker et al. [33] evaluated the use of Rayleigh-based fiber-optic DAS to measure the oscillatory strain rate along a standard fiber-optic cable caused by pressure waves at mHz-frequencies. Ultimately, the tests showed that this approach works for hydrostatic pressure waves with short oscillation periods (< 10 s). Schenato et al. [42] proposed a highly sensitive distributed pressure-sensing cable that employs standard single-mode fibers. The cross-section of the cable has two arched meandering rubber profiles that enclose an elastic band

embedding the fiber. The pressure sensitivity and spatial response of the cable were characterized by a commercial optical frequency domain reflectometer (OFDR). In particular, the cable showed an intrinsic spatial resolution of about 8.5 cm, with a mean sensitivity of -30 GHz/kPa. The spectral shift resolution and corresponding pressure resolution were 150 MHz and approximately 5 Pa respectively, while the root-mean-square accuracy was limited to 5 hPa, mainly due to cable manufacturing imperfections.

One of the major shortcomings of almost all the experimentally tested optical fibers, especially those used in the POTDR, is that they were performed on bare fiber cables. These bare fibers are not suitable for field deployment, and they need to be coated with single or multi-layers of cladding, depending on the applications. Besides, the effect of the external signal frequency on pressure sensitivity has not been deeply explored. We intend to explore this dependence in greater detail. Lastly, despite the huge benefits of Rayleigh-based distributed sensing, its use poses some unique challenges, in particular, how to handle the vast amount of data generated (several GBs per minute) in a multi-km deep wellbore. This data volume must be managed effectively to extract the information needed in a timely manner. Hence, also in this work, an integrated approach that involves spectral decomposition and other signal processing techniques will be used first to compress the data and then to extract meaningful information that could be applied for real-time field operations monitoring and decision-making. Before discussing our computational approach to Distributed Pressure Sensing (DPS), we first discuss the applications of pressure measurement in the oil industry.

2.2.2. Potential Applications of DPS in Petroleum Engineering

The pressure acquired by DPS can be used for a variety of oil and gas applications. It is worth noting that DPS data not only provides an equivalent benefit to those of currently used single-point

pressure gauges, but it provides a plethora of applications in which the dense spatial data can be used; some of these applications are highlighted briefly below.

1. Inflow Performance Estimation:

The Productivity Index (PI or J) is a measure of the ability of a well to produce. It is the ratio of the liquid flow rate to the pressure drawdown defined below [43], [44]:

$$PI = \frac{q_o}{P_R - P_{wf}} = \frac{q_o}{\Delta P} \quad 2.8$$

For performance analysis of oil wells, engineers often assume that the flow rate is directly proportional to pressure drawdown. It is a reliable indication of the well productive capacity only if the well is produced during a pseudo-steady-state flow regime.

2. Pressure Transient Analysis:

$$P_{wf}(t) = P_i - \frac{162.6q\mu B}{kh} \left[\log \left(\frac{kt}{\phi\mu c_t r_w^2} \right) - 3.23 - 0.87s \right] \quad 2.9$$

Simple equations allow us to estimate permeability and skin factor once the correct semi-log straight line is identified and its slope, m , is estimated. These equations apply to both drawdown and buildup tests. The following equations are used for oil wells [45]:

$$k = \frac{162.6qB\mu}{mh} \quad 2.10$$

$$s = 1.151 \left[\frac{\Delta p_{1hr}}{m} - \log \left(\frac{k}{\phi\mu c_t r_w^2} \right) + 3.23 \right] \quad 2.11$$

3. Artificial Lift Monitoring:

Artificial lift methods are usually applied to assist or supplement the natural reservoir pressures, which may no longer be sufficient to push the fluids in the well bore to the surface. This can be achieved using gas lifting, which involves reducing the density of the liquid in the well bore or using different varieties of submersible pumps. The accuracy of the

pressures in the pumps is very important for optimizing pump efficiencies [46]. Actual DPS data can be used to diagnose faulty gas lift valves as well as early indications of the need to service submersible pump motors. This is of extreme importance, especially with downhole water separation techniques for water coning solutions [47], [48] where complicated downhole completions and accurate distributed downhole pressures are needed.

4. Monitoring of Packer Integrity:

Production packers provide barriers that ensure the reservoir fluids pass through the tubing, completions fluid is not contamination and properly isolates different production zones. The ability to monitor the pressures around these packers can be used to measure the integrity of the packers [15]. The spatial pressure information will help to precisely identify the leak/failure points.

5. Interference Testing:

An adjacent wellbore's impact on another well within the field can be assessed through interference testing. During a conventional interference test process, the well is shut-in and given time to attain a stable pressure. The pressure within the shut-in wellbore would then be monitored while a nearby wellbore was injected with a fluid (water), to ascertain how long it would take for the shut-in well's pressure to be influenced.

6. Identification of oil-water, gas-water, and gas-oil contacts:

Distributed pressure sensing provides an opportunity for real-time monitoring of fluid contacts. DPS can provide value by reduction of production deferment – the use of real-time monitoring prevents the repeat of previous situations in which radiometric surveys missed the thinning and the lowering of the fluid contacts. [49]. Figure 6 shows a schematic of how this can be done.

7. Leak detection or gas ingress into the wellbore:

Gas leaks due to damaged casing and poor cementing jobs can also be detected by using the novel DPS technique proposed. Leaks lead to a decrease in pressure from what is expected and hence will be picked up by the DPS system.

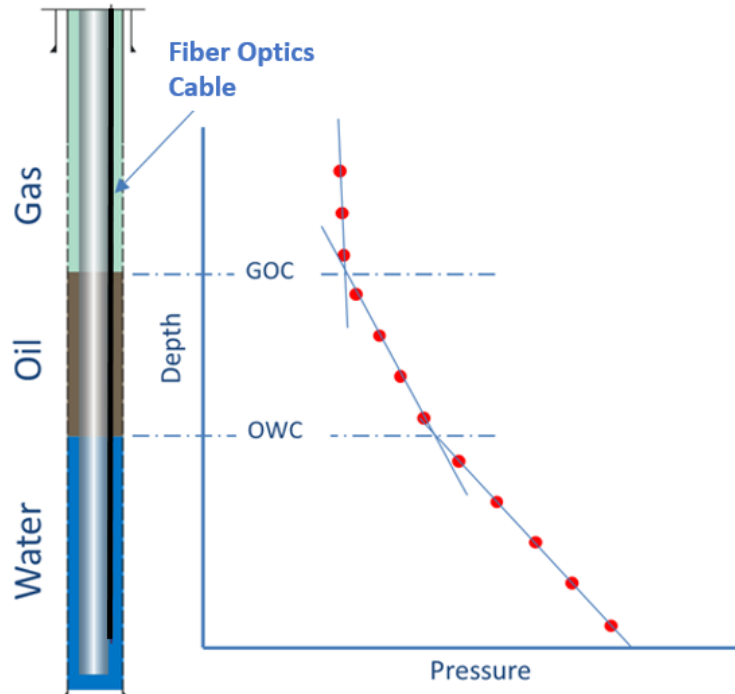


Figure 6. Distributed pressure sensing for oil-rim movement monitoring.

2.3. Methodology

Two-phase (water and nitrogen gas) flow studies were carried out in a test well described in section 1.3. Frequency band energy (FBE), also known as pre-specified frequency bands, are created by applying the fast Fourier transform to the acquired data (FBE), as mentioned earlier in section 1.1.2.2. This investigation looked at seven distinct frequency bands - Band-LF (0 to 2 Hz), Band-0 (2 to 5000 Hz), Band-1 (2 to 10 Hz), Band-2 (10 to 50 Hz), Band-3 (50 to 200 Hz), Band-4 (200 to 500 Hz), and Band-5 (500 to 1000 Hz). Our dataset contains little acoustic energy above 1000 Hz, so we have not analyzed these.

Using two separate experimental datasets, the suggested distributed pressure measuring methodology using DTS and DAS was shown in this chapter. In the first experiment (referred as Dataset #1), the wellbore was initially filled with water, and then a fixed volume of nitrogen gas was injected down the tubing and allowed to rise to the surface through the annulus. In the second experiment (referred here as Dataset #2), water is injected soon after the gas is injected to drive the gas down the tubing and eventually through the annulus and back to the surface. The datasets correspond to different gas injection volumes, water circulation rates, backpressure, and injection methods, as given in Table 1. Figure 7 displays the waterfall graphs for bands 0 and 1. Figure 8 and Figure 9, respectively, display the pressure and temperature readings for Datasets 1 and 2.

Table 1. Parameters used in the case study experiments

Dataset	Water Injection Rate [GPM]	Injected Gas Volume [BBL]	Injection Method	Backpressure [PSI]
1	0	2	Injection Line	Choke closed
2	100	5	Tubing	300

2.3.1. Analysis Workflow

The proposed analysis workflow developed in this study is illustrated in Figure 10 and described as follows [52] :

1) The data preparation step starts with time and depth matching the pressure gauge, DTS, and DAS data.

2) *Single-Depth Analysis*: The machine learning model is implemented separately at the four gauge depths (487 ft, 2023 ft, 3502 ft, and 5025 ft). The input parameters for the model at each depth are DAS (one frequency band at a time) and DTS data, and the desired output variable is the change in pressure relative to the initial pressure at the first time-step (P). For model training, 30% of the

data were picked at random, while the remaining 70% were used for blind testing. The performance of each frequency band is examined independently to select the best one for pressure prediction. This analysis is done for the two experimental datasets across all four gauge depths and seven frequency bands.

3) *DAS Frequency Band Selection*: The best-performing frequency band for each dataset is determined via a single-depth analysis for each of the four gauge positions. This frequency band is used in the distributed pressure analysis.

4) *Distributed Pressure Analysis*: The objective is to forecast pressure at various depths using DAS and DTS data. To estimate pressures at gauge depths other than those used for training, the machine learning model is first trained using data from any two gauge depths. The input features are DTS, DAS (only the frequency band chosen in (3)), and time, and the target predicted is a change in pressure (ΔP).

Preliminary Comparative Analysis.

A preliminary comparative analysis using different machine learning algorithms to select the most robust technique was conducted. The algorithms used to build different models are Random Forest (RF), gradient boosting (GB) [53], [54], extreme gradient booking (XGBoost) [55], support vector regression (SVR) [56], [57] and different architectures of shallow ANN [58], [59]. Figure 11 shows a summary of the performance of the models. The values shown are the mean values across the four gauge depths using the DAS Band-LF (0 to 2 Hz) for Dataset 2. The Random Forest model (Figure 12) used in the main body of work consistently showed similar or better performance (i.e., high R^2 and low RMSE) compared to the other techniques investigated in all seven frequency bands analyzed in both datasets. The architecture of all the models used in the preliminary analysis

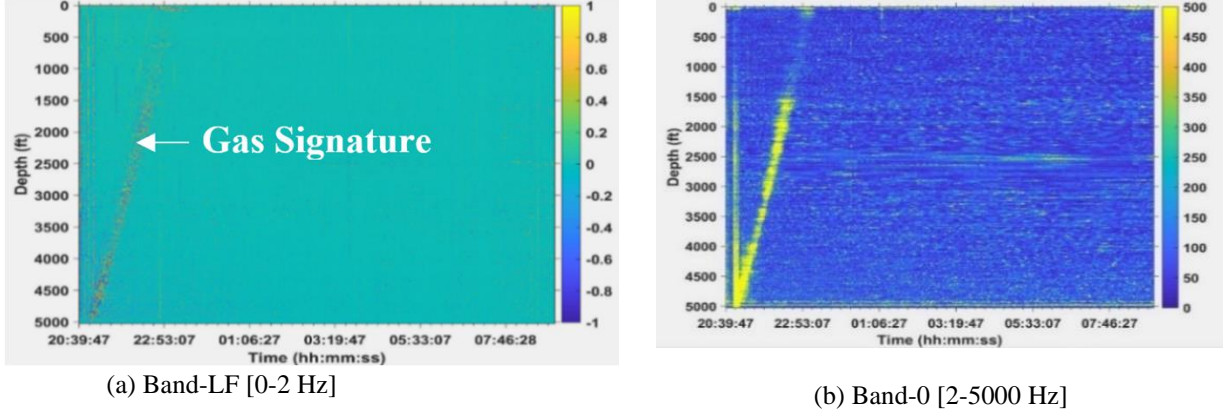


Figure 7. Waterfall plots showing the DAS values in the different frequency bands for Dataset-1.

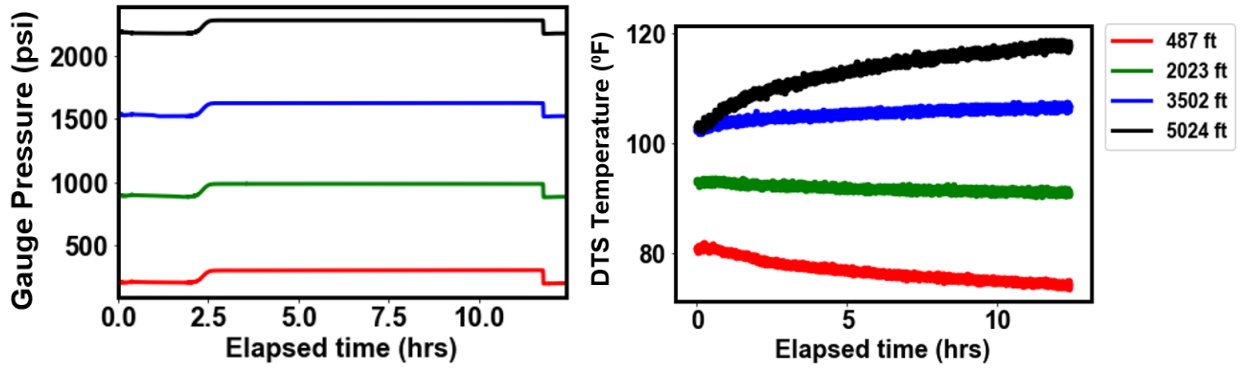


Figure 8. Pressures from downhole gauges and DTS at the four gauge locations for Dataset-1.

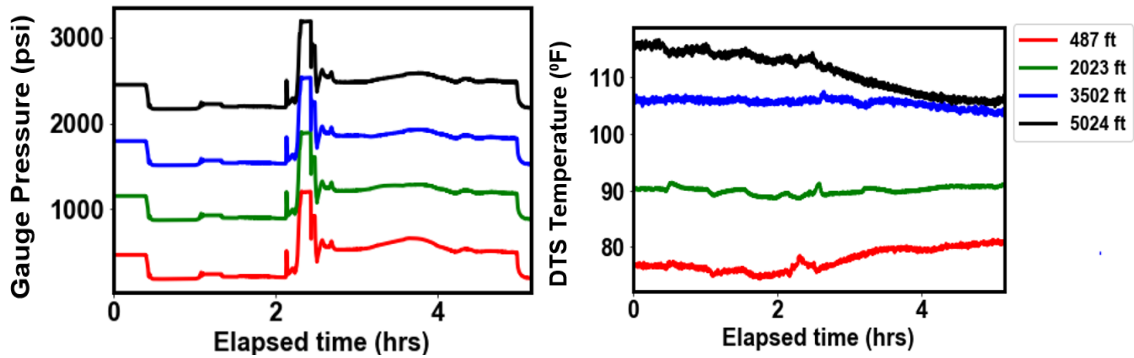


Figure 9. Pressures from downhole gauges and temperature from DTS at the four gauge locations for Dataset-2.

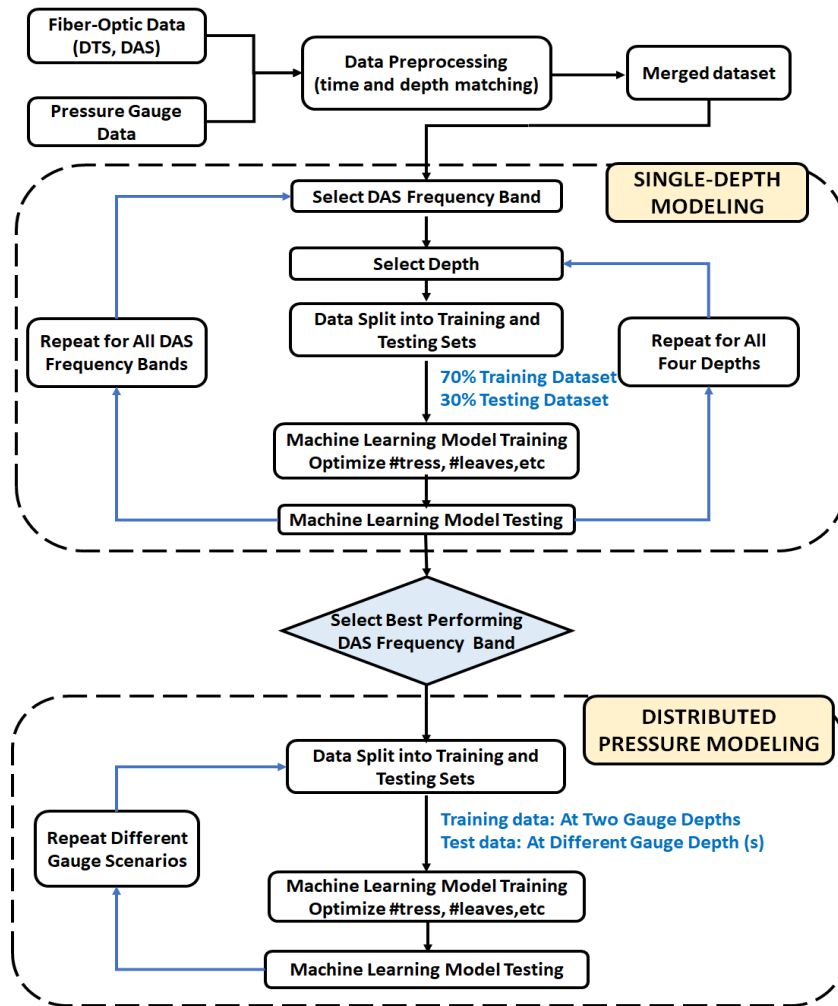


Figure 10. Combination of machine learning and signal processing workflow for pressure prediction using DTS and DAS [52].

is shown in Figure 13. It should be noted that the ANN architecture when deep enough may also give improved results but the computational time inhibits its usage.

Random Forest Algorithm

Compared to the other four machine learning algorithms investigated for our process, the random forest approach was chosen as the model of choice in the main body of this work due to its consistently strong performance (high R^2 and low RMSE) and low computing time.

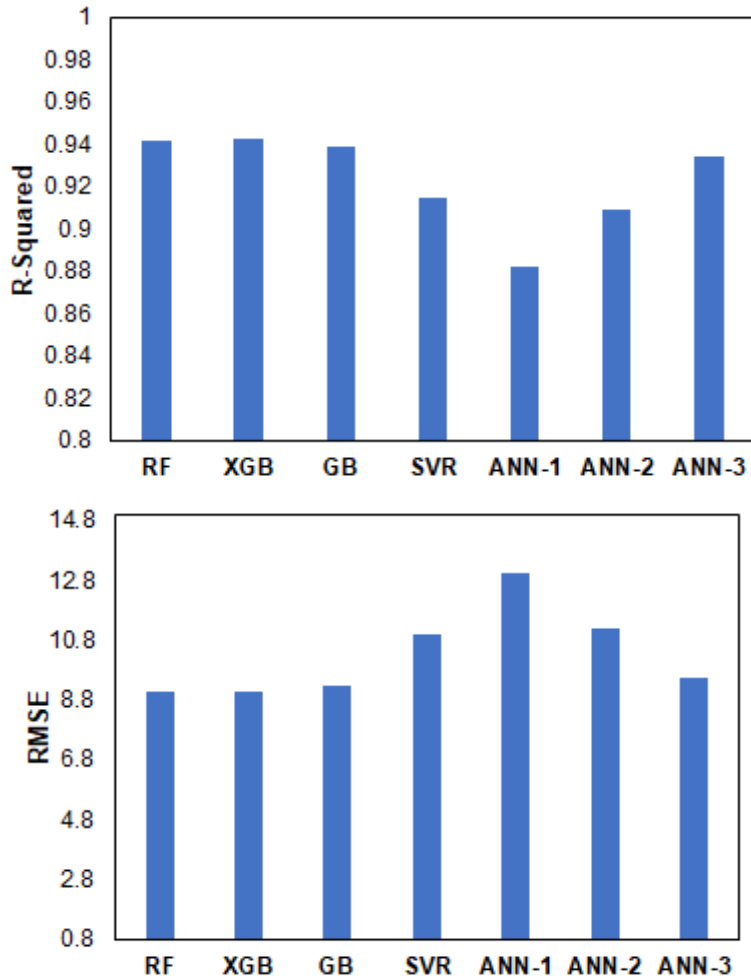


Figure 11. R2 and RMSE of the predictions obtained using the different machine learning algorithms for Dataset-2 [52].

Random forest is a multi-decision tree ensemble machine learning technique [60], [61]. The dataset must first be divided into training and testing datasets, as shown in Figure 13. Following that, the training set is randomly sampled based on the number of decision trees to be trained. The training set is then subdivided into training and validation datasets for each subgroup (otherwise known as out-of-bag samples). Each decision tree creates its own model and evaluates it using the validation samples.

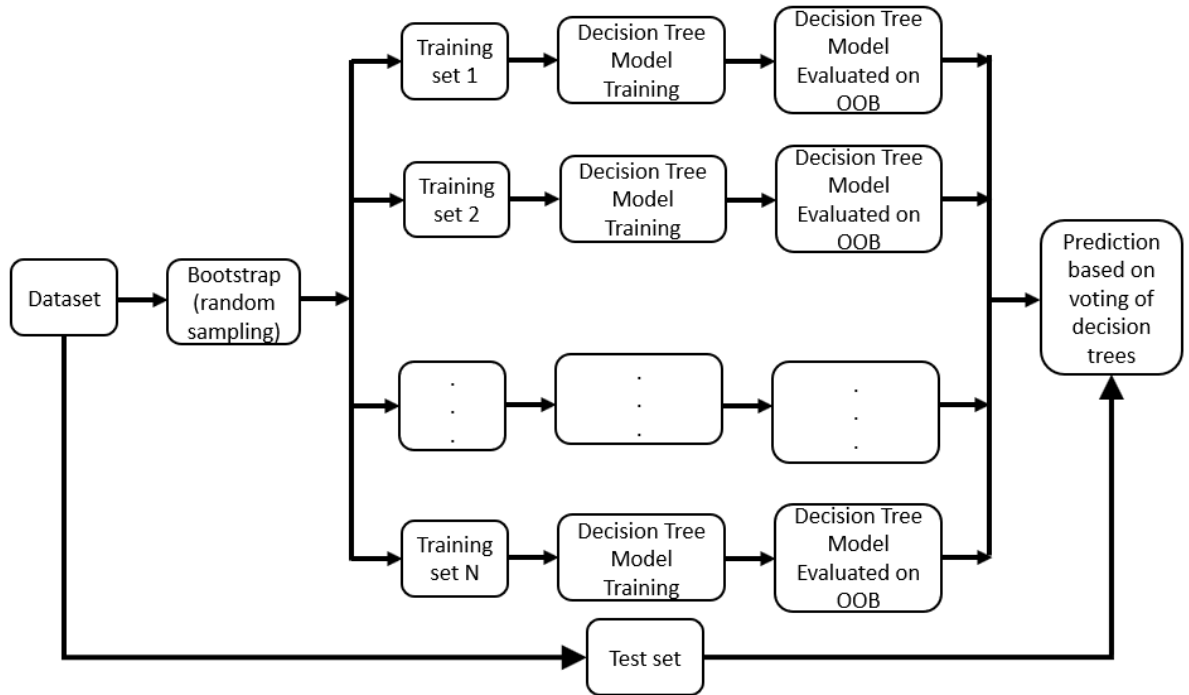


Figure 12. Schematic illustration of the random forest algorithm [50].

Machine Learning Algorithm	Model Architecture	Model Hyperparameters	Running Time (s)
Random Forest (RF)	-	Number of trees=100, learning rate=0.1, min samples split=2, splitting_criterion='mse'	0.95
Gradient Boosting (XGB)	-	Number of trees=100, learning rate=0.1, min samples split=2, splitting_criterion='mse'	0.825
Extreme Gradient Boosting (GB)	-	Number of trees=100, learning rate=0.1, min samples split=2, splitting_criterion='mse'	0.9
Support Vector Regressions (SVR)	-	kernel='rbf', gamma='scale', regularization parameter (C) =1, epsilon=0.1	0.92
Artificial Neural Network (ANN-1)	2:10:1	optimizer='adam', loss='mse', batch size=10, epochs=1000, activation function=ReLU	244
Artificial Neural Network (ANN-2)	2:10:10:1	optimizer='adam', loss='mse', batch size=10, epochs=1000, activation function=ReLU	248
Artificial Neural Network (ANN-3)	2:10:20:10:1	optimizer='adam', loss='mse', batch size=10, epochs=1000, activation function=ReLU	266

Figure 13. Machine Learning models used in the preliminary model evaluation [50].

2.4. Results

The input and output features for the machine learning models for the single-depth and distributed pressure modeling phases are summarized in Table 2.

Table 2. Machine learning model features for the single-depth and distributed pressure modeling.

Random Forest Model	Predictor (Input Variables)	Target (Output Variable)	Number of Datapoints (Training / Testing Data)
Single-Depth Analysis	DAS (all frequency bands), DTS	ΔP	2668 / 1144 (Dataset-1) 553 / 238 (Dataset-2)
Distributed Depth Analysis	DAS (Band-LF), DTS, Time	ΔP	7624 / 7624 (Dataset-1) 1582 / 1582 (Dataset-2)

2.4.1. Single-Depth Predictive Modeling

The R^2 of the Band-LF ranged from 0.90 to 0.99, with an average performance of 0.97 across all depths, whereas the R^2 of the higher frequency bands ranged from 0.81 to 0.83 across all depths. Similarly, the RMSE values for the Band-LF ranged from 0.8 to 11.4 psi, whereas the RMSE values for the higher frequency bands ranged from 8 to 23 psi. The results show that for Dataset-1, the low-frequency DAS data provides a more accurate pressure forecast. The R^2 values for the Band-LF in Dataset-2 ranged from 0.90 to 0.96, with an average of 0.94 at all depths. For the higher frequency DAS bands, the average R^2 values varied from 0.64 to 0.75. Similarly, the RMSE values for the Band-LF ranged from 6.7 to 11.3 psi, whereas the higher frequency bands had RMSE values ranging from 12.3 to 39.5 psi. Figure 14 shows the R^2 and RMSE for the test set for a single gauge depth while Figure 15 shows the pair plot of predicted and actual values.

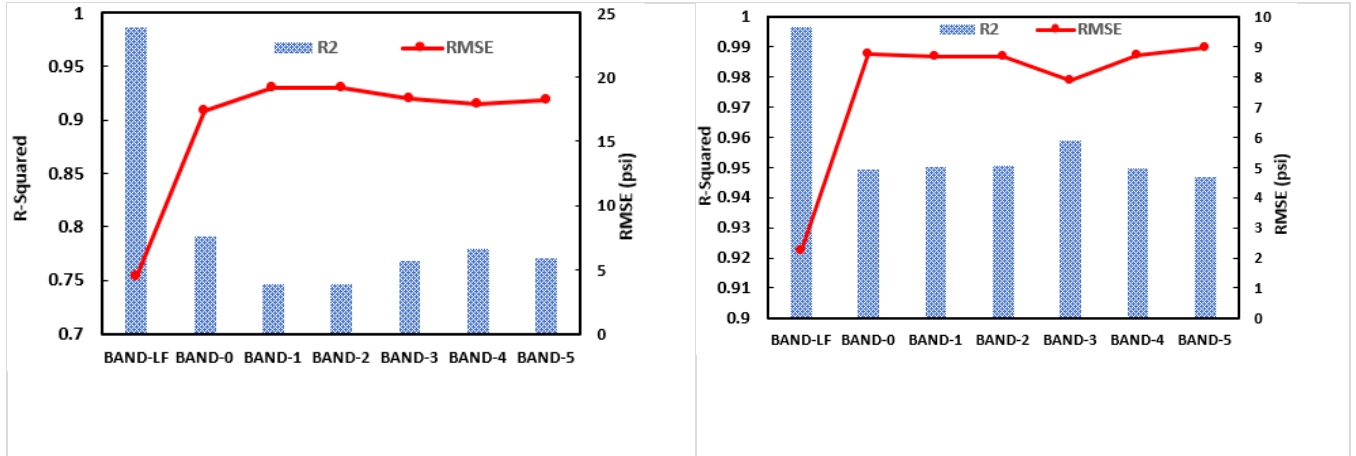


Figure 14. The RMSE and R^2 values for the testing subsample at each gauge depth for Dataset-1 [52].

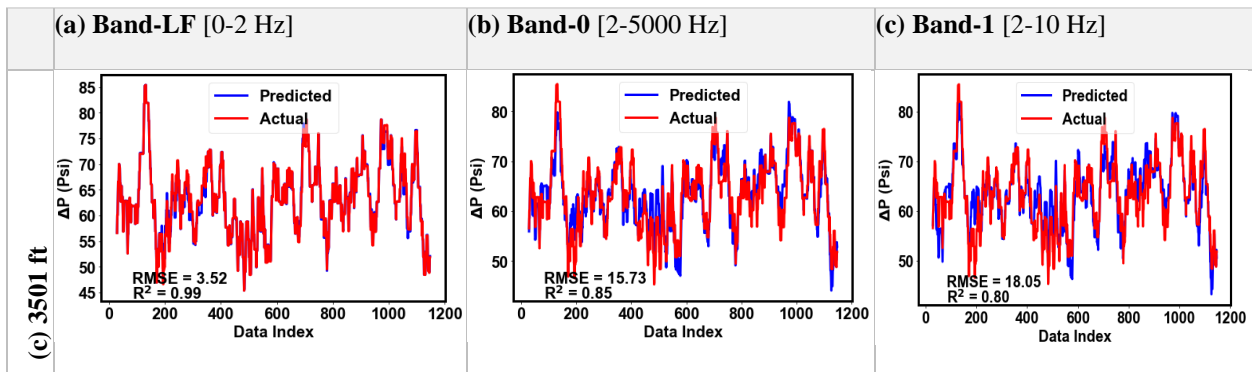


Figure 15. Pressure prediction using DAS Bands LF, 0, and 1 for the testing set for Dataset-1 (RMSE in psi) [52].

2.4.2. Distributed Pressure Predictive Modeling

The single-depth pressure modeling findings clearly showed that the low-frequency DAS (or Band-LF) performed consistently better than the higher-frequency DAS bands. As a result, we employed the DAS Band-LF, DTS, and elapsed time as input characteristics for the distributed pressure modeling, and the change in pressure from the initial pressure as the output for the random forest model. The model was trained using datasets from any two gauge depths, and the model was then used to estimate pressures at the other two depths.

In Figure 16, for example, DTS, DAS, and pressure data were used to train the random forest model at 487 ft and 2023 ft, and the trained model was utilized to forecast pressures at 3502 ft using the DAS Band-LF and DTS at that depth. For Dataset-1, the R2 values for all eight situations were greater than 0.99, with the RMSE ranging from 2.5 to 4.2 psi. In Dataset-2, strong model performance was seen in all situations, with R2 more than 0.95.

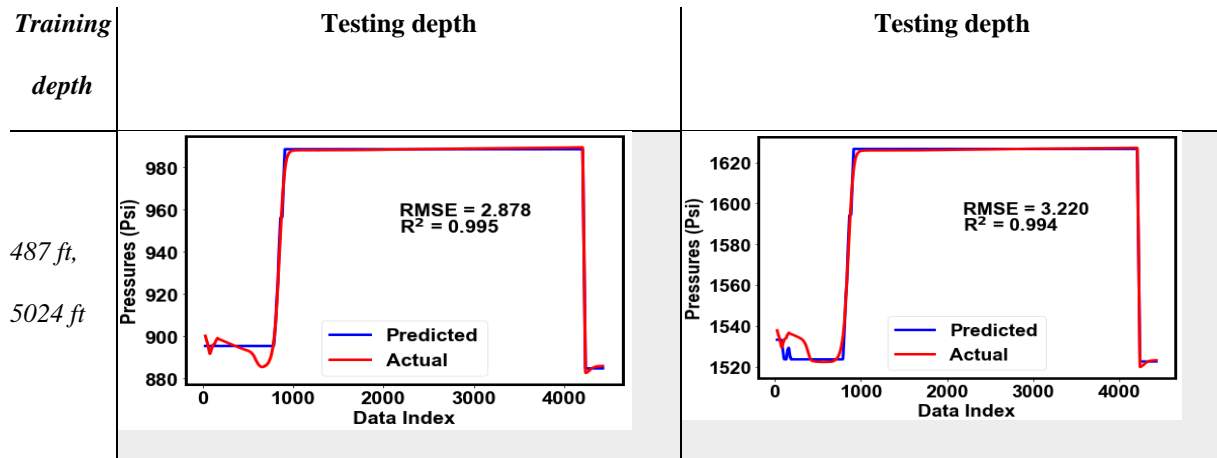


Figure 16. Comparison of the predicted and the actual pressure profiles obtained for the distributed pressure analysis for different combinations of training and testing depths for Dataset-1 (RMSE in psi).

2.5. Summary

This study presents the first well-scale application of fiber-optic DAS and DTS data for pressure prediction. We used a combination of machine-learning and signal processing to analyze the pattern in the data before using the trained model to forecast pressure data at different depths. In an oilfield, surface and downhole pressure gauges are commonly available and can be utilized for model training.

The findings are in line with those of several recent research, which have found that low-frequency DAS has a superior correlation with pressure. In their laboratory-scale experiment, Becker et al. [33] found that the low-frequency DAS band (100mHz) was more sensitive to fluid pressure. The pressures evaluated in our well-scale tests reached up to 3200 psi, whereas the

greatest pressure in the Becker study was less than one psi. This research shows how low-frequency DAS paired with DTS may be utilized to monitor distributed pressure on a well-scale.

Chapter 3. Automated Detection and Quantification of Gas Influx Velocity

3.1. Introduction

Undetected gas kicks during drilling or completion are to be blamed for many disastrous incidents in the oil and gas industry. As a result, early detection of gas influx (or kick) into the wellbore is critical to avoid the loss of lives and valuable assets, such as the rig, as well as environmental damage. Traditional gas-kick monitoring techniques such as pit gains, increases in flow rate from a well at constant pump speed, and pumps-off flow from the well are surface indicators that suffer from time delay in detecting conditions between the surface and the downhole. These surface-based approaches may also have inadequate accuracy when dealing with small overflows.

In this chapter[†], a unique workflow is proposed that identifies gas-kick and estimates gas influx velocity using real-time downhole data from DAS deployed in a wellbore. The Hough transform, which is a feature extraction approach for grouping edge points into object candidates via a vote operation across a set of parameterized picture objects, is employed in the workflow [62]. The Hough transform is applied to frequency-wavenumber (f-k) graphs to estimate the gas influx velocity in real-time, as discussed in the next section.

3.2. Methodology

Figure 17 depicts the workflow, which includes the processes of data collection, processing, and interpretation. First, a 2-dimensional time-depth matrix is created from the raw time-series DAS vibration data (recorded in SEG-Y format). The data from each duration of the recording is then

[†] This chapter was previously published as G. K. Ekechukwu and J. Sharma, "Automated Detection and Quantification of Gas Influx Velocity in Wellbore from Fiber-Optic Sensor Data," in *OSA Optical Sensors and Sensing Congress 2021*, paper JTh6A.11. DOI:[10.1364/AIS.2021.JTh6A.11](https://doi.org/10.1364/AIS.2021.JTh6A.11)

concatenated to form a larger matrix that corresponds to the times of interest. A single SEG-Y file for a recording length of 10s is about ~920 MB in size, equating to ~330 GB per hour or ~8 TB per day. As a result, the data size is quite huge, necessitating data compression. The Fourier transform is used as the typical data compression approach for each depth (trace or row data) for each recording length. For all bands, the FBE file generated per record length (10 s) reduces the size from 920 MB to roughly 90 KB. The FBE data created in the preceding phase is transformed into frequency-wavenumber (or f-k) space in the next stage of the pre-processing steps [12]. The maximum wavenumber and frequency values in the new domain are given by the Nyquist equation as:

$$k_{max} = \frac{1}{2\Delta x} \quad 3.1a$$

$$f_{max} = \frac{1}{2\Delta t} \quad 3.1b$$

Currently, the gas rise velocities are visually identified and manually calculated. Sharma, et al. [12] have shown this approach of visual detection and manual calculation utilizing low-frequency DAS (the red rectangle in Figure 17a). Manual estimations of gas velocities, on the other hand, can be subjective, time-consuming, and difficult to execute in continuous monitoring for several wells, making it impossible to make time-sensitive decisions, such as monitoring gas kick. This research offers a possible solution. The Hough transform was applied on the f-k plots of the low-frequency DAS FBE data to find straight lines, as shown in Figure 17b, and the gas velocity was determined using the slope of the straight line. A line can be represented in the conventional Hough transform as the point of intersection of the slope (m) and intercept (c), as indicated in equation 3.2.

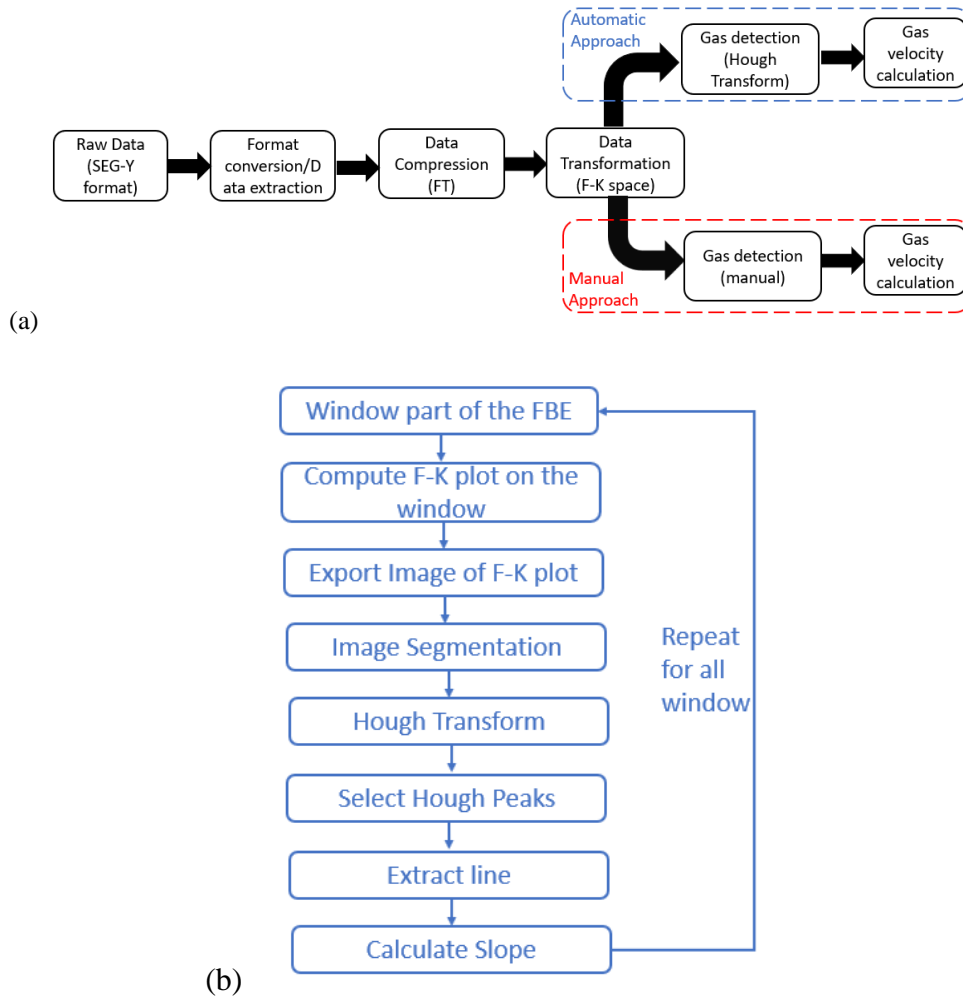


Figure 17. (a) Overview of the workflow (b) Details of the automated portion for estimation of gas rise velocity [63].

As shown in Figure 17, the Hough transform is applied on the f-k plots of the low-frequency DAS FBE data to detect straight lines, and then the gas velocity was estimated by the slope of the straight line. In classical Hough transform, a line can be represented as the point of intersection of the slope (m) and intercept (c) as shown in equation 3.2. However, this m - c form will not be able to represent vertical lines and therefore the polar coordinate formulation was used as shown in equation 3.3.

$$y = m * x + c \tag{3.2}$$

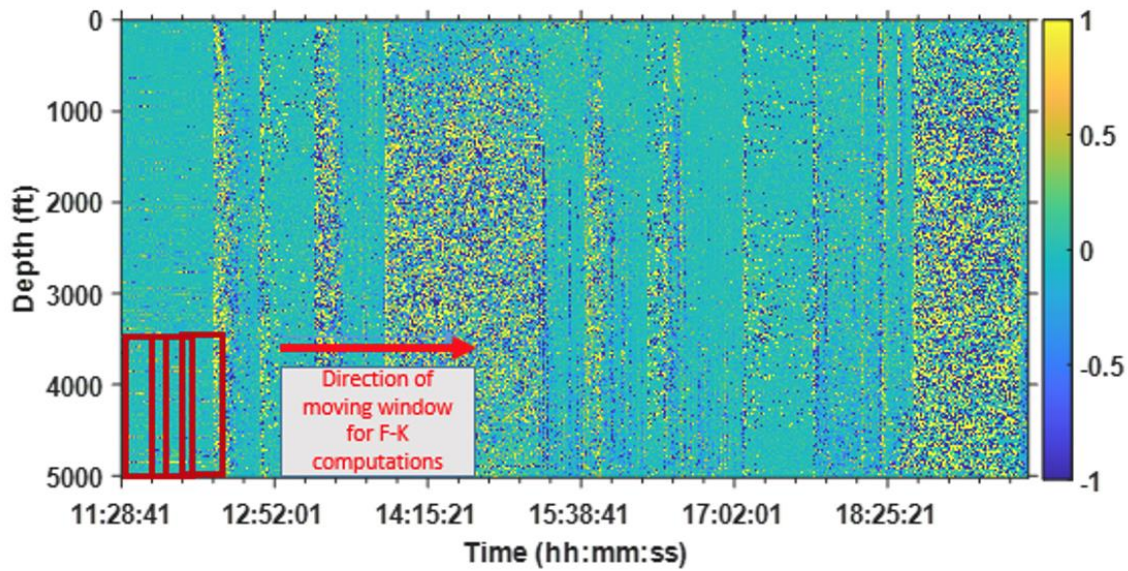
$$r = x \cos \theta + y \sin \theta \quad 3.3a$$

$$y = -\frac{\cos \theta}{\sin \theta} x + \frac{r}{\sin \theta} \quad 3.3b$$

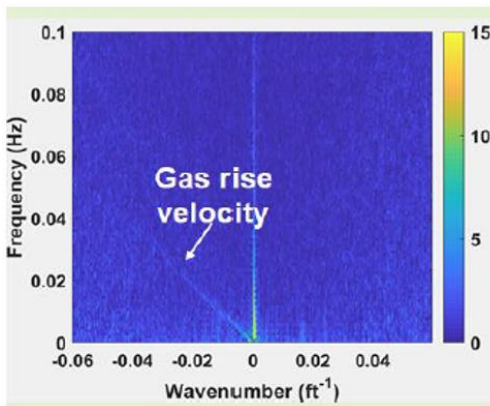
The mapping of a fixed point (x,y) to a sinusoidal line in the Hough space is a particularly important variant. As a result, points on the same line in cartesian space will correspond to the Hough parameter space intersection point of their respective sinusoids. The Hough accumulator is used to find places where the Hough space sinusoids intersect most frequently. When a point on a cartesian plot is modified, the accumulator's bins for all lines that pass through that point are increased. Lines are then discovered by applying a threshold to the accumulator matrix's maximum value.

3.3. Results

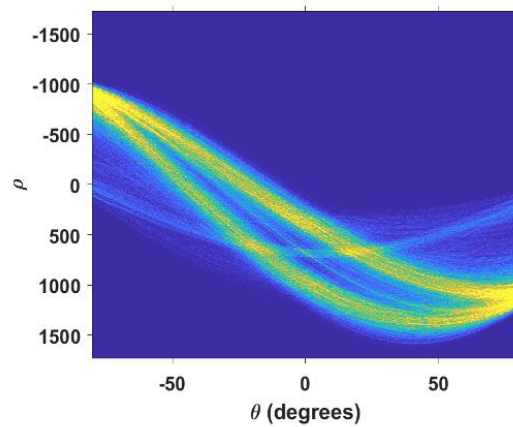
The suggested approach was tested on DAS data from well-scale gas-kick experiments carried out in a 5163-foot deep test wellbore described in section (1.3. Test Well) [64], [65]. When compared to high-frequency DAS, Sharma et al. [2] found that low-frequency DAS (> 2 Hz) resulted in better detection of the gas rise (2-5000 Hz). As a result, the low-frequency DAS was used to create the proposed automated workflow. Figure 18a depicts the gradient of the low-frequency DAS FBE with respect to time across an eight-hour time segment. The f-k and Hough transforms were applied across 53 windows covering the bottom parts of the FBE.



(a)



(b)



(c)

Figure 18. (a) Visualization of the sliding window on the FBE data (b) F-K transform space (c) Hough space representation.

Each window is propagated from the left to the right of the FBE plot and covers a predetermined length of time series interval. The f-k plot of one of the windows where gas was identified is shown in Figure 18b, while the Hough space representation is shown in Figure 18c. Only a few areas of the original FBE would show the presence of gas based on real experiments [12], [64]. Such windows will be detected by the automated workflow, which will then estimate

their rise velocities. Using the confusion matrix (or error) concept, the number of true positives (TP), false negatives (FN), false positives (FP), and true negatives (TN) is 7, 1, 0, 45, giving an accuracy of roughly 98 % in predicting gas presence. However, due to the data imbalance in the number of samples with and without gas in the dataset, the accuracy metric may not fully capture the performance of the methodology. The recall (another machine learning-based metric) can be used instead. The recall is the fraction or percentage of actual positive results that were detected as indeed positive. Hence, the recall for the positive case (i.e., when gas is present) in this example will be 7/8 or 87.5%. The ground truth was obtained by identifying windows containing gas from other methods such as pressure drop and DTS. Furthermore, a comparison of the velocity computed using the workflow and manual calculations reveal good agreement.

3.4. Summary

This study shows how to automatically identify the real-time influx of gas into a wellbore, which is an improvement over current approaches in which the gas velocity is largely identified by surface-based methods that have time-delay issues. Additional datasets can be used for further validation of the proposed workflows, which will also address the data imbalance issue

Chapter 4. Interface Tracking and Estimation of Gas Fraction Using Distributed Fiber-Optic Sensor and Downhole Pressure Data

4.1. Introduction

Multiphase flow is encountered in various industrial and engineering applications, such as in the chemical, geothermal, nuclear, petroleum, and space industries. The use of DFOS for fluid composition analysis and interface tracking has been gaining more attention recently. This chapter presents the estimation of gas fraction along the wellbore's depths using different techniques. The findings of our research will be beneficial to improve and validate fiber-optics-based production logging algorithms, detection, and quantification of gas leak volumes in the wellbore, and pipeline flow monitoring. Gas fraction or void fraction is the volume of space occupied by the gas in multiphase flow scenarios. It is one of the most fundamental parameters required in different flow calculations, such as two-phase viscosity, density, and pressure drop calculations. Many experimental studies and several correlations have been proposed to estimate this essential parameter in two-phase flow.

This chapter presents workflows to calculate the gas fraction along the wellbore in real-time. The gas fraction at different sections of the wellbore will be estimated using two independent methods. The first method that will be explored is the use of combined pressure-difference and DFOS data to estimate gas fraction. The second method will investigate the application of the speed of sound (SOS) in mixture for determining the gas fraction in the wellbore. The parameters needed as input for both gas void fraction methods described above were obtained using a novel analysis workflow comprising of several signal processing and filtering steps. Some previous authors have experienced some challenges in using SOS for phase fraction estimations. Paleja et al. [19], in their experimental study, found the SOS in an air-water mixture to be 10-20 m/s, which

was less than that of water (1450 m/s) or air (300 m/s), hence was not able to estimate the gas fraction. Other previous studies, e.g., Bukhamsin et al. [66] that have also explored the SOS method, had inflow control devices (ICDs) in their wellbore that created restrictions in the wellbore. Flow-through ICDs created enhanced perturbations that would be easier to detect using DAS. In our test well setup, there are no restrictions in the wellbore, hence we have a more challenging experimental setup since the self-generating pressure waves may not be strong enough [67]. The two proposed workflows address this challenge in our experimental setup. More details about the two methods are described below.

4.2. Methodology

4.2.1. Gas Void fraction Estimation

Method 1: Pressure Difference Method (PDM)

The gas fraction can be estimated from the modified hydrostatic pressure equation shown below:

$$\Delta P_{ij} = 0.052 * \alpha (\rho_w - \rho_g) * h_s \quad 4.1$$

$$\alpha = \frac{\Delta P_{ij}}{0.052 * (\rho_w - \rho_g) * h_s} \quad 4.2$$

Where ΔP_{ij} is the pressure difference of the two pressure gauge readings in between which the gas-liquid mixture region has been identified. Here, h_s is the gas-water mixture height, ρ_w and ρ_g are water and gas densities, respectively, and α is the gas void fraction that is to be calculated, and 0.052 is the unit conversion factor from the SI unit when the units of the pressure, density, and height are psi, ppg, and ft, respectively. Figure 19 shows the schematic of a gas slug (gas-liquid mixture) rising in the annulus of a well. As time progresses from t_1 to t_3 , the gas moves from the bottom of the well to the top of the well.

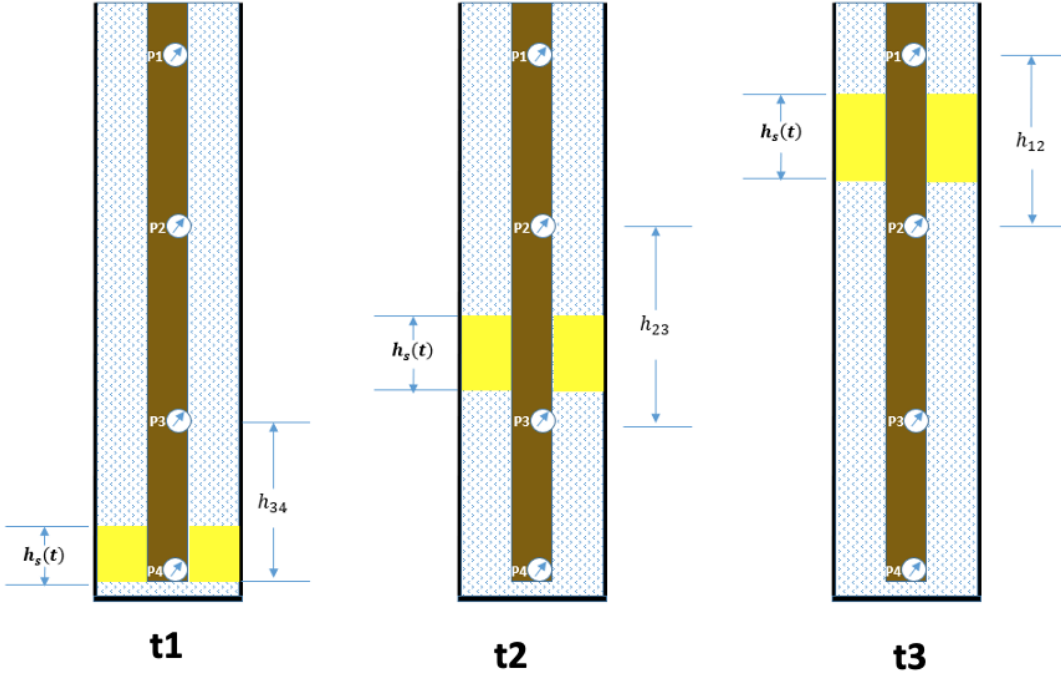


Figure 19. Schematics showing the gas rise in the annulus of the well.

The gas-water mixture length at different times and depths along the wellbore can be estimated using the velocity band energy methodology described later in the chapter.

Method 2: Speed of Sound (SOS) Approach

The method described in this section follows the procedures that were described by Chaudhuri et al. [18] and Bukhamsin et al. [65]. The SOS in a fluid is given by the Newton-Laplace equation:

$$c_m = \sqrt{\frac{K_m}{\rho_m}} \quad 4.3$$

Assuming that the average density of a fluid mixture can be estimated using arithmetic mean as:

$$\rho_m = \alpha_g \rho_g + (1 - \alpha_g) \rho_w \quad 4.5$$

and the fluid mixture bulk modulus can be approximated by the harmonic mean of the two fluids as follows:

$$K_m = \left[\frac{\alpha_g}{K_g} + \frac{(1 - \alpha_g)}{K_w} \right]^{-1} \quad 4.6$$

If the geometry of the pipe (diameter (d) and wall thickness (t)) and elastic properties such as Young's modulus (E) effects are accounted for, the equation above becomes.

$$K_m = \left[\frac{\alpha_g}{K_g} + \frac{(1 - \alpha_g)}{K_w} + \frac{d}{Et} \right]^{-1} \quad 4.7$$

Substituting Eqns 4.5 and 4.7 into 4.3 will give:

$$c_m = \left\{ [\alpha_g \rho_g + (1 - \alpha_g) \rho_w] \left[\frac{\alpha_g}{K_g} + \frac{(1 - \alpha_g)}{K_w} + \frac{d}{Et} \right] \right\}^{-\frac{1}{2}} \quad 4.8$$

The gas and water moduli can be substituted as $K_g = c_g^2 \rho_g$ and $K_w = c_w^2 \rho_w$, α_g respectively. The gas void fraction α_g can then be calculated by solving the quadratic equation:

$$\alpha_g = \frac{-B \pm \sqrt{B^2 - 4AC}}{2A} \quad 4.9a$$

Where the coefficients are defined as:

$$A = \left(\frac{1}{c_g^2} - \frac{\rho_g}{\rho_w c_w^2} \right) \left(1 - \frac{\rho_w}{\rho_g} \right) \quad 4.9b$$

$$B = \frac{\rho_g}{\rho_w c_w^2} + \frac{\rho_w}{\rho_g c_g^2} - \frac{2}{c_w^2} + \frac{\rho_g d}{tE} - \frac{d}{tE} \quad 4.9c$$

$$C = \frac{1}{c_w^2} - \frac{1}{c_m^2} + \frac{\rho_w d}{tE} \quad 4.9d$$

The SOS in a fluid mixture as a function of the composition of the fluid mixture is shown in Eqns 4.8 and 4.9 above. The SOS curve is also dependent on the pressures and temperatures encountered at each depth because they affect the fluid properties. This is demonstrated In Figure 20 a-d, which

were obtained at gauge depths of 487 ft (with P = 211 Psi and T = 90 °F), 2023 ft (with P = 890 Psi and T = 95 °F), 3502 ft (with P = 1528 Psi and T = 104 °F), and 5025 ft (with P = 2180 Psi and T = 105 °F), respectively.

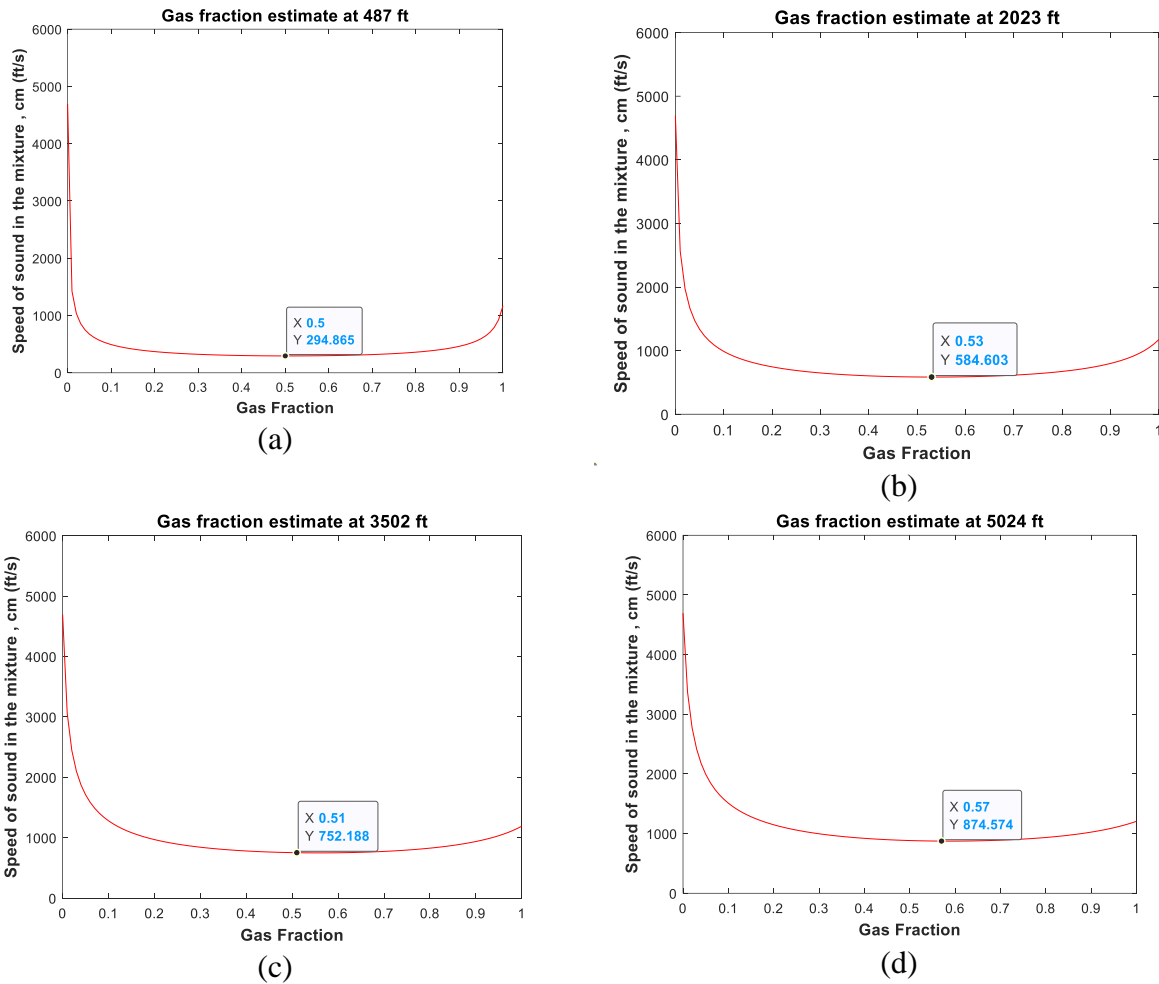


Figure 20. The SOS in a fluid mixture as a function of the fluid composition.

The corresponding pressure and temperature values were obtained from the downhole gauges corresponding to hydrostatic conditions in the PERTT test well. The plot shows that the minimum values of the SOS curve are highly dependent on the pressures and temperatures and hence on the depth of the gas slug (gas-liquid mixture region) as well.

The first step is to estimate the SOS of the mixture (c_m) at the depth of interest. The c_m value is then traced horizontally to intersect the SOS curve. Finally, the corresponding gas fraction at the

point of intersection is determined. For instance, if the c_m is 1500 ft/s, as shown in Figure 21, the gas void fraction will be estimated to be 0.9. For SOS values that give two possible gas fraction solutions from this approach, additional information is utilized to select the right answer, such as using mass balance consideration or another domain knowledge.

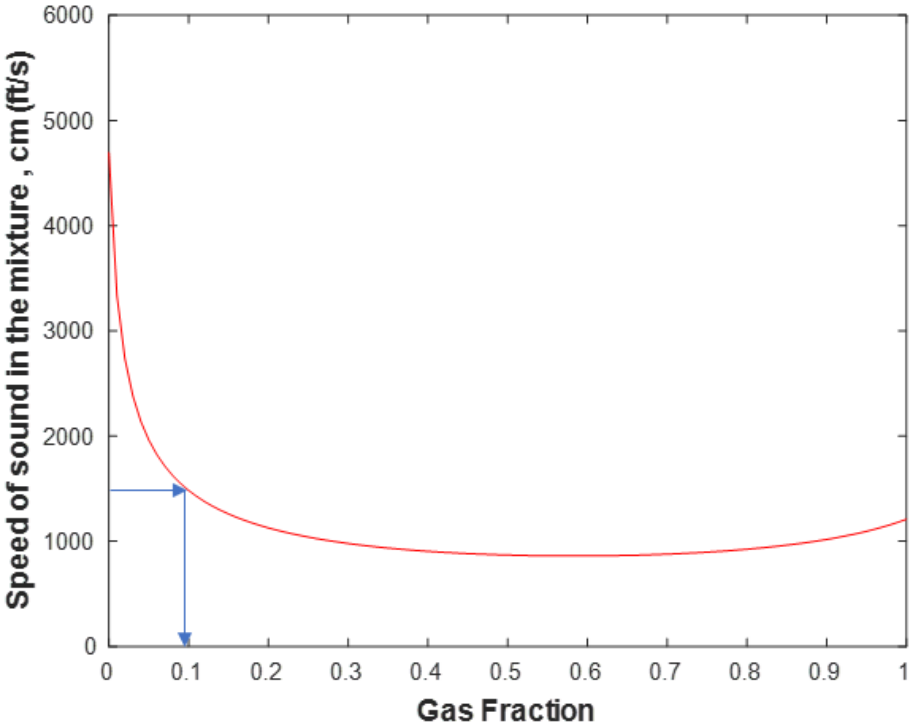


Figure 21. Illustration of gas fraction estimation estimated using SOS curve.

4.2.2. Gas-Liquid Interface Tracking

The gas-liquid interface tracking is achieved using the velocity band energy or VBE workflow described next:

Velocity Band Energy (VBE) Workflow

Figure 22 shows the workflow employed for estimating the gas-water mixture height, h_s , as well as the SOS in the mixture c_m . Both parameters are obtained from the DAS data, and act as inputs to the gas fraction estimation methods discussed above. The gas-water mixture height h_s is used

in the pressure-difference estimation method while c_m is used in the SOS estimation technique. The VBE workflow, as shown in Figure 22, is divided into two phases; phase one of the workflow starts with getting a representative 2D DAS vibration input sample. The mirror boundary condition is then applied to remove boundary artifacts. Next, a gradient with respect to time is performed to remove the horizontal streaks in the data which are a result of the non-uniform coupling of the fiber to the tubing. The last step in phase 1 of the workflow is to apply frequency and wavenumber filtering. For the frequency filtering, a high-pass Butterworth filter is applied in the time direction. The high-pass filter is used to remove the horizontal lines (the DC components of the signal) as well as the pump noise in the circulation case, whereas, for the wavenumber filtering, the Butterworth filter is applied in the depth direction. This is to ensure that long wavelengths are removed from the data to optimize the visualization of the gas-water mixture. The Butterworth filter is a time-domain filter in which the frequency response is as flat as possible in the bandpass. The result at the end of phase 1 is used for estimating the SOS in the gas-water mixture by tracing the slope of the up-going and down-going waves observed in the filtered plot. The phase two of the workflow starts with the application of the automatic gain control (AGC). The AGC is a popular seismic processing technique [66] that is applied to enhance the weak signals in the data (make it uniform across the fiber). This was achieved by multiplying the DAS values with a scaling factor $g(x)$. The scaling function for each depth is the inverse of the root mean square of all the DAS values at that depth for each time window considered which can be represented as:

$$g(x) = \frac{1}{\sqrt{\frac{1}{N} \sum_1^N A_i}} \quad 4.10$$

Where A_i are the DAS values, and N is the total number of samples in each depth.

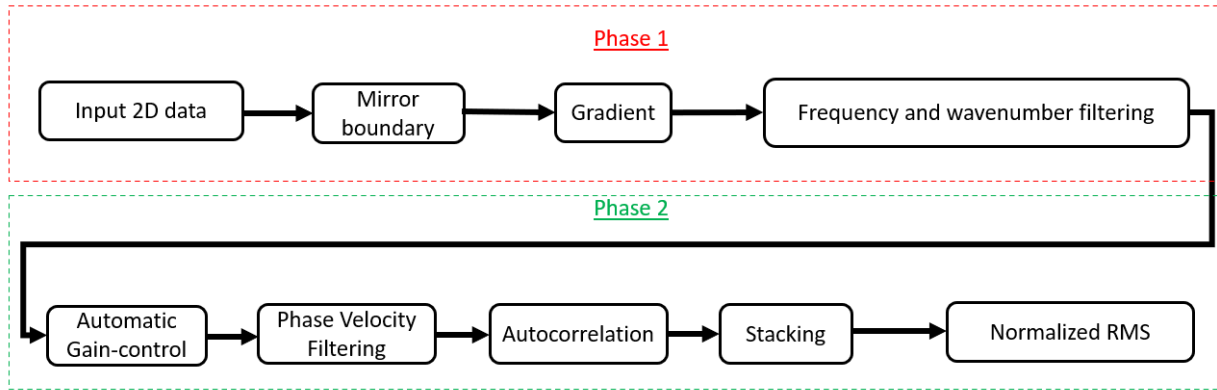


Figure 22. The velocity band energy workflow.

The phase velocity filtering part of the workflow can be summarized as shown in Figure 23. The input into the VBE workflow is the AGC-processed data. 2D FFT is applied to the AGC data, and a velocity map is created. The velocity at each cell in the velocity matrix is the ratio of its corresponding frequency to the wavenumber. A velocity range of interest is then specified to create a velocity mask. To obtain the gas-VBE-RMS plot, the velocity range of 900-1200 ft/s is specified, while for the water-VBE-RMS plot, the range of 4900-5200 ft/s is specified, based on the SOS observed in Figure 20. The velocity map is then multiplied with the created velocity mask to obtain the velocity-filtered data. Lastly, the inverse Fourier transform is applied to present the time-space version of the data.

The phase velocity-filtered data is then passed through an autocorrelation function. The autocorrelation function is a special type of cross-correlation function. The cross-correlation function is used to compute the degree of similarity or dissimilarity between two analytical signals $x(t)$ and $y(t)$, which can be mathematically expressed as shown in Eqn. 4.11 below [68]:

$$R_{xy}(\tau) = \int_{-\infty}^{\infty} x(t) y(t + \tau) dt = \int_{-\infty}^{\infty} x(t - \tau) y(t) dt \quad 4.11$$

Where τ is the time lag. The cross-correlation is a summation of the $y(t)$ lagged by τ multiplied by $y(t)$.

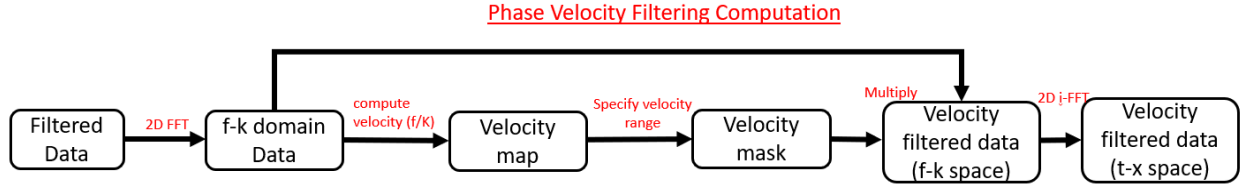


Figure 23. Phase velocity filtering computation steps.

If the result of the cross-correlation is large, then the two signals are very similar, but a smaller value shows a high degree of dissimilarity. Autocorrelation, on the other hand, is used to check the degree of similarity of the $x(t)$ is given by:

$$R_{xx}(\tau) = \int_{-\infty}^{\infty} x(t) x(t + \tau) dt = \int_{-\infty}^{\infty} x(t - \tau) x(t) dt \quad 4.12$$

Calculating the autocorrelation of the signal $x(t)$ is the same as the square of the amplitude spectrum in the frequency domain. In other words, taking the power spectrum of $x(t)$ in the frequency domain is another way to compute the autocorrelation function.

$$\mathfrak{F}\{R_{xx}(\tau)\} = R_{xx}(\omega) = X(\omega).X(\omega) = |X(\omega)|^2 \quad 4.13$$

Where ω is the angular frequency. In this work, the autocorrelation was computed at each depth in the frequency domain, and then the inverse Fourier transform was applied to convert the result back to the time-space domain, which is then stacked before the root mean square is computed. The 10-second long 2D DAS data is split into 1-second chunks and then stacked for better signal enhancement. RMS is then computed on the stacked 2D data. The computed RMS could also be normalized using the min-max approach to clearly see the intersection of the gas-VBE-RMS/water-VBE-RMS plots.

Measurement of the gas-water mixture height

The gas-water mixture height that is used in this study is estimated based on the full width at half maximum (FWHM) [69] using the gas-VBE-RMS/water-VBE-RMS plots. The FWHM is the

difference between the two values of a variable (in our case, height) at which the other variable in a plot (in our case, RMS) is equal to half of its maximum. As illustrated in Figure 24, the value of the gas-water mixture height will be $h_2 - h_1$ based on the gas-VBE-RMS plot. The average of the heights estimated from the gas-VBE-RMS and water-VBE-RMS plots will be used as the gas-water mixture height value that will be used in equation 4.2 to calculate the gas void fraction. The value of the average is very close to the heights obtained from the intersection of the normalized gas-VBE-RMS and water-VBE-RMS plots as shown in Figure 25 to Figure 27 below.

4.3. Results

4.3.1. Gas Void Fraction Estimation (No Circulation Dataset)

Both the gas void fraction estimation methodologies described above were used to estimate the gas fraction and demonstrated on two well-scale datasets. In the first trial, nitrogen gas is injected into a well that is initially occupied by water. Ten (10) bbl. of nitrogen gas was injected through the chemical line, a choke back pressure of 300 psi was applied, and then the gas was allowed to migrate in a static water-filled annulus. Figure 25, Figure 26, and Figure 27 show the results of the analysis done when the gas was located at the bottom, middle, and top of the annulus of the well, respectively. The (a) part of the figures shows the 2D matrix of the DAS SEG Y file corresponding to a 1-second data frame, and the (b) part shows the data after frequency-wavenumber (f-k) filtering has been applied. The (c) part of the figures shows the AGC-processed data, while the (d) shows the normalized gas-VBE-RMS and water-VBE-RMS cross plots. As mentioned earlier, for the gas-VBE-RMS plot, the range of 900-1200 ft/s is specified in the phase velocity filtering, while for the water-VBE-RMS plot, the range of 4900-5200 ft/s is specified, corresponding to the respective SOS values.

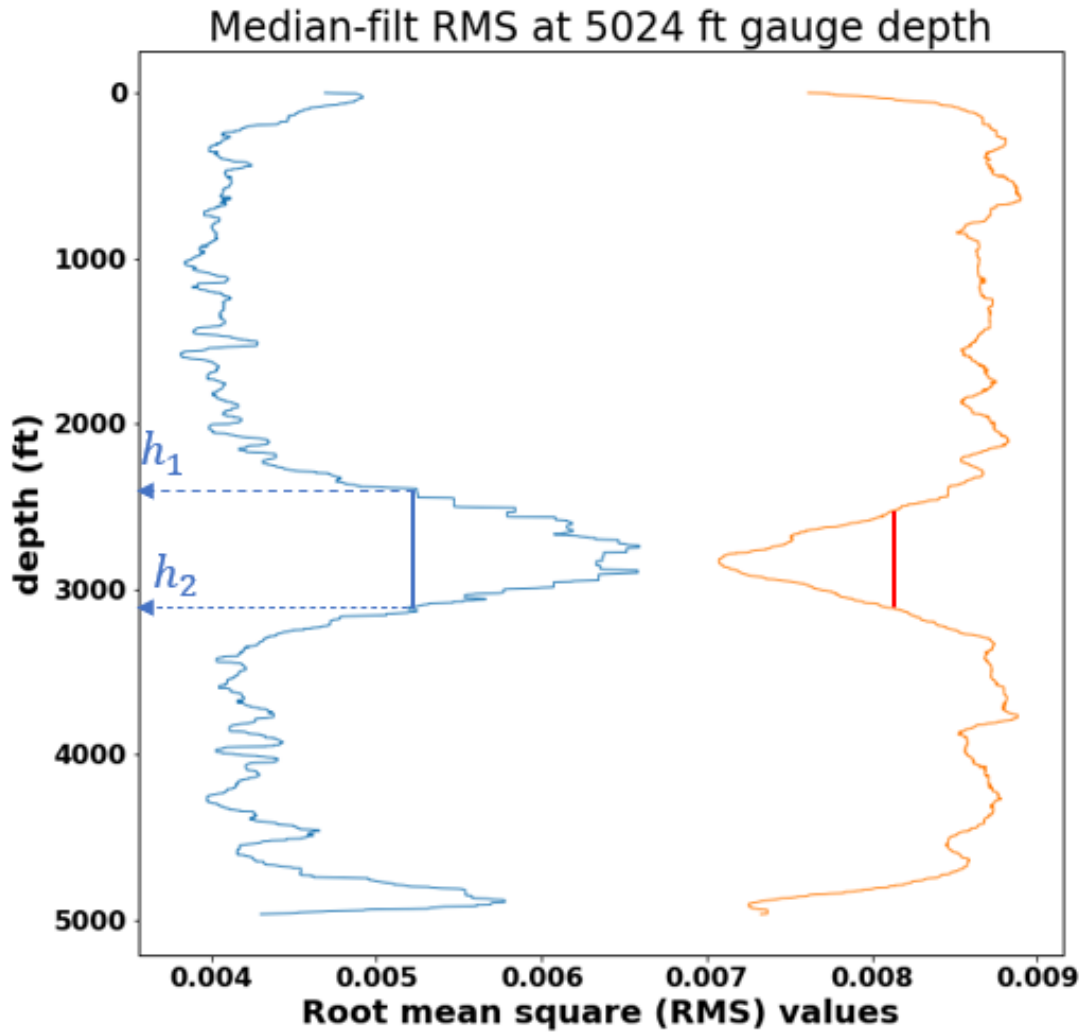
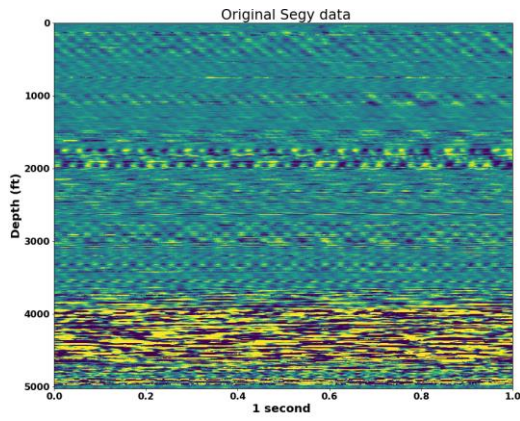
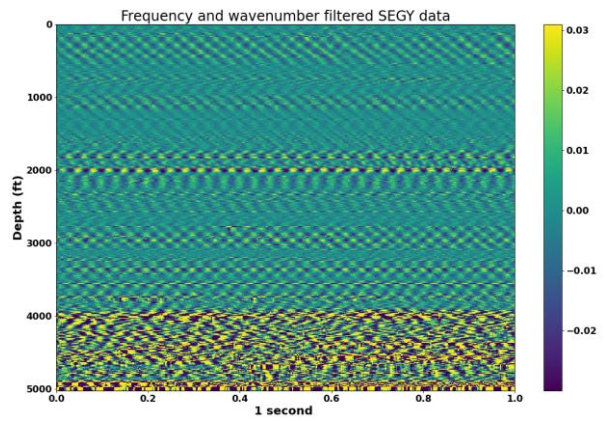


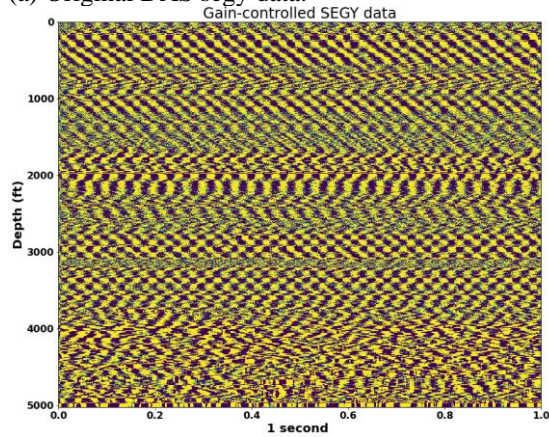
Figure 24. Gas-water mixture height calculation method using FWHM.



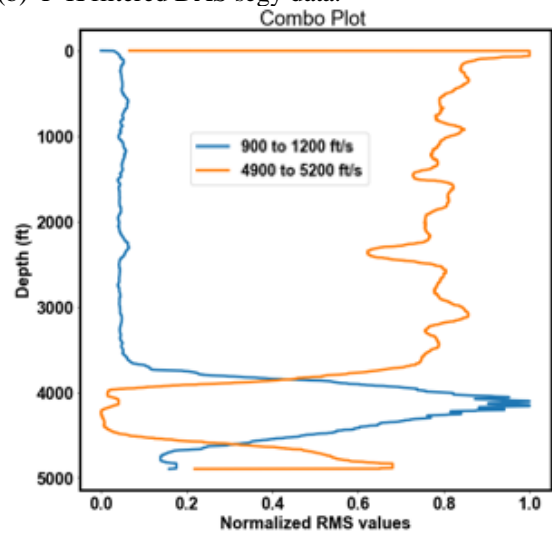
(a) Original DAS segy data.



(b) F-K filtered DAS segy data.



(c) AGC-filtered DAS segy data.



(d) Gas-vbe-rms vs water-vbe-rms crossplot.

Figure 25. Results of the analysis when gas is at the bottom of the well.

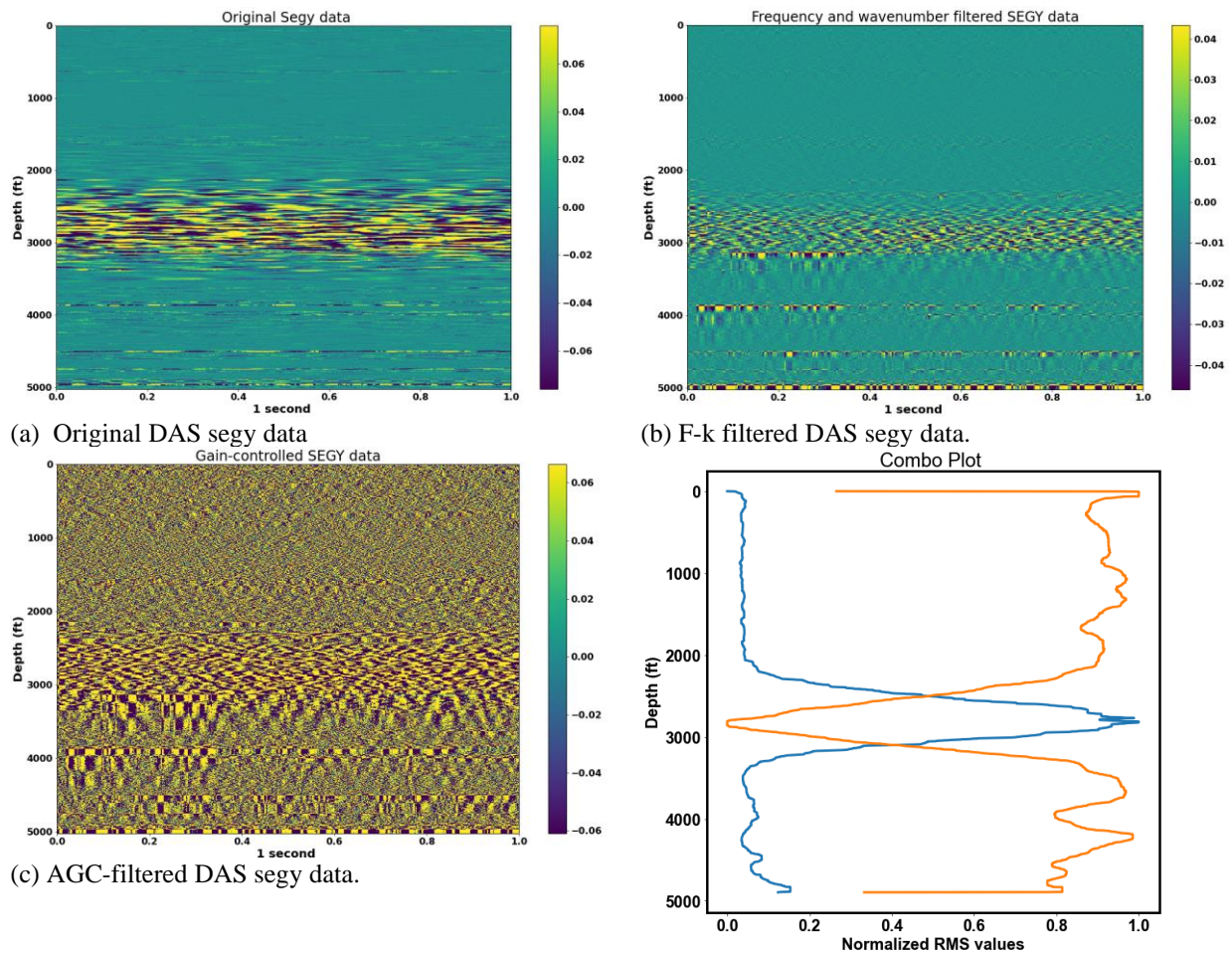
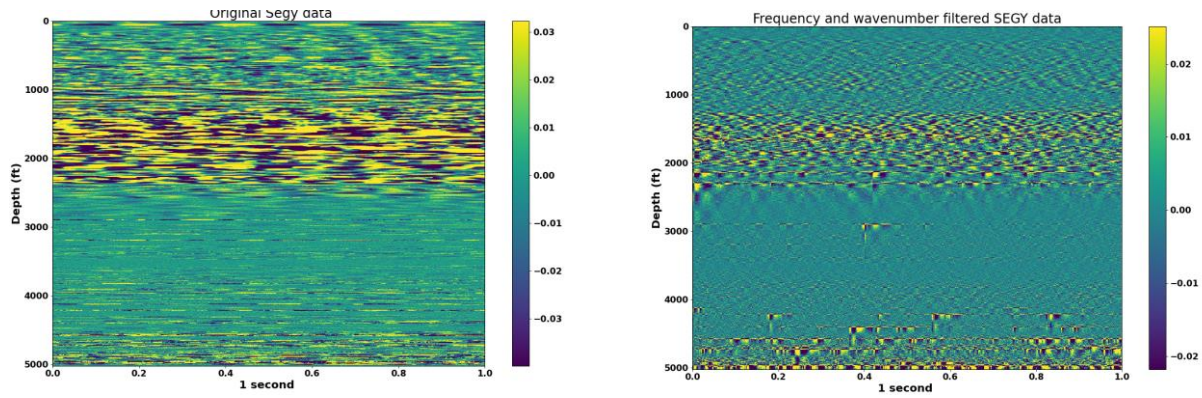


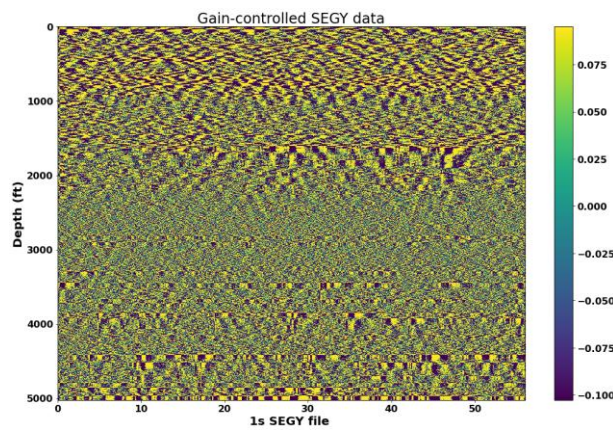
Figure 26. Results of the analysis when gas is in the middle of the well.

Figure 28 shows the pressure difference between two consecutive gauges as the gas migrates from the bottom to the top of the annulus during the first trial. The values of the pressure difference combined with the gas-water mixture heights were used to estimate the gas fraction in the three timesteps selected. To apply the SOS approach for gas fraction calculation, the SOS of the mixture was estimated by the average of the different down going, and upgoing waves identified in the f-k filtered plot, for example, those shown in Figure 29. The resulting gas fractions at different depths are displayed in Figure 30. The plots were obtained using the gauge pressures and temperatures obtained during the actual trial run.

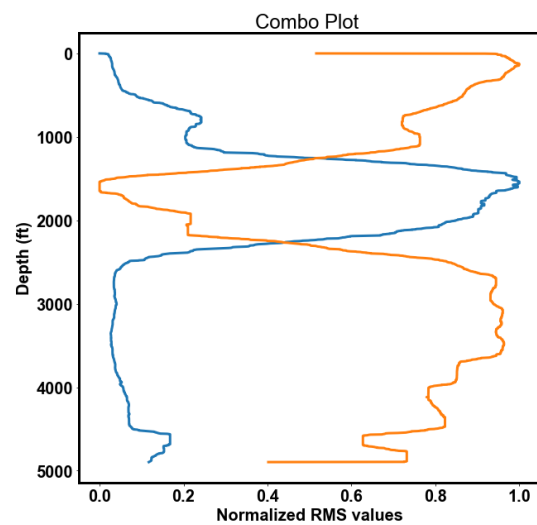


(a) Original DAS segy data.

(b) F-k filtered DAS segy data.



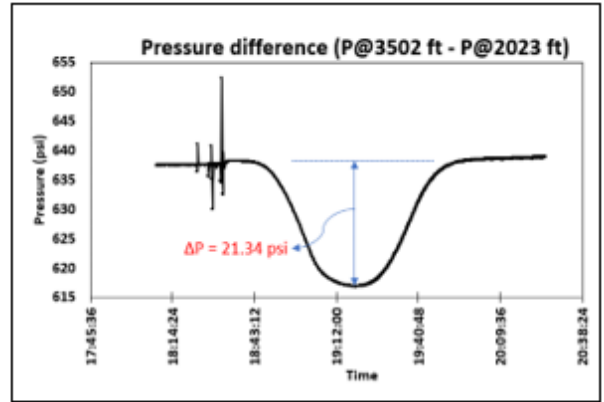
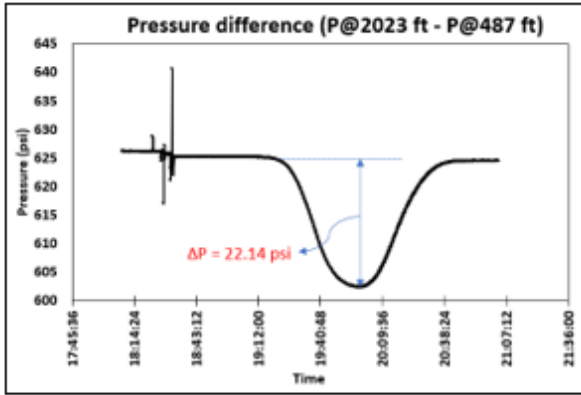
(c) AGC-filtered DAS segy data.



(d) Gas-vbe-rms vs water-vbe-rms crossplot.

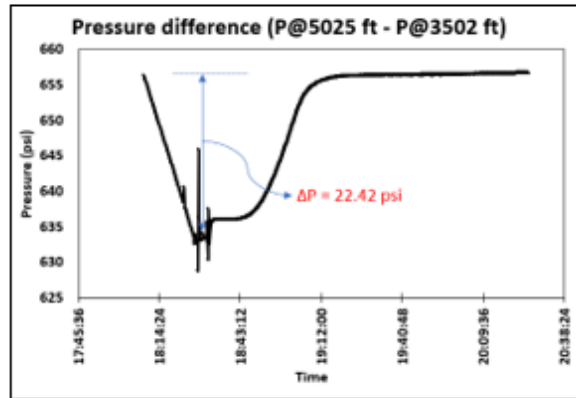
Figure 27. Results of the analysis when gas is at the top of the well.

A summary of the gas estimates from both the techniques is given in Table 3. The estimated gas void fraction using the pressure difference method ranged from 6% to 8%, with a slightly high gas fraction at the bottom than at the top. The gas fraction estimate obtained using the SOS method ranged from 5% to 7%. 4.3.2. Gas-liquid Interface Tracking (With-Circulation Case Studies). The gas-liquid interface tracking workflow is demonstrated on DAS datasets from two different scenarios as described below.



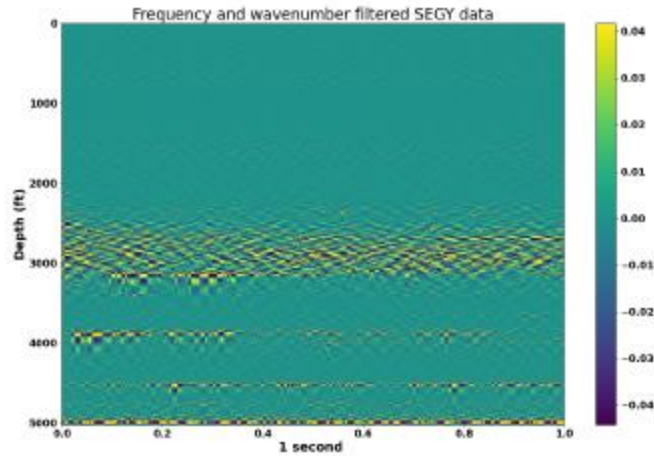
(a)

(b)

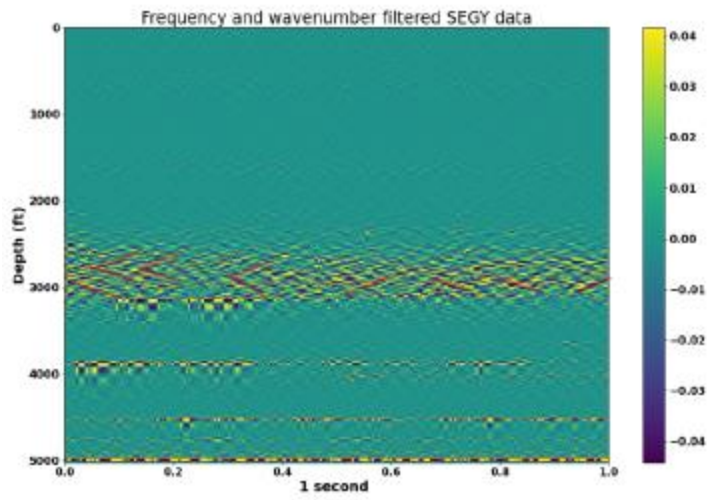


(c)

Figure 28: Pressure difference plots at different gauge depths located along the well.

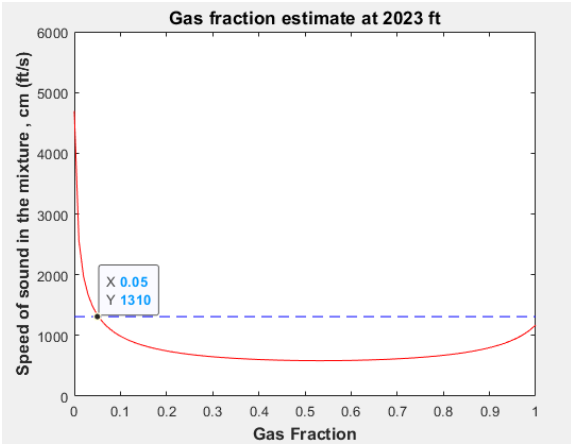


(a)

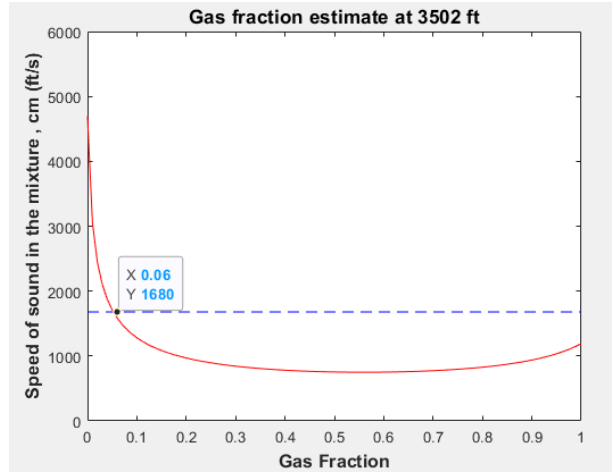


(b)

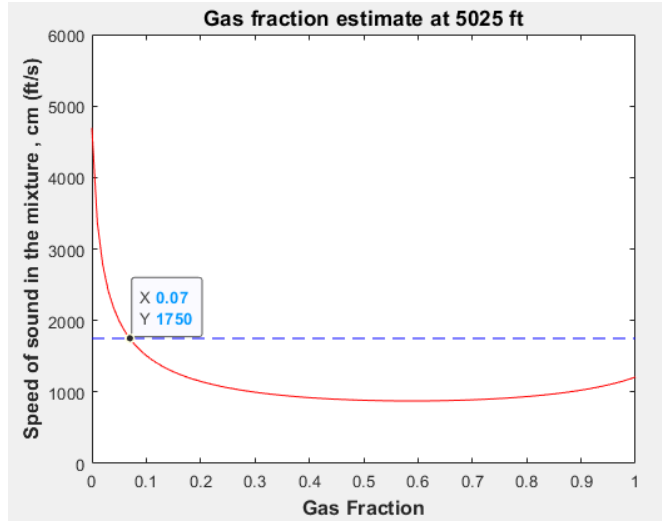
Figure 29: SOS estimation method from f-k filtered plots (a) is an example of an f-k filtered plot (b) is the same f-k plot as in (a) but with examples of red lines whose slopes were used to estimate the gas mixture SOS.



(a)



(b)



(c)

Figure 30. Gas fraction estimated from the SOS method at different depths.

4.3.2. Gas-liquid Interface Tracking (With-Circulation Case Studies)

The gas-liquid interface tracking workflow is demonstrated on DAS datasets from two different scenarios as described below.

Scenario 1: No circulation plus artificial noise

In the first scenario, three DAS traces representing the case when gas is at the bottom, middle, and top of the well, respectively, are used as test cases. In all cases there is no fluid circulation and gas

migrate in a static water-filled annulus. The 2D DAS data of the selected traces are shown in Figure 31 below; these will be referred to as the “signal data”.

Table 3: Summary of gas void fractions estimates for the case study.

Pressure difference estimation method				Speed of sound method	
Gas located	Gas-water mixture height (ft)	Pressure drop (Psi)	Gas fraction α_g	Speed of sound (ft/s)	Gas fraction α_g
Between 487 and 2023 ft	740	22.42	0.06	1310	0.05
Between 2023 and 3502 ft	774	19.78	0.07	1680	0.06
Between 3502 and 5025 ft	1058	25.18	0.08	1750	0.07

The 2D background noise data that will be added to the signal data is shown in Figure 32. A fraction of the background noise is progressively added to one of the 2D signal data (in Figure 31) as follows:

$$Input_{data} = 2D \text{ signal data} + \alpha * 2D \text{ background data} \quad 4.14$$

α is the fraction of the background noise that is added to the 2D signal data to evaluate the effect of the addition of noise on the efficacy of gas-liquid interface detection. Both the 2D DAS signal and background noise data are first normalized so that the values fall between 0 and 1 before the addition takes place. The $Input_{data}$ is then passed through the other steps of the analysis workflow shown in Figure 22, starting with the mirror boundary condition. Figure 33 – 35 shows the output of the analysis workflow described by Eqn. 4.14. above.

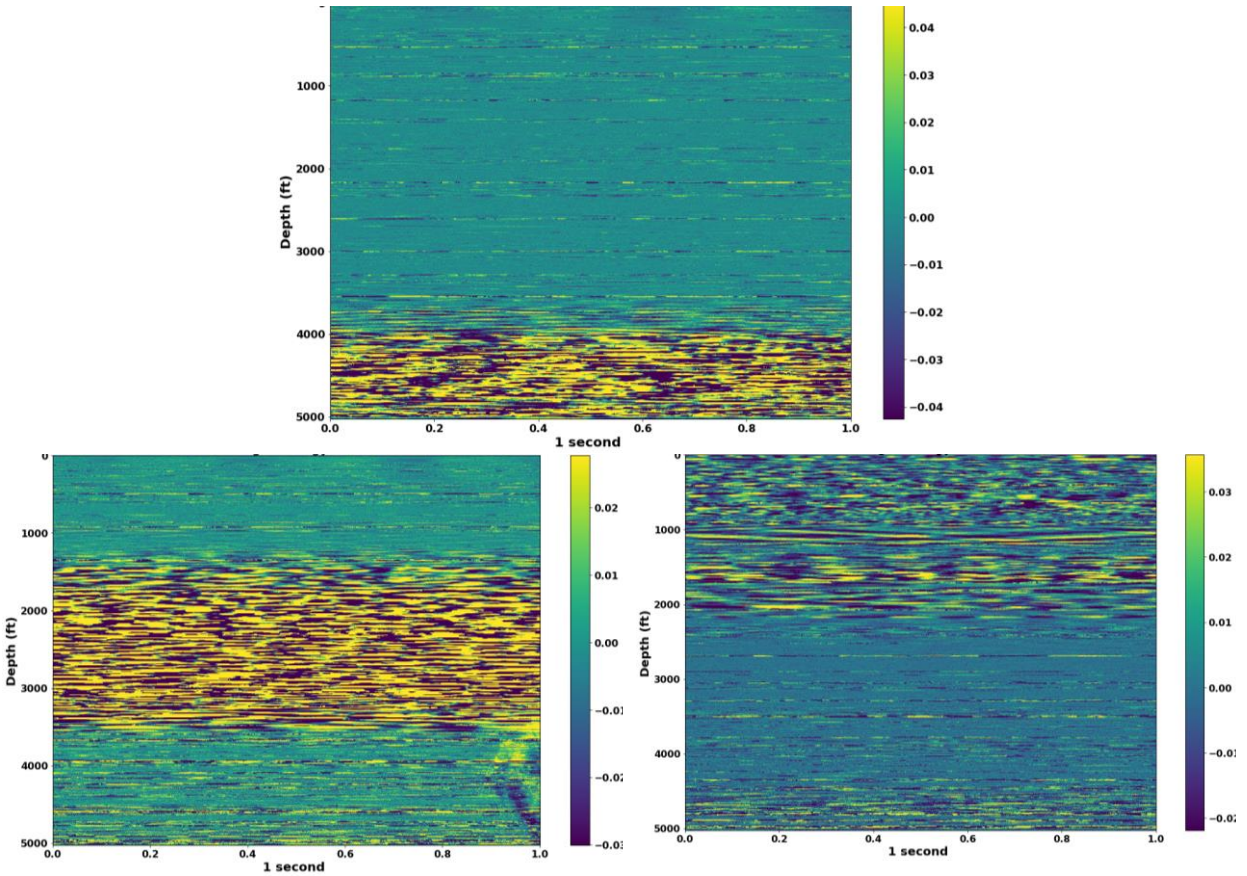


Figure 31. SEGY DAS samples used as test cases in scenario-1 corresponding to gas-water mixture location at the top, middle, and bottom of the annulus.

The approximate location of the gas along the well is characterized by the presence of relatively higher RMS values. The noise threshold for this background noise for each of the test cases is determined when the peak RMS is no longer in the depths containing gas. For the case when the gas is located at the bottom of the well, the noise threshold is 50%. The noise thresholds for when the gas is at the middle and top of the well are 30% and 10%, respectively. The noise thresholds are reduced as the gas travels to the top of the well. These results show that it is difficult to detect the gas location of gas directly from the 2D raw DAS data when the pumps are on.

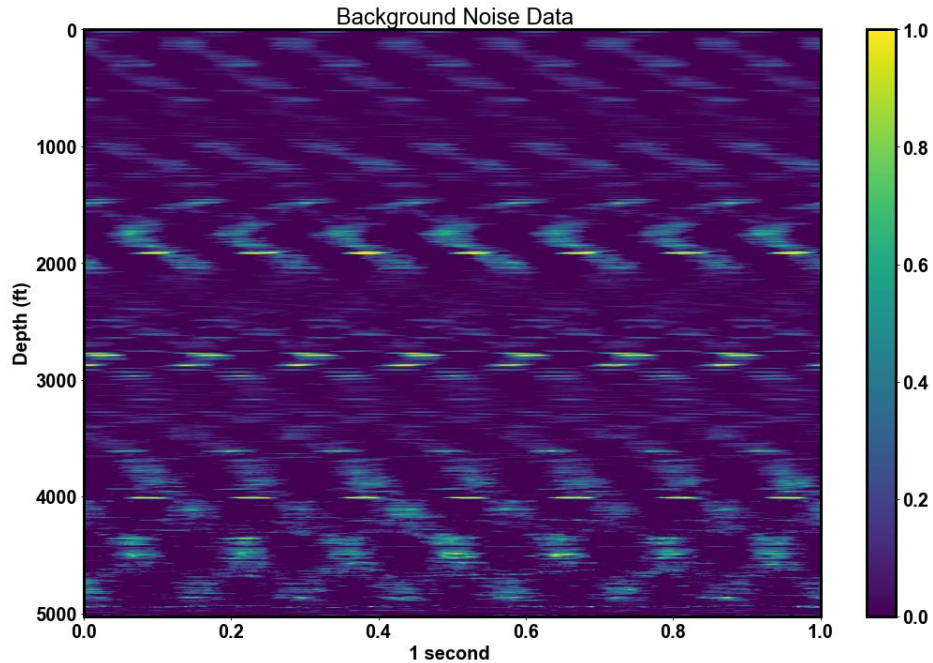


Figure 32. Background noise added to the signal data.

Scenario 2: With-circulation case study

In the second scenario, we demonstrate the interface detection workflow on a DAS data acquired in an experimental trial that involved 10 bbl. of gas injection while the water was continuously circulated at 100 gpm rate. The 2D DAS SEG Y data corresponding to this trial is shown in Figure 36. Here, the pumps are switched on to inject water down the tubing to circulate the gas up the annulus. As can be seen, it is difficult to clearly identify the location of the gas. However, after applying the correction shown in Eqn. 4.15 below, the results (i.e., the ability to identify the gas) were greatly improved, as demonstrated in Figure 38. The background noise used is the same as that in Figure 32, which was also used in scenario-1 described above.

$$Input_{data} = 2D \text{ signal data} - 2D \text{ background data} \quad 4.15$$

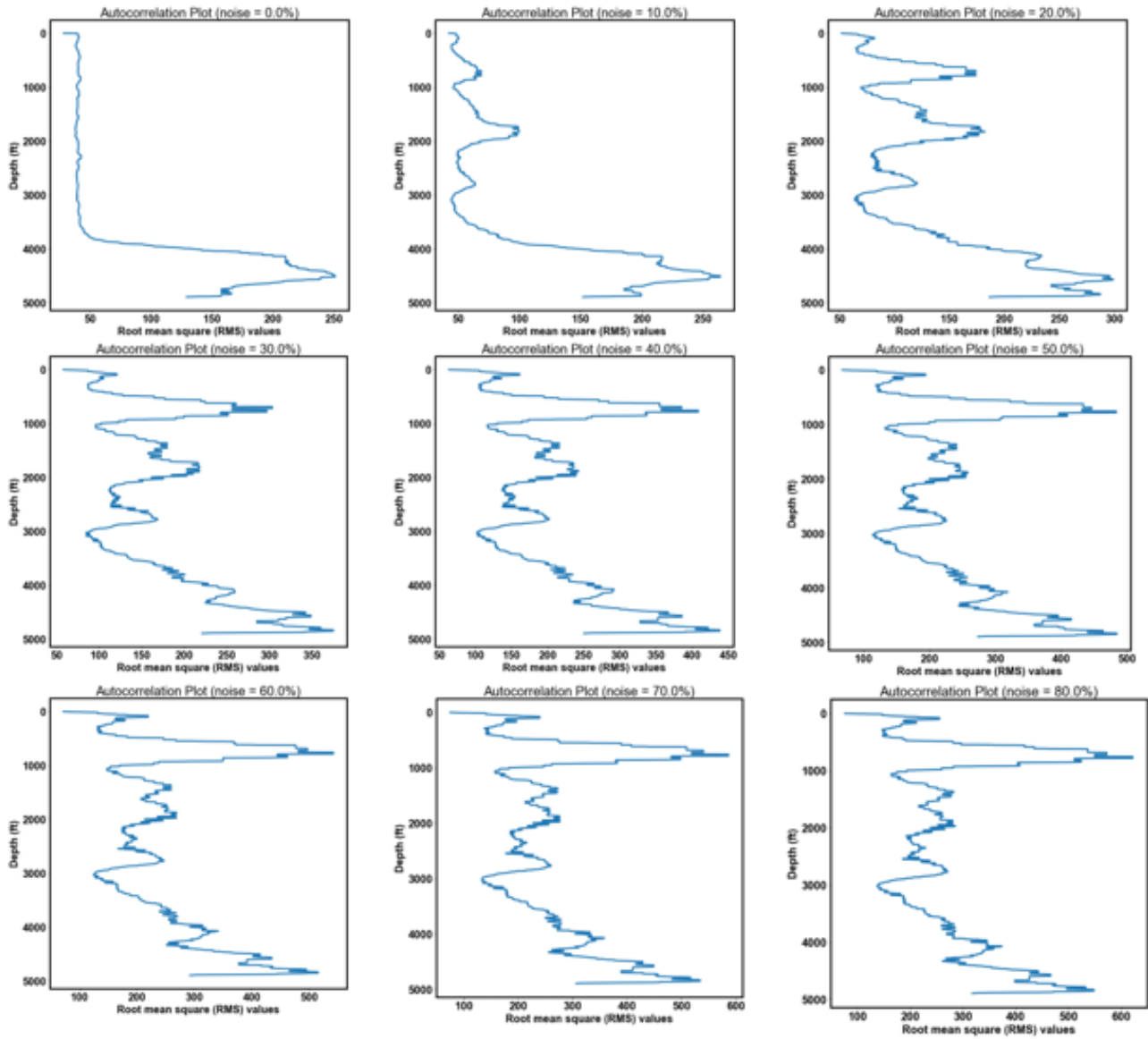


Figure 33: Effect of noise when the gas is located at the bottom of the well.

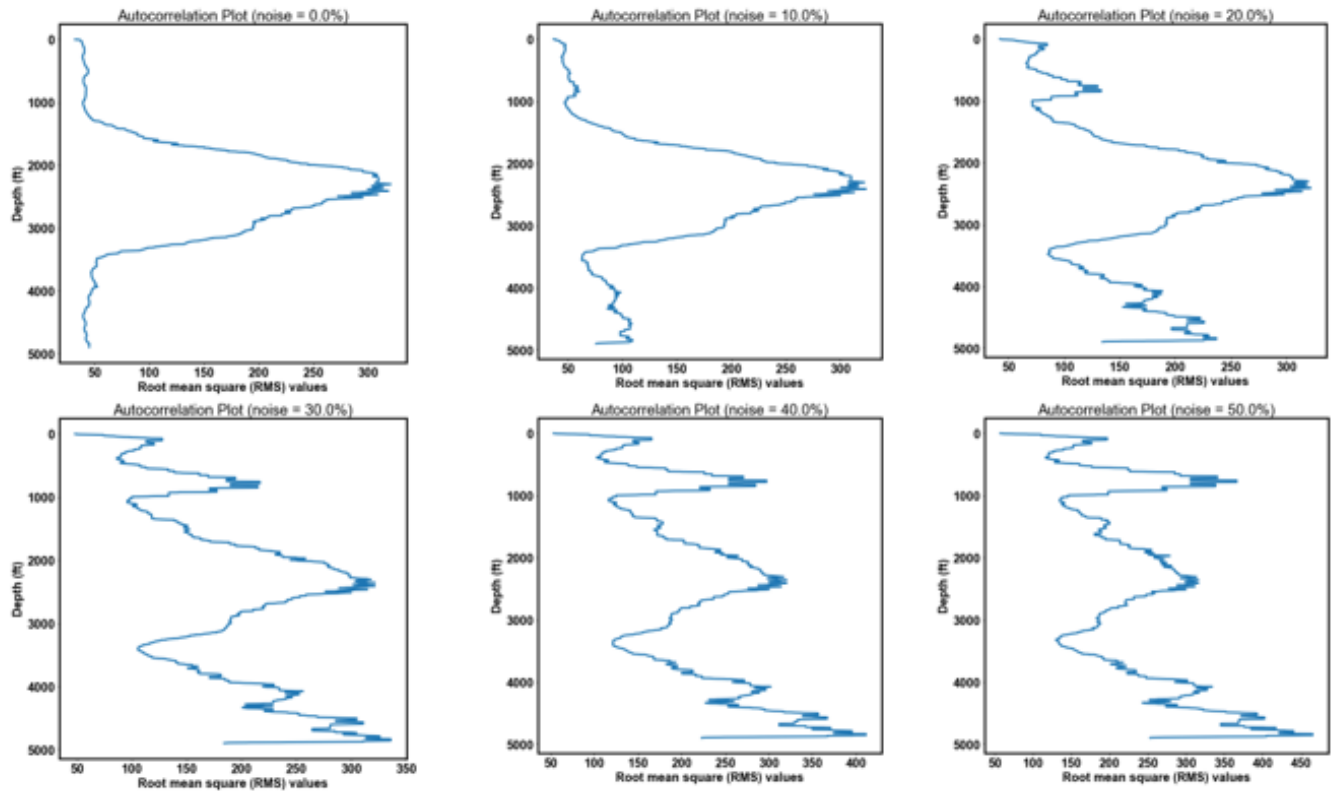


Figure 34: Effect of noise when the gas is located in the middle of the well.

The interface tracking workflow gave promising results when the gas was in the middle of the well but, unfortunately, did not give good results when the gas was located either at the bottom or top of the well. At the top of the well, the gas is more dispersed, and the signal is weak. While at the bottom of the well, the noise is very high; this could be due to the fiber degradation that we have observed in our well, as described in the next chapter.

4.4. Summary

Two independent techniques were demonstrated to estimate the gas void fraction using DAS data. The gas void fraction results were within the range of acceptable error uncertainties. The findings of our research will be beneficial to improve and validate fiber-optics-based production logging

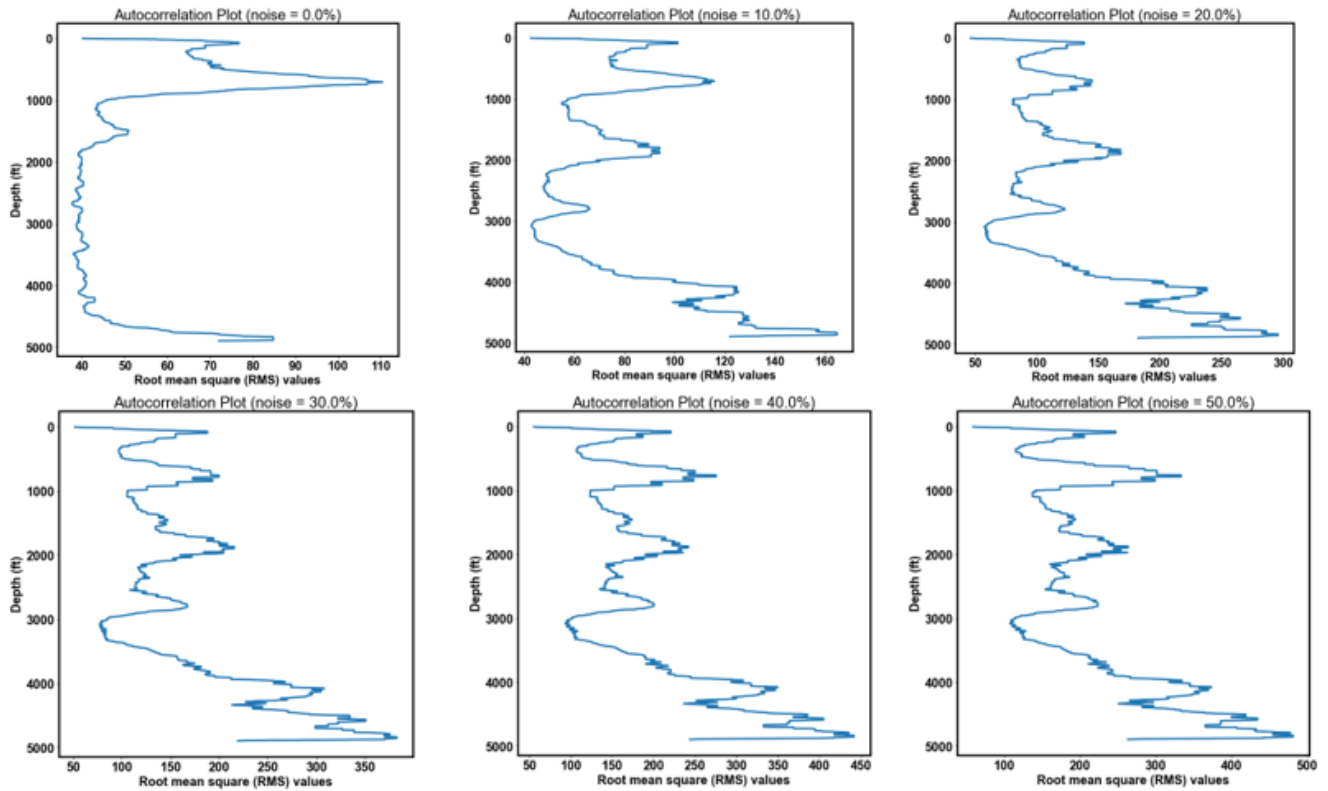


Figure 35. Effect of noise when the gas is located at the top of the well.

algorithms, detection, and quantification of gas leak volumes in the wellbore, as well as pipeline flow monitoring. The VBE workflow was also applied for gas-liquid interface tracking in noisy DAS data. The results show that the background noise threshold (at which the workflow is unable to detect the gas-liquid interface) for the analyzed datasets could range from 10-50%, with 50% being at the bottom of the well. Applying the analysis workflow on the DAS data with-circulation (i.e., pumps on) test cases only gave promising gas location identification when the gas when present in the middle of the well likely due to the low SNR at the bottom of the well due to fiber degradation (discussed in the next chapter) and extremely dispersed gas at the top.

Good results were obtained using the proposed analysis when the pumps are off. These scenarios are common in the oil industry operations where using DAS vibration data can still provide value, for instance, during drilling operations, no circulation cases are observed after drilling a stand of

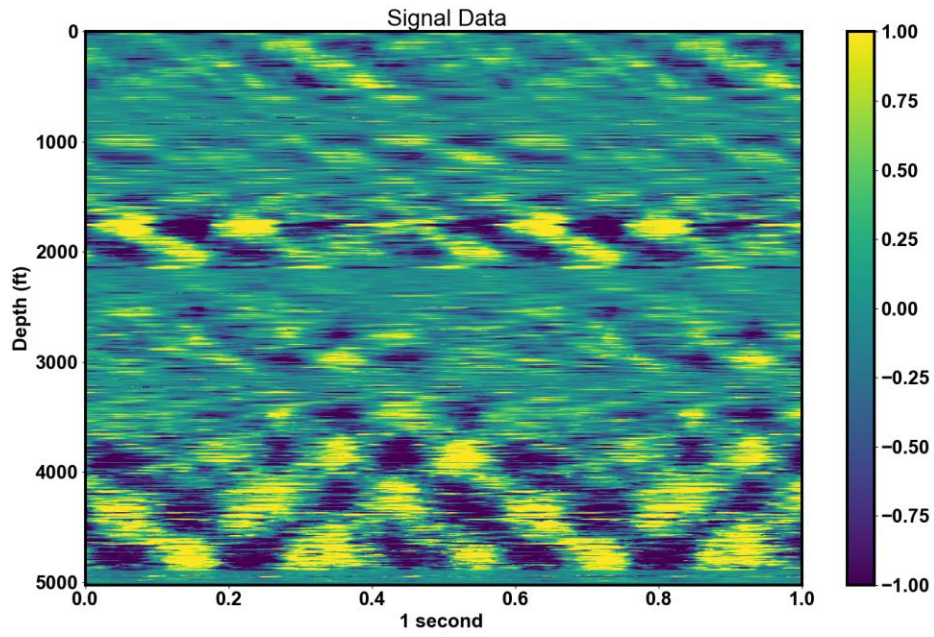


Figure 36. 2D DAS SEGY when the gas is located in the middle of the well (between 2500 to 3000 ft).

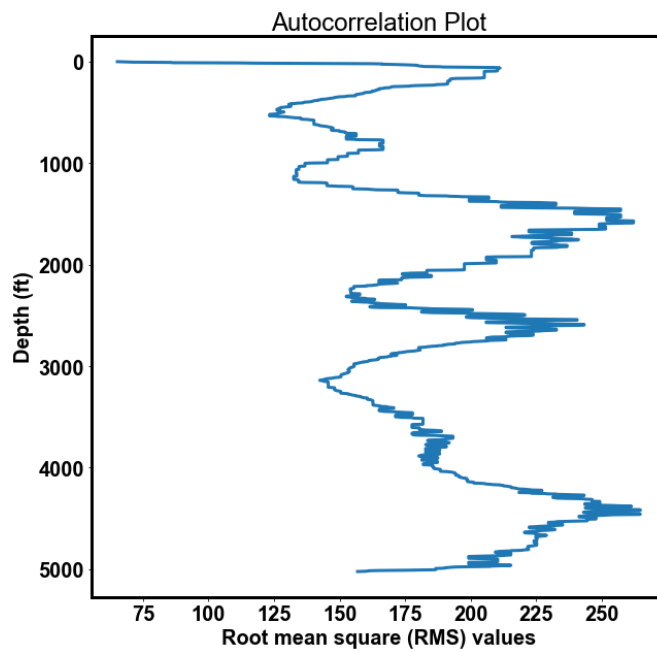


Figure 37. The result of applying the VBE workflow on the 2D data.

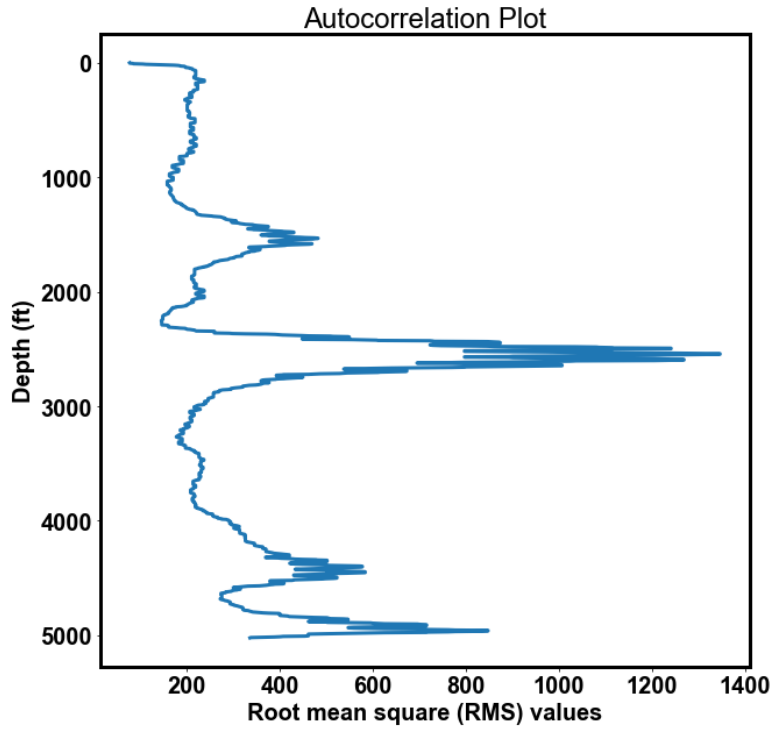


Figure 38. The result of applying the VBE workflow on the raw 2D data minus the background noise.

drill pipes (approximately 90 ft); this is to allow the drilling crew to make connections. This time window provides a great opportunity for us to apply the workflow and detect any gas ingress and their locations in real-time.

Chapter 5. Fiber Degradation Analysis and SNR Estimation

5.1. Introduction

The main objective of this chapter is to analyze the unexpected degradation observed in both the single-mode and multimode fibers, which are in a low-temperature (<130 °F) and low-pressure (<3500 psi) environment in the test well used in this study. A root-cause analysis was performed to understand the main cause of this degradation as well as to study the impact of the degradation on the DAS and DTS data quality over time, both qualitatively and quantitatively.

There are only a few case studies involving fiber degradation in the field. Blount et al. [70] described a fiber-optic health monitoring scheme used to explain DFOS failures in numerous instrumented wells, principally through time-lapsed OTDR measurements. OTDR traces in the problematic fiber-optic cables showed a variety of failure scenarios, including hydrogen darkening, fiber bending, and a cable breach. Oulundsen et al. [71] developed ways for creating low-loss fibers in a hydrogen-rich, high-temperature environment. One way is to coat the fiber with a hermetic material, the most common of which is carbon. Because the carbon layer is substantially less permeable to hydrogen than other coating materials, the rate of hydrogen diffusion into the fiber is significantly slower. However, using carbon has two disadvantages: (1) it loses its hermeticity at temperatures above 170°C , and (2) hydrogen will seep through the carbon layer and reach the core fiber over time. The second approach is to coat fibers with materials that can significantly reduce the impacts of OH absorption peaks, such as polyimide, which can operate at temperatures as high as 300°C with no signal deterioration at the relevant wavelengths. However, losses caused by free hydrogen will continue to occur. When exposed to a high-temperature hydrogen-rich environment, the pure silica core graded-index multimode fiber cables demonstrated much less induced attenuation than Ge-doped multimode fiber. The fundamentals of

macrobending and microbending in optical fibers were outlined by Jay et al. [72]. They looked at how mode field diameter (MFD) and wavelength affected macrobending. They discovered that for fibers with high MFD, attenuation was constant below a certain wavelength and rapidly rose above that wavelength. Lower MFD fibers showed a significantly diminished response following the wavelength cut-off. To design a fiber with a reduced mode field diameter, the refractive index difference between the core and cladding must be increased while the core diameter must be decreased. The "MAC number" is the MFD to fiber cut-off wavelength ratio. They also discovered that when a particular "MAC number" was exceeded, attenuation increased exponentially. In their work, they also examined the standards for measuring macrobending and microbending.

Other research groups have investigated employing attenuation losses as a sensing technique. Guzowski [73], for example, investigated the use of microbending as a pressure-sensing method. Based on the fiber microbending principle, Wu et al. [74] suggested a system architecture for monitoring concrete cracks. In the sensitized fiber sensor network, a quantitative link was established between optical loss and crack width. Njegovec et al. [75] exploited the microbending technique to create an optical fiber sensor for detecting and localizing corrosion events on metal surfaces. Zheng et al. [76] created an optical fiber crack sensor based on macrobending loss to detect crack opening displacement. Cheng et al. [77] developed an optical splitter-enhanced U-shaped-wound fiber macrobending loss crack sensor. Lopez et al. [78] created a distributed fiber-optic bending sensor for detecting petroleum hydrocarbons using the coherent optical frequency domain reflectometry approach. A sensitive polymer was utilized, which swells selectively in the presence of hydrocarbons and causes bending losses in the fiber. Roman et al. [79] demonstrated a thin-core high-numerical aperture fiber with minimal macrobending loss that is suited for applications that require the fibers to bend sharply.

One of the novelties aspects of our methodology is that the exact specifications of the fiber were documented in detail, making it conceivably the only field-scale case study examining single-mode and multimode fiber degradation over time. The manufacturers and end users of fiber optics would benefit from having a better understanding of the reasons behind fiber degradation and from being able to apply what they have learned to new projects. This study is also unique in that it examines multimode fiber degradation utilizing time-lapse measurements of temperature-sensitive (TTS) and non-temperature-sensitive (NTS) Raman backscatter patterns. Additionally, we have examined the impact of fiber deterioration in both water- and oil-based drilling mud wellbore fluids. This becomes extremely important to assess the effect of fiber exposure during wellbore drilling and completion. Using DFOS to monitor gas kicks during drilling, completion, and workover activities is being explored by both industry and academia. However, the performance or degradation of the installed fiber in the presence of drilling and completions fluids (typically, water- or oil-based muds) has not been explored. Additionally, this chapter seeks to close this information gap. Potential Causes of Fiber Degradation. In fused silica glass fiber, signal degradation is frequently caused by optical losses caused by scattering, bending (microbending and macrobending), attenuation, dispersion, absorption, and optical splices and connectors. These phenomena are explained shortly below.

Attenuation: This is the measurement of optical energy loss as it goes through the fiber. Attenuation is often measured in decibels per kilometer (dB/km). As seen in Figure 39, these losses are wavelength-dependent, and the value of the attenuation is highly dependent on the fiber material and manufacturing tolerances. Scattering and absorption both contribute to attenuation.

Scattering Loss: When light interacts with the inhomogeneities within the glass core, it scatters, which is usually what causes normal loss in the fiber cable. When energy is moved from the

dominant mode to the adjacent mode, linear scattering takes place. The linear scattering in the dominant mode is directly correlated with the input power. The scattered wave's frequency does not change in a linear scattering process [6]. There are two different linear scattering mechanisms: Mie scattering and Rayleigh scattering. The primary type of linear scattering brought on by smaller-than-wavelength scatterers created during the fiber production process is known as Rayleigh scattering. The inverse of the fourth power of wavelength is directly related to the Rayleigh scattering coefficient [81]. Mie scattering occurs in inhomogeneities such as core-cladding refractive index variations over the length of the fiber, impurities at the core-cladding interface, strains or bubbles in the fiber, or diameter fluctuations. In commercial fibers, the effects of Mie scattering are insignificant, and they can be reduced by carefully removing imperfections from the glass material and controlling the quality and cleanliness of the manufacturing process. Non-linear scattering losses occur in an optical fiber that is operating in non-linear mode when the optical power at the output of the fiber does not change proportionally with the power change at the input of the fiber. Stimulated Raman scattering and stimulated Brillouin scattering are two categories of non-linear scattering losses caused by the nonlinearity of a medium.

Absorption: The composition of the fiber and its fabrication results in absorption losses which depend on the wavelength of light. Electronic UV (ultraviolet) absorption bands that occur at shorter wavelengths (with high values around 100 nm) and molecular IR (mid-range infrared) absorptions are the main contributors to intrinsic absorption losses. The tails of the electromagnetic (EM) spectrum's UV and IR absorption bands extend into the visible light region. [82]. The theoretical low-loss wavelengths are around 1550 and 1310 nm, which are two commonly utilized laser wavelengths [6]. Impurities in the fiber during manufacture cause extrinsic absorption. When metal impurities such as iron, nickel, and chromium are introduced into the fiber during the

fabrication process, absorption may occur because of metal ions transitioning to higher energy levels. Metal ion losses can be decreased to a very low level by purifying the glass mixture to an impurity level of less than 1 part per billion (ppb).

Hydrogen Darkening: The exposure of an optical fiber to hydrogen can result in the degradation of the fiber's performance and optical losses at specific wavelengths due to the absorption of a variety of hydrogen-related species [83]. These losses typically originate from two sources: the reaction of hydrogen with fiber defects and free molecular hydrogen (H_2) dissolved in silica. The magnitude of these losses depends on temperature, hydrogen concentration, partial pressure of hydrogen, and exposure time [84]. Hydrogen can react with the glass matrix to form hydroxyl ions (OH^-) that interfere with the passage of light through the glass. Absorption losses occur in the presence of OH^- , which can result in significant optical attenuation at specific wavelengths.

This typically happens at defect sites along the fiber where the oxygen atoms are not fully bonded. These losses are permanent since the chemical reaction cannot be reversed. Absorption peaks due to OH^- are strong at 1383 nm and, to a lesser extent, at 945 nm and 1240 nm (Figure 40). However, the OH^- absorption band is narrow enough that ultrapure fibers can achieve losses of less than 0.2 dB/km at 1550 nm. The addition of germanium oxide to the glass core alters the effect of OH^- impurities by creating additional absorption peaks at slightly different wavelengths. When fused silica glass fiber is exposed to hydrogen gas, the hydrogen molecules can also diffuse through the polymer materials to the fiber cladding and core at room temperature just within days. These H_2 molecules will occupy interstitial sites that have specific absorption peaks [71]. These effects cause a reversible loss because once the fiber is removed from the hydrogen environment, the hydrogen molecule can diffuse back out. The rate of response and recovery depends on the temperature. Figure 40 shows the absorption spectrum resulting from molecular hydrogen

dissolved within silica optical fiber illustrating a fundamental peak at 2420 nm and the first overtone at 1240 nm. Other absorptions of interest can be observed at 1590 nm and 1640 nm [84]. The resulting fiber losses can reach hundreds of decibels per kilometer, which makes it unusable for any optical transmission application.

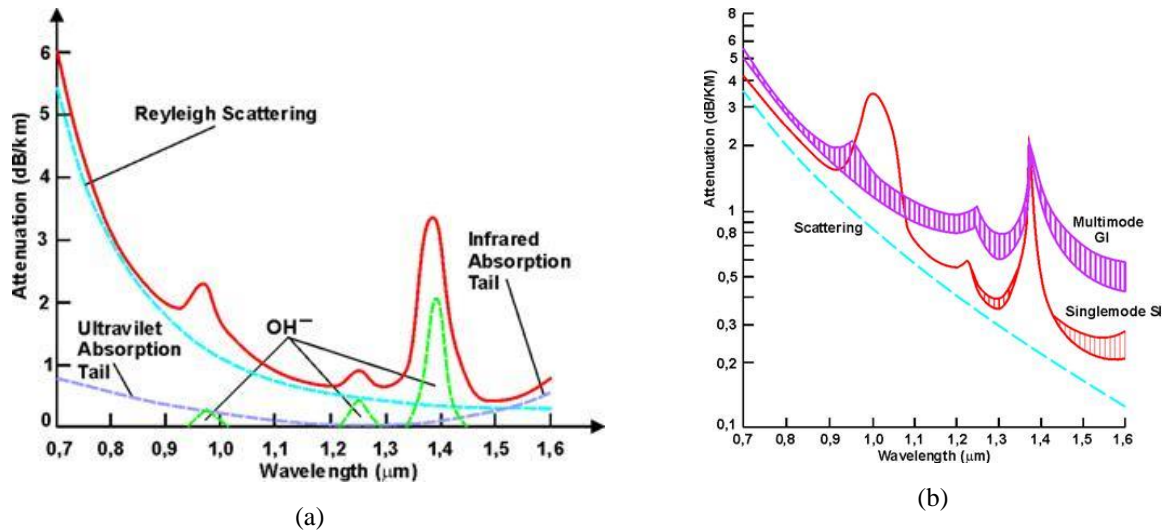


Figure 39. (a) Attenuation in silica optical fiber as a function of wavelength (b) Spectral attenuation in Graded index (GI) multimode and Stepped Index (SI) multimode fibers [82].

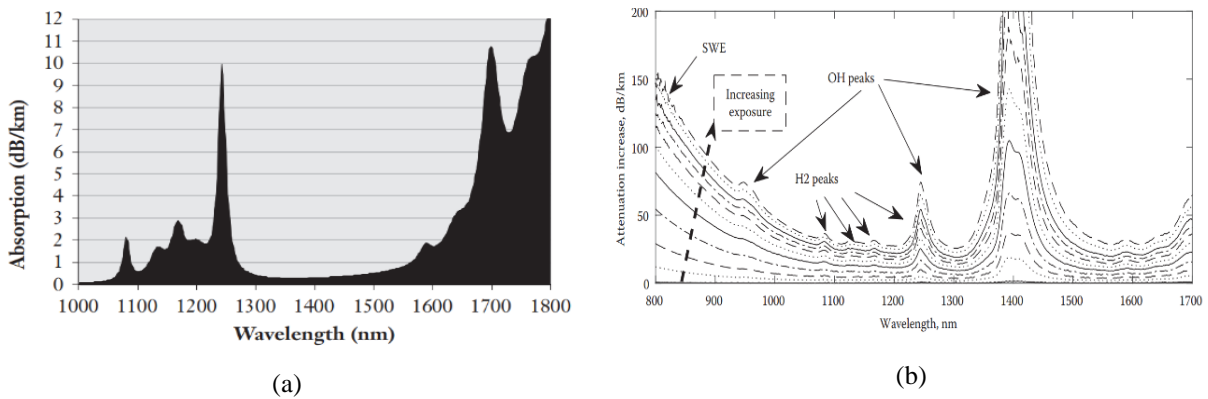


Figure 40. (a) Absorption spectra of molecular hydrogen [84] (b) Attenuation profiles with increasing hydrogen exposure [6].

The hydrogen that interacts with optical fiber can come from a multitude of sources, including ambient atmospheric hydrogen, evolution or dissolution from cable material (e.g., hydrocarbon polymers and metals), a galvanic reaction between dissimilar metals in the cable, general

oxidation/corrosion, and due to sulfate-reducing bacteria, or direct fluid influx due to poor termination or hole in the fiber control line [85]. Hydroxyl ions may be formed due to the dissociation of water into hydronium ions (H_3O^+) and OH^- . However, very few water molecules undergo this dissociation (about one water molecule in half a billion dissociates into an OH^-) [86]. Therefore, if water touches the fiber, there is a small chance of the OH^- diffusing through the coating through the cladding to the core, thereby causing some adverse effects.

One way to prevent hydrogen darkening is the application of hermetic coatings on the fiber surface to create a hydrogen barrier. Metal, ceramics, and carbon coatings have been explored for this application. Of these, carbon coatings are considered the most attractive, especially at temperatures above 100°C , as shown in Figure 41 [87]. At these temperatures, the saturation lifetimes with respect to hydrogen ingress are on the order of years, and the mean strength is sufficient for most applications. Hydrogen-capturing gels have also been used to buffer the fiber, and other proprietary techniques may be used to prevent hydrogen atoms from reaching the glass fiber via the cable sheath [88].

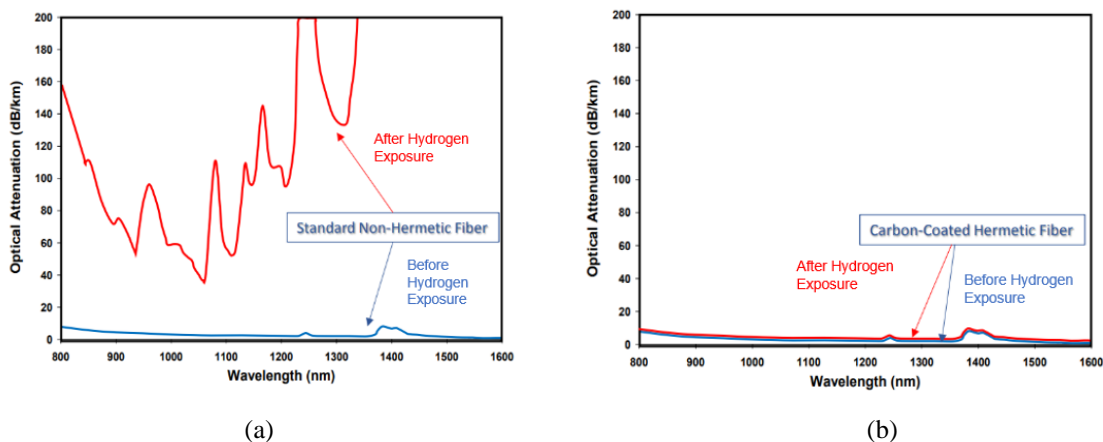


Figure 41. (a) Standard graded index multimode fiber before hydrogen exposure (b) carbon-coated hermetic fiber after hydrogen exposure [87].

Bending Losses: The optical signal traveling through the fiber can also be affected by bending losses, as illustrated in Figure 42. There are categorized into two types, namely: macrobending and microbending.

Macrobending Losses: This typically occurs when the fiber cable is folded or physically bent, and the curvature of the bend is larger than the fiber diameter, as shown in Figure 42a. When this occurs, there will no longer be a total internal reflection at that point, as the angle of refraction is now less than the critical angle; hence light will leak out through the cladding. The degree of light leakage is proportional to the magnitude or radius of curvature of the bent fiber cable. The loss due to macro bending is wavelength-dependent, and the value of the loss will increase at higher wavelengths. OTDR traces obtained at longer wavelengths (such as 1625 nm) can be used as indicators for macrobending [72]. In general, macrobending losses should be insignificant for bends up to 10 times the outside diameter [81].

Microbending Losses: This type of loss is caused by very small-scale bends in the core-cladding interface (typically <1 mm) along the waveguide [72]. These localized bends can develop during the deployment of the fiber or can be due to local mechanical stresses placed on the fiber, such as stresses induced by cabling the fiber or wrapping the fiber on a spool or bobbin [81]. They can also form because of defects in the manufacturing process. Other potential causes of microbending would be a differential expansion of the optic fiber and the surrounding coating material. If the fiber gets cold, it will shrink and get shorter. If the core/cladding is not shrinking at the same rate, then there is a possibility of microbending. Irregularities in the coating materials, coating surface slickness, the reaction of the coating material with some solvents such as isopropyl alcohol, and the presence of particles such as those in the pigments of color coatings, may result in inconsistencies in how mechanical stress is transmitted through the polymer coatings to the

fiberglass which can contribute to microbending losses. External factors, such as temperature and humidity, can also affect the sensitivity of the fiber to experience this type of loss. Microbending exhibits attenuation across a large wavelength band and shows less wavelength dependency, as shown in Figure 42b. The set of perturbations that causes bending can be viewed as a spectrum. Some factors that can contribute to microbending loss are described in the equation below [72].

$$\lambda = N \langle h^2 \rangle \frac{a^4}{b^6 \Delta^3} \left(\frac{E}{E_f} \right)^{3/2} \quad (5.1)$$

Where λ is the attenuation, N is the number of bumps of average height h per unit length; a is the radius of the core, b is the overall fiber diameter, Δ is the difference in the refractive index while E and E_f are the modulus of elasticity of the fiber and coating, respectively. As can be seen from the equation above, several parameters can affect microbending. Smaller core size and large refractive index differences can contribute to reducing microbending attenuation.

Dispersion Losses: This type of optical signal loss results from the spreading out of a light pulse as it propagates down the fiber, which leads to a reduction in the effective bandwidth available for optical transmission. Dispersion in optical fiber includes modal dispersion, chromatic dispersion, and polarizing mode dispersion. Of these, the modal dispersion is not a problem in single-mode fibers since there is only one light mode that can travel in the fiber.

Connector and Splice-induced Losses: One of the major extrinsic contributors to optical signal losses are connectors and splices. No matter how good the connection or splicing, these losses are inevitable. Connector losses or insertion losses are the losses of optical power resulting from the insertion of a device in a transmission line or optical fiber. Mechanical misalignment of connectors scratched or pitted glass end face, or foreign debris on the fiber end face can be contributed to these losses.

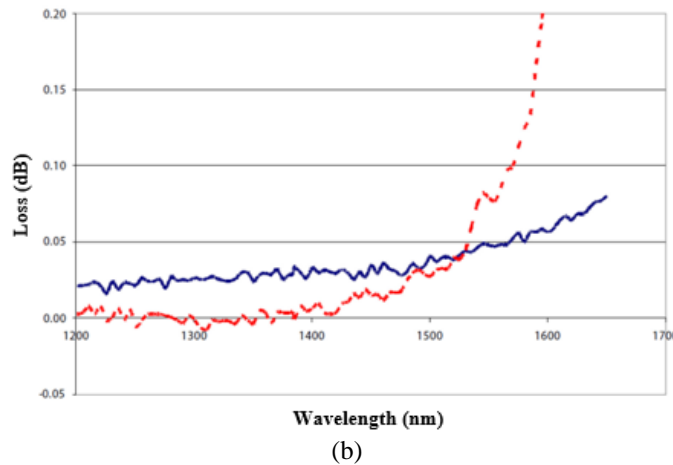
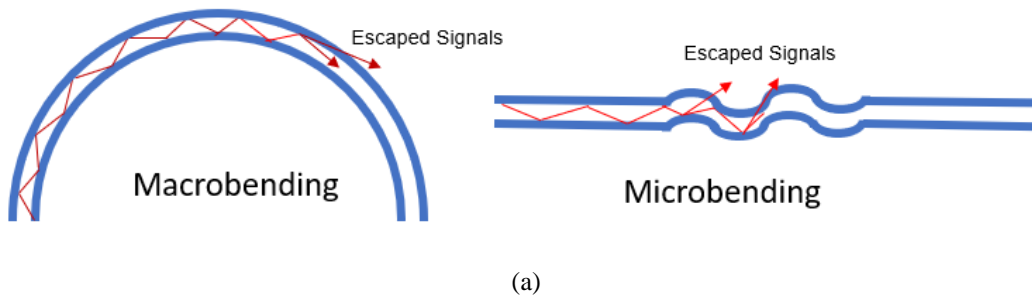


Figure 42. (a) Schematics of macrobending and microbending (b) The wavelength dependency of microbending and macrobending [72].

The quality of the fiber splicing affects the splicing losses. Acceptable fusion splicing losses of multimode fiber range from 0.1 to 0.5 dB, while they are typically less than 0.05 dB in single-mode fiber [89]. The typical accepted range for multimode connector losses is between 0.2 to 0.5 dB and less than 0.75 dB for single-mode connectors. The field engineer or technician responsible for the fiber installation is responsible for ensuring that these losses do not contribute to exceeding the optical budget.

5.2. Fiber Degradation Analysis Methodology

The optical budget or the link budget is the estimation of the two-way loss of optical signal considering all the signal losses experienced along the optical fiber path [90]. This is usually done to ensure that the signal that returns to the receiver is not too weak, which will then make it difficult

to be separated from the background or instrument noise. In the context of DFOS, the cumulative signal losses due to factors intrinsic and extrinsic to the optical fiber should not exceed the maximum loss permitted by the DFOS acquisition unit or interrogator used. As optical losses are inevitable, there is a maximum level of an acceptable loss outlined for various processes. For the test well setup used in this study, the maximum cumulative losses (connectors, splice, and downhole fiber) for the DTS acquired using the multimode fiber should not exceed 12 dB while the maximum cumulative loss for the DAS acquired using the single-mode fiber should not exceed 5 dB [91]. In addition, the measured attenuation along the installed downhole multimode fiber should not exceed 3 dB/km and 1 dB/km for 850 nm and 1300 nm wavelengths, respectively. For the single-mode fiber, the measured attenuation should not exceed 0.5 dB/km and 0.4 dB/km for 1310 nm and 1550 nm wavelengths, respectively [89]. To ensure that the optical losses in the DFOS installed in the test well are within the acceptable limits as described above, multi-wavelength OTDR measurements and optical backscatter signal analysis was performed.

5.2.1. Multi-wavelength OTDR Measurements

OTDR is optoelectronic equipment used to characterize the total two-way signal losses experienced by the light traveling through the fiber. It provides a plot of distance versus signal level, which is useful for locating defects and quantifying signal losses at different points along the fiber. Since many of the optical loss mechanisms are wavelength-dependent, as described previously, most OTDRs allow measurements at different laser wavelengths, pulse widths, and distance ranges. Time-lapse OTDR measurements were taken in the single-mode and multimode fibers installed in the test well to measure cumulative losses over time across the fiber length in the well. There is a splice and connector at the junction box at the wellhead and the single- and multimode fibers are terminated using epoxy inside the bottom of the DFOS control line (at 5025

ft). There are no other optical splices or connectors along the DFOS control line in the tubing. All the OTDR plots were visualized starting from the wellhead splice (at 0 ft i.e., top of the test well) up to the fiber termination point at 5025 ft (which is indicated by the far-end Fresnel reflection). Repeated OTDR measurements were acquired at 850 nm and 1300 nm for the multimode fiber to encompass the DTS interrogator probing wavelength of 1064 nm. Similarly, the OTDR in the single-mode fiber was acquired at 1310 and 1550 nm wavelengths, considering the operating wavelength of 1550 nm for the DAS interrogator. Once the degradation was observed in the fibers in the form of higher-than-expected optical losses, OTDR at other wavelengths was also acquired to conduct a root-cause analysis, in addition to the conventional wavelengths employed in single-mode and multimode fibers. The special wavelengths included 1244 nm, 1310 nm, 1383 nm, and 1625 nm. Increased losses at higher wavelengths, such as 1625 nm, can be used as an indicator for possible macrobending issues. The 1244 nm wavelength is used for measuring the “water peak” region of high attenuation in a fiber’s spectral attenuation curve. If the water peak attenuation grows due to unusual chemical activity within the fiber, then the 1310 nm operating band can also become affected [92]. The OTDR readings at 1383 nm can be used as an indicator for permanent hydrogen damage as the loss values will be higher at these wavelengths than at nearby lower wavelengths in the case of hydrogen-induced degradation.

5.2.2 Raman Spectra Analysis

The DTS interrogator deployed in this study utilizes the anti-Stokes and Stokes components of the Raman spectrum to evaluate the distributed temperature profile. Therefore, the degradation in the multimode fiber (used for DTS acquisition) was also evaluated by analyzing the change in the Raman backscatter profiles over time. The Stokes component of the Raman spectrum is non-temperature sensitive (NTS) and mainly contains the fiber loss information, while the anti-Stokes

component of the Raman spectrum contains temperature-sensitive (TTS) information which is affected by both the temperature and the optical fiber losses. Eq. 2 shows how the DTS temperature profiles are computed for a single-ended multimode fiber installation from the NTS and TTS band trace data. The temperature calculated by the DTS interrogator at any point x ($Temp_x$) along the fiber is a function of the Stokes and the anti-Stokes ratio at x to the Stokes and anti-Stokes ratio in the reference coil (c), the temperature of the reference coil (RCT), the fraction of fiber length (Z), and a sensitivity parameter (SLE). The equation also shows how the light loss in a single-ended multimode fiber is corrected in a single laser pulse DTS interrogator by setting a differential loss correction or DLC factor. The DLC factor inputted assumes that the optical loss is constant along the fiber which may not be valid in some cases due to variations in fiber manufacturing, purity of the fiber, control bands during installation, fiber deterioration with time, new connections, etc. Over time, the single-ended temperature measurements can change as the light loss characteristic of the fiber changes due to fiber deterioration, etc. In this situation, the absolute accuracy of the DTS temperature profile can be corrected post-acquisition by calibrating the DTS temperature to a known gauge temperature using the DLC adjustment method.

$$\frac{1}{Temp_x} = \frac{1}{RCT} - \frac{\ln\left(\left(\frac{TTS}{NTS}\right)_x / \left(\frac{TTS}{NTS}\right)_c\right) * e^{(DLC*Z)}}{SLE} \quad (5.2)$$

As the fiber installation in the test well is single ended, if the fiber degradation is the same for the NTS and the TTS signals (in other words, there is no change in the differential loss), then the DTS temperature measurements are not impacted, and therefore correct. Consequently, to evaluate the degradation in the multimode fiber, the NTS and TTS signals over time were analyzed, and the observed DTS measurement was also compared with the temperature measured using the four downhole gauges in the test well

5.3 Fiber Degradation Analysis Results and Discussion

5.3.1 Multi-Wavelength OTDR Measurements

5.3.1.1 Multimode Fiber Analysis

At the time of DFOS installation in the test well in June 2019, the attenuation for the multimode DTS fiber was found to be 3.48 dB/km and 1.874 dB/km at 850 nm and 1,300 nm OTDR wavelengths, respectively for the total length (5025 ft) of the downhole fiber. As it has been reported in the literature [6], [70], [89] the fiber loss is wavelength dependent, and the optical fiber attenuation decreases with longer wavelengths. This means that the fiber attenuation and losses seen by the DTS interrogator unit operating at the acquisition wavelength of 1,064 nm would be lower than the values measured by the two-way OTDR at 850 nm wavelength but higher than the 1300 nm wavelength Figure 43a and Figure 43b shows the plot of the time-lapse OTDR acquisition obtained in Jun 2019, Jan 2022, and Feb 2022, recorded at 850 nm and 1300 nm, respectively. From the plots, we see an inflection point at roughly 2500 ft where the OTDR profiles start to deviate away from the initial profile at installation. The optical losses over time in the top half of the multimode fiber appear to be overlaid and have similar attenuation rates (indicating no significant change over time). However, the attenuation rate at the bottom half of the fiber appears to be increasing with time. The cumulative optical loss values for the OTDR profiles across the entire fiber and only the bottom half of the fiber length are summarized in Table 5 . The attenuation at 1300 nm is lower than those at 850 nm, which is expected because attenuation decreases as the probing light wavelength increase until certain wavelengths when the attenuation caused by infrared absorptions starts to increase.

To further understand the cause of increased degradation at the bottom part of the fiber observed during the periodic OTDRs, loss measurements at additional OTDR wavelengths were

acquired in June 2022, as shown in Figure 44. The attenuation values for both the total length and the bottom half of the multimode fiber are summarized in Table 6. If hydrogen darkening was causing the fiber degradation, the attenuation at 1244 nm would have been at least an order of magnitude higher than the attenuation at the other wavelengths. Similarly, if hydroxyl ion was the culprit, the attenuation at 1383 nm would have been at least an order of magnitude higher than the attenuation at the other wavelengths. In the hydrogen darkening example by Blount et al. [70], both free hydrogen and hydroxyl ions affected the fiber cable, and the attenuations at 1244 nm and 1383 nm were an order of magnitude higher than those at other wavelengths.

As recommended and observed by Oulundsen et al. [71], fiber-optic cables with carbon and polyimide coatings, similar to the one used in the fiber installed in the test well, are not expected to be affected by the presence of hydrogen in the range at which DTS operates (between 1014 nm to 1114 nm) and low-temperature conditions in the test well. Fiber degradation due to the ingress of wellbore fluid into the DFOS control line due to pin holes or poor termination can also be ruled out since no significant change in OTDR profile was observed when the fluid in the test well was switched from water to synthetic oil-based mud (OBM) in February 2022. The properties of the mud are shown in Table 7, and the particle size distribution of the solids in the OBM is shown in Figure 45. The ratio of the oil/water ratio of the mixture is 70/30. If there were fluid ingress into the DFOS control line, the pumping of fluid with solids with likely cause more abrasiveness of the fiber coating, which could greatly increase the attenuation. Comparing the multi-wavelength OTDRs taken before and after the mud switch did not show any dramatic change in the attenuation, which rules out fluid ingress as the likely cause of the observed fiber degradation and high optical losses.

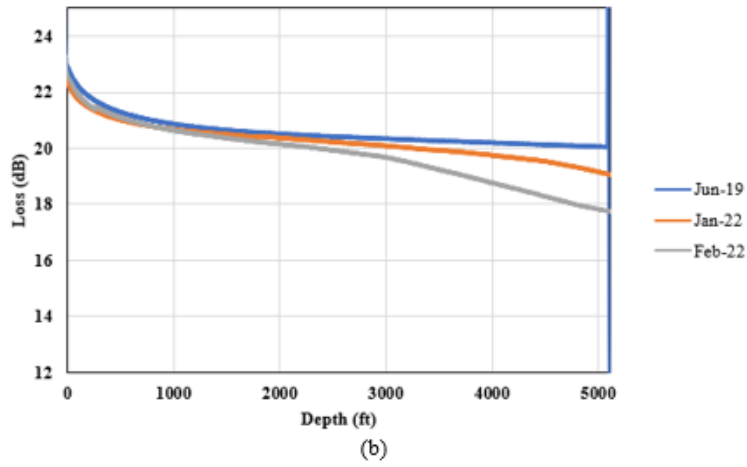
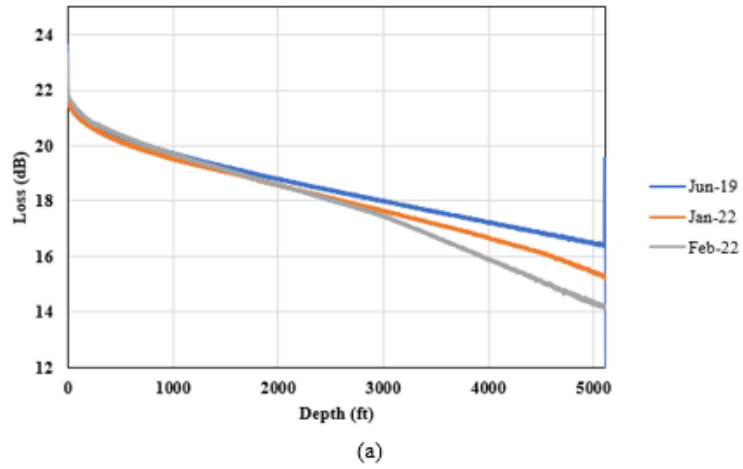


Figure 43. Time-lapse OTDR for multimode fiber at (a) 850 nm and (b)1300 nm.

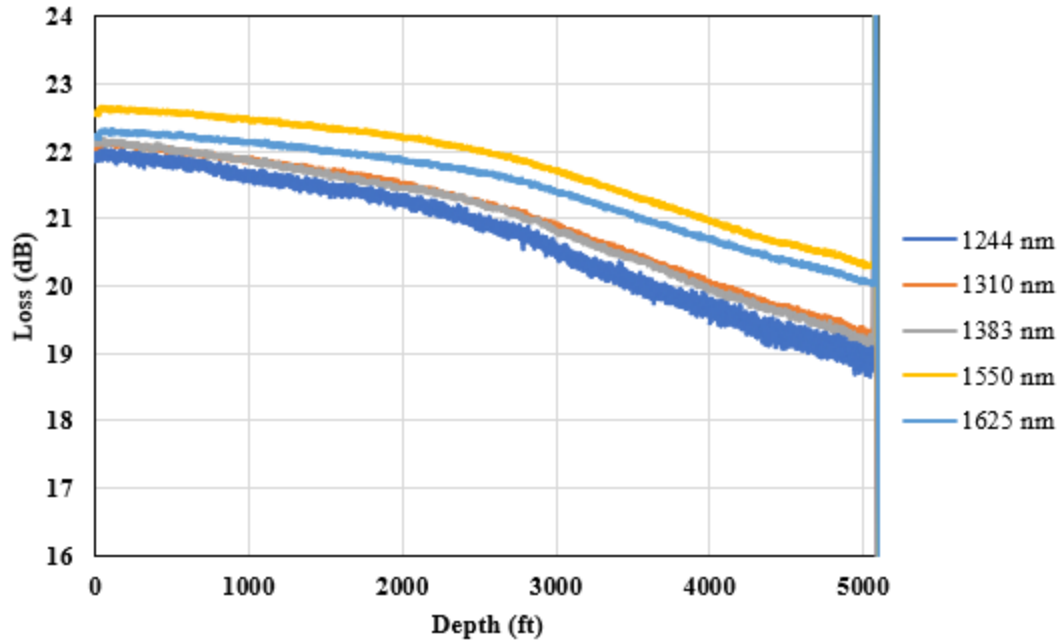


Figure 44. Multi-wavelength OTDR for the multimode fiber taken in Jun 2022.

If macrobending was the main cause of the degradation, increased losses would have been observed at a higher wavelength (1625 nm). For example, the macrobending example by Blount et al. [70] is not observed in our case. The multi-wavelength analysis suggests that macrobending and the presence of hydrogen or hydroxyl ions cannot be blamed for the observed degradation. Since there are no optical connectors or splices along the fiber installed along the tubing in the test well, microbending appears to be the only other possible cause of the observed degradation.

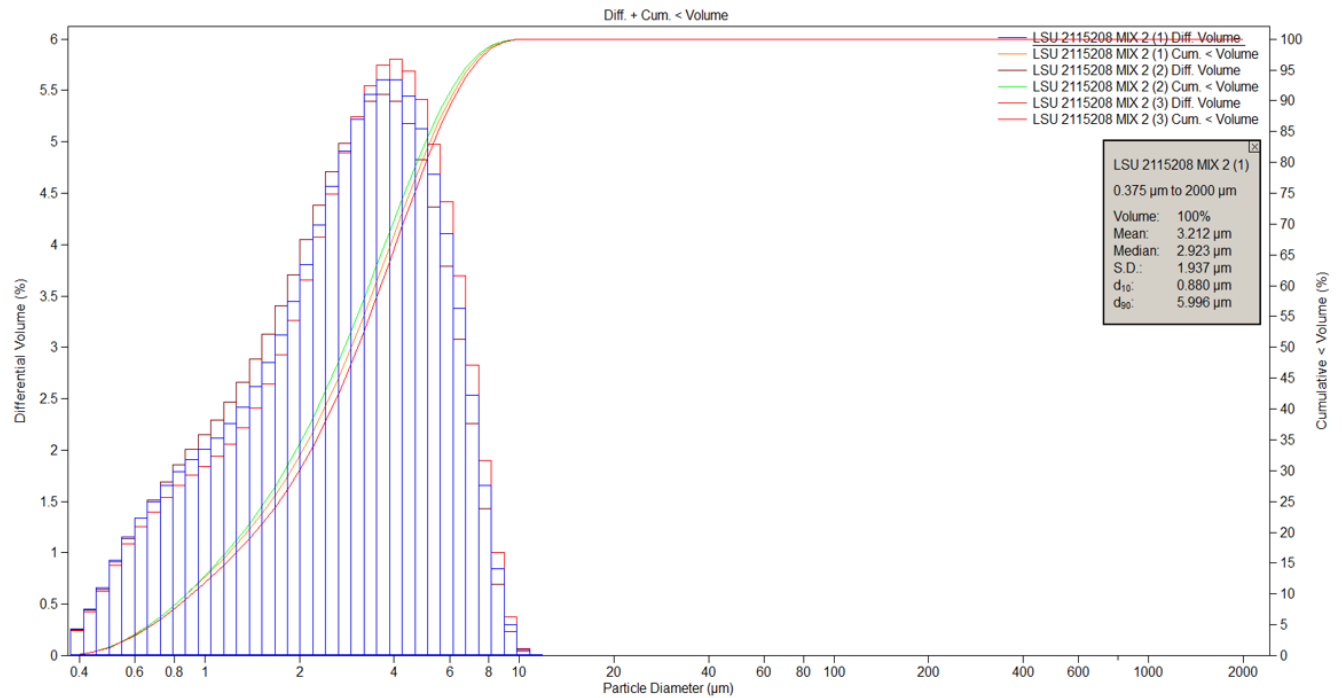


Figure 45. Particle size distribution of the mud in the well.

Table 4. Specification for the single-mode and multimode fibers installed in the test well.

	Single mode	Multimode
Material		
Hermetic coating	Carbon	Carbon
Coating	Polyimide	Polyimide
Core	Pure Silica	Pure Silica
Geometry		
Core diameter (μm)	10 ± 0.5	50 ± 1
Clad diameter (μm)	125 ± 2	125 ± 1
Coating Diameter (μm)	155 ± 2	155 ± 1
Measurement Metrics		
Range (km)	16	15
Operating Temperature	-40 to 200	< 175
Spatial Resolution (m)	1.5	1.2
Sampling Interval (m)	0.77	0.5
Recording Length (s)	10	12

Table 5. The attenuation in dB/km for the total length as well as the bottom half of the downhole multimode (MM) fiber at 850 nm and 1300 nm.

	850 nm		1300 nm	
Date	Total length (0-5025 ft)	Bottom Half (2512-5025 ft)	Total length (0-5025 ft)	Bottom Half (2512-5025 ft)
	Attenuation (dB/km)		Attenuation (dB/km)	
6/14/2019	3.48	2.474	1.874	0.475
1/28/2022	4.02	3.602	2.079	1.451
2/14/2022	4.906	4.908	3.139	2.778

Table 6. Attenuation readings from multi-wavelength OTDR for the total length and bottom half of the MM fiber taken in Jun 2022.

	Total length (0-5025 ft)	Bottom Half (2512-5025 ft)
Wavelength (nm)	Attenuation (dB/km)	
1244	2.037	2.68
1310	1.862	2.559
1383	1.945	2.659
1550	1.538	2.222
1625	1.439	2.096

Table 7. Oil-mud mud properties.

Mixture Properties	Unit	Values
Measured Mud Weight	sg	1.013
Plastic viscosity	cp	16
Yield Point	lb. /100ft ²	16
Oil/Water Ratio	%/%	70/30
LGS	% By vol	2.6
HGS	% By vol	9.7
Brine		
Brine SG	sg	1.025
Water Concentration	bbl.	0.272
Salt Concentration	lb. /bbl.	2.384

5.3.1.2. Single-mode Fiber Analysis

Time-lapse OTDR measurements were also acquired for the single-mode fiber that is used for DAS. Figure 46 shows the optical loss profiles repeated at different times between the initial fiber installation in 2019 and 2022 obtained at the probing wavelength of 1310 nm (Figure 46a) and 1550 nm (Figure 46b). The results show clear degradation beyond 1500 ft from the top of the single-mode fiber for both wavelengths, which appears to be worsening over time. The spike in attenuation at the bottom of the fiber (around 5025 ft) is due to the fiber termination and Fresnel reflection. Table 8 shows the attenuation values from the repeated OTDR measurements obtained at 1310 nm and 1550nm. Compared to the multimode fiber, the attenuation seen in the single-mode fiber are higher.

To further understand the cause of the increased optical attenuation, OTDR measurements were acquired at additional wavelengths. Figure 47 shows the profiles for the multi-wavelength OTDR obtained in Jun 2022, and the optical loss results are summarized in Table 9. An increase in optical loss is observed below 3000 ft for all wavelengths. Like the multimode fiber, neither hydrogen darkening nor macrobending seems to be culprits here since a significant increase in losses is not observed at 1244 nm, 1310 nm, 1383 nm, or 1625 nm, as would be expected for those mechanisms. As shown in Figure 40, the single-mode fiber also has carbon and polyimide coatings which are hermetic and will be resistant to hydrogen darkening, especially at temperatures below 170 °C. The maximum temperature that the fibers have been exposed to in the test well is less than 130 °F, so it is expected that the coatings should still be effective even if they are in an environment with hydrogen, which we do not expect in our case. Like the multimode fiber case, no significant change in OTDR profiles was observed after the change in wellbore fluid from water to OBM in February

2022, which rules out degradation due to fluid ingress in the DFOS control line from pin holes or poor termination at the bottom.

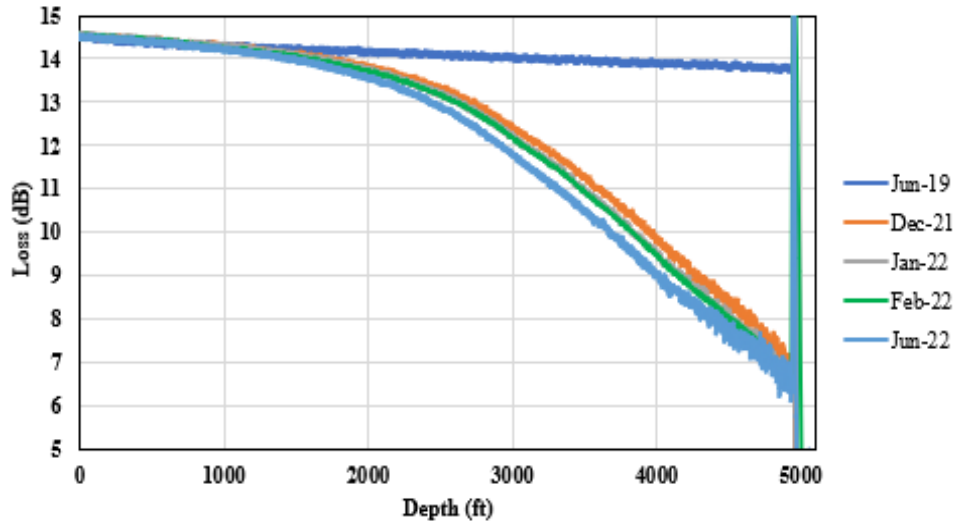
Table 8. The attenuation in dB/km for the total length as well as the bottom half of the downhole single mode fiber at 1310 nm and 1550 nm OTDR.

	1310 nm		1550 nm	
	Total length (0-5025 ft)	Bottom Half (2512-5025 ft)	Total length (0-5025 ft)	Bottom Half (2512-5025 ft)
	Attenuation (dB/km)		Attenuation (dB/km)	
6/14/2019	0.577	0.4	0.712	0.313
12/2/2021	5.013	8.6	4.431	7.563
1/28/2022	5.065	8.276	4.621	7.669
2/14/2022	5.169	8.423	4.632	7.786
6/20/2022	5.197	8.531	4.633	7.881

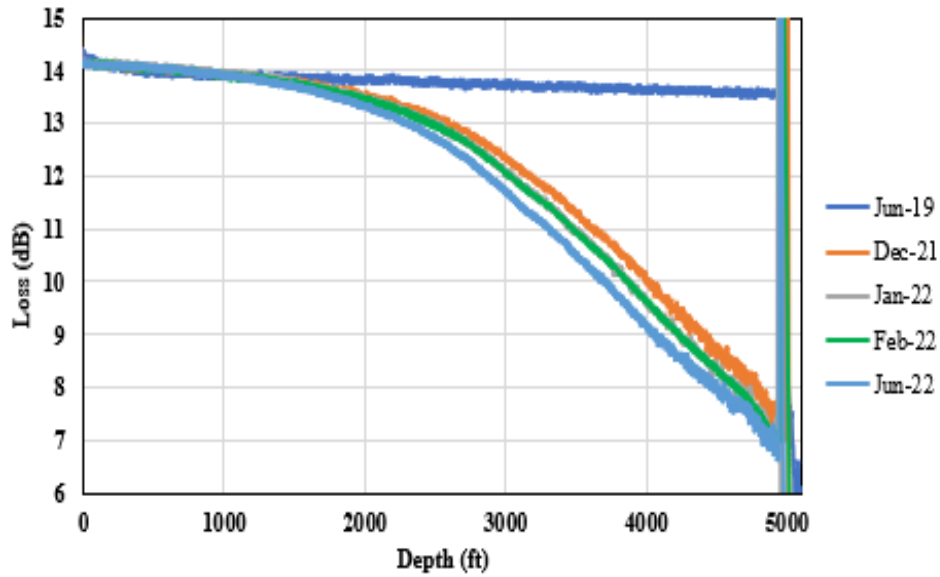
Table 9. Multi-wavelength optical attenuation readings for the total length and bottom half of the single-mode fiber acquired in Jun 2022.

Wavelength (nm)	Dec-21		Jun-22	
	Total length (0-5025 ft)	Bottom Half (2512-5025 ft)	Total length (0-5025 ft)	Bottom Half (2512-5025 ft)
	Attenuation (dB/km)		Attenuation (dB/km)	
1244	-	-	5.515	8.749
1310	5.013	8.25	5.197	8.331
1383	4.901	8.126	5.147	8.247
1550	4.431	7.463	4.633	7.481
1625	4.447	7.438	4.539	7.459

Since there are no splices or optical connectors across the fiber installed in the tubing, this leaves microbending as the only viable cause for the degradation.



(a)



(b)

Figure 46. Periodic OTDR measurements at (a) 1310 nm and (b) 1550 nm.

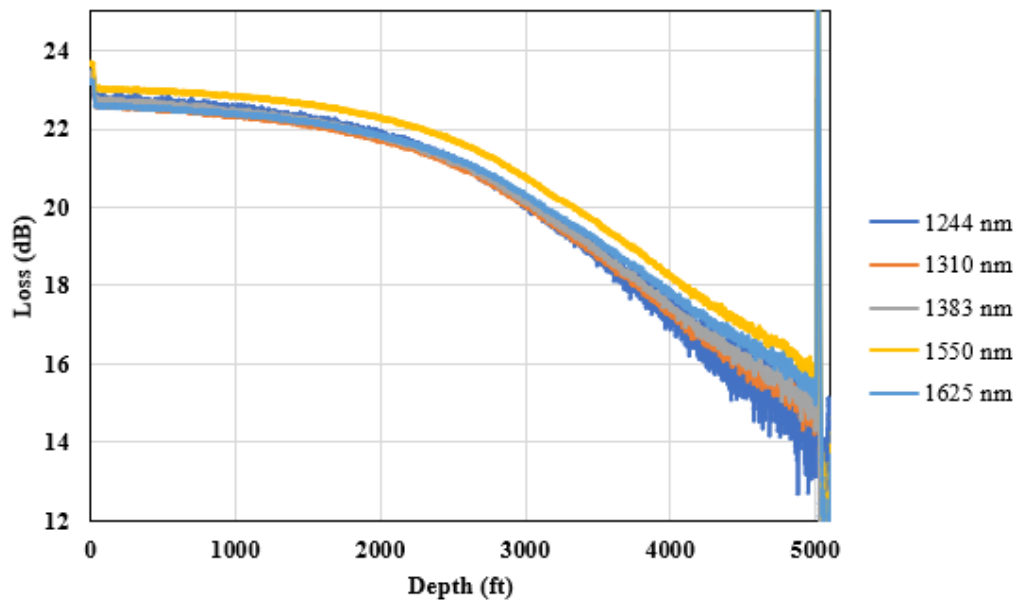
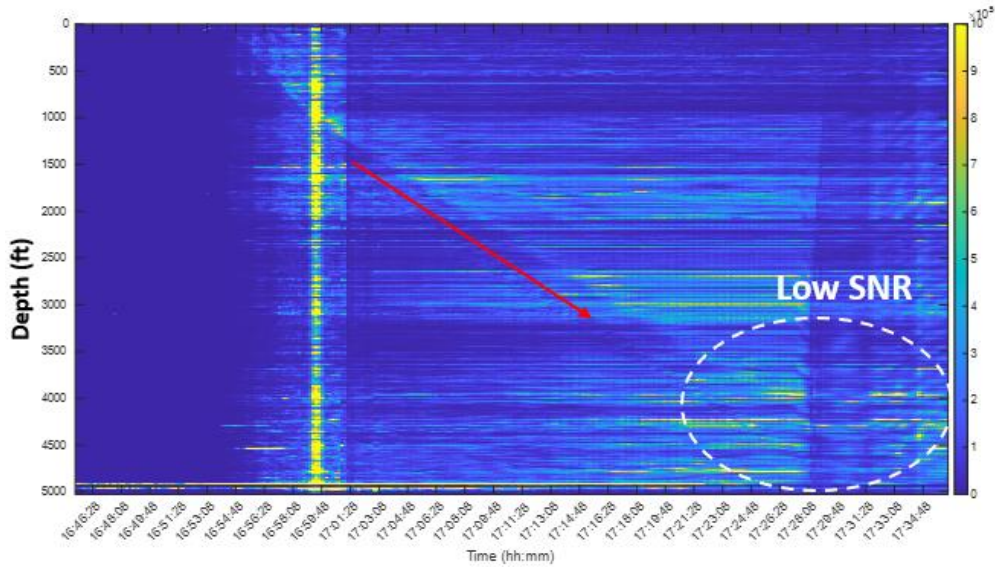
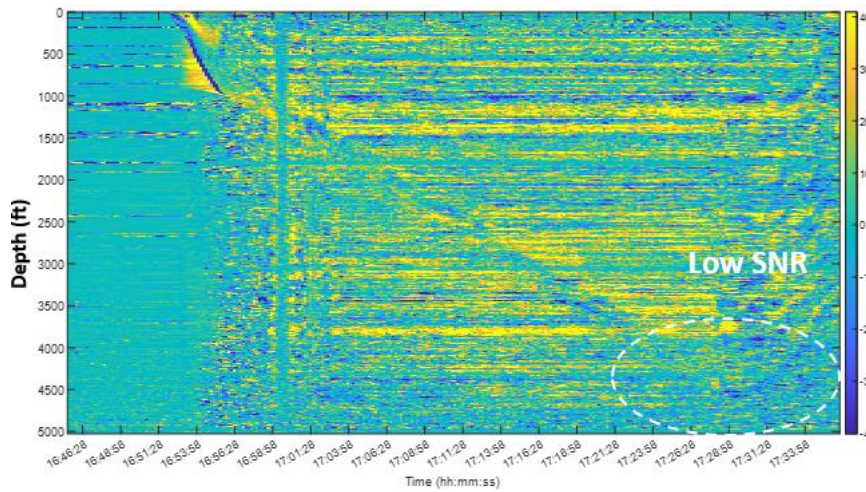


Figure 47. Multi-wavelength OTDR for the single-mode fiber acquired in Jun 2022.

Microbending in the single-mode and multimode fibers in the test well can result from the degradation of the fiber coating due to the mechanical stress caused by the roughness of the control line's inner wall and/or IPA damage solvent damage of the coating material. As can be seen from equation (2), several parameters can affect microbending. Smaller core size and large refractive index differences can contribute to reducing microbending attenuation. But these are usually standardized because they affect other optical parameters as well. The coating diameter, however, can be a major design parameter implicit in the "b" parameter in equation 2. Increasing the coating diameter increases the stiffness of the coated fiber hence also reducing the tendency for microbending. The coating diameter can be seen as a low-pass filter of small radius external perturbations. Jay [72] showed that as the coating diameter increased, the microbending sensitivity reduced with coated fiber diameter. The worst performer was the fiber with a core diameter of $\sim 250 \mu\text{m}$. The overall fiber diameter for both the multimode and single-mode fibers is $\sim 155 \mu\text{m}$. Hence there is a higher tendency that they would have high microbending sensitivity.



(a)



(b)

Figure 48. The effect of single-mode fiber degradation on DAS data for gas injection in the tubing shows low SNR at the bottom in: (a) high-frequency DAS FBE (b) low-frequency DAS FBE.

Another potential cause of microbending would be a differential expansion of the fiber and the surrounding material [81], which can be accelerated due to thermal cycling. If the fiber gets cold, it will shrink and get shorter. If the core/cladding is not shrinking at the same rate, then there could be a possibility of microbending. Thermal expansion and contraction cycling could cause the ¼” capillary tube (control line) hosting the optical fibers to stretch the fiber effectively stealing excess fiber length from the upper portions of the well. Then, as the well cools, the surplus loose fiber in

the lower length will buckle (bunch) as the cooler ¼” tube shrinks as it recovers to the geothermal background temperature. However, the DFOS in the test well has a loose-tube construction which implies that the internal diameter of the outer capillary tube is much greater than the outside diameter of the single-mode and multimode fibers inside it. This arrangement allows the outer capillary tube or control line to respond to changes in temperature without stressing the fibers. Moreover, polyimide has very low thermal conductivity making the transfer of heat very slow. Based on this, the chance that temperature cyclicity could be the reason for the microbending is probably low. The multimode and single-mode fibers in the test well were pumped with 99.9% IPA and then purged over 48 hours with nitrogen. The source of the reduction in the already thin coating diameter could be due to the damage of the polyimide coating if it encountered IPA during installation. Polyimide is a polymer containing the imide group belonging to a class of high-performance plastics. However, not all polyimides perform the same as the actual materials, and the manner of coating may be different [71]. Oulundsen et al. also mentioned that poorly optimized polyimide coating could develop blisters under even relatively low temperatures, such as (50 °C), which could potentially occur in this case.

The impact of degradation in the single-mode fiber on the DAS data can be seen in Figure 48. Figure 48a shows the high frequency (2-5000 Hz) DAS Frequency Band Energy (FBE) plot during nitrogen gas injection into the 2-7/8-inch tubing. Figure 48b shows the corresponding low-frequency DAS FBE (0-2 Hz). We can see from both figures that the line that tracks the gas movement (just above the red arrow) disappears below about 3000 ft. The degradation of the fiber has caused a low signal-to-noise ratio (SNR) at the bottom and the gas signature is buried in the noise.

5.3.2. Time-Lapse Raman Spectra Analysis

The time-lapse NTS and TTS Raman backscatter profiles were analyzed to further understand the optical losses observed in the multimode fiber. Figure 49 shows the NTS profiles at four different periods between December 2020 and February 2022, while Figure 50 shows the corresponding TTS profiles for the same periods. The NTS mainly contains the fiber loss information as captured from the Raman Stokes spectrum, while the TTS contains both the temperature and the loss information as captured from the Raman anti-Stokes spectrum. From the NTS and TTS profiles, we can see that, like the OTDR profiles, the top section of the fiber is not showing significant change (as the profiles mostly overlay). However, the rate of degradation increases progressively towards the bottom half of the fiber, which is consistent with the observations from the OTDR measurements.

To evaluate the impact of the multimode fiber degradation on the measured temperature values, we compare the DTS temperature profiles with the temperatures obtained from the downhole gauges that were installed at four depths along the wellbore. Figure 51 shows the DTS values and gauge temperatures recorded from June 2020 to June 2022. The red profile shows the difference between the DTS and the gauge temperatures. The mean differential temperatures are 0.1 °F, 0.4 °F, 5.4 °F, and 9.8 °F at 487 ft, 2023 ft, 3502 ft, and 5024 ft, respectively. This further confirms what we have observed in the OTDR profiles in which the losses increase towards the bottom of the fiber. A careful look at the differential temperature profiles at the bottom two gauge depths also shows the difference in the temperature is increasing with time. The trend of the temperature differential can be employed to correct the DTS temperature at the gauge depths.

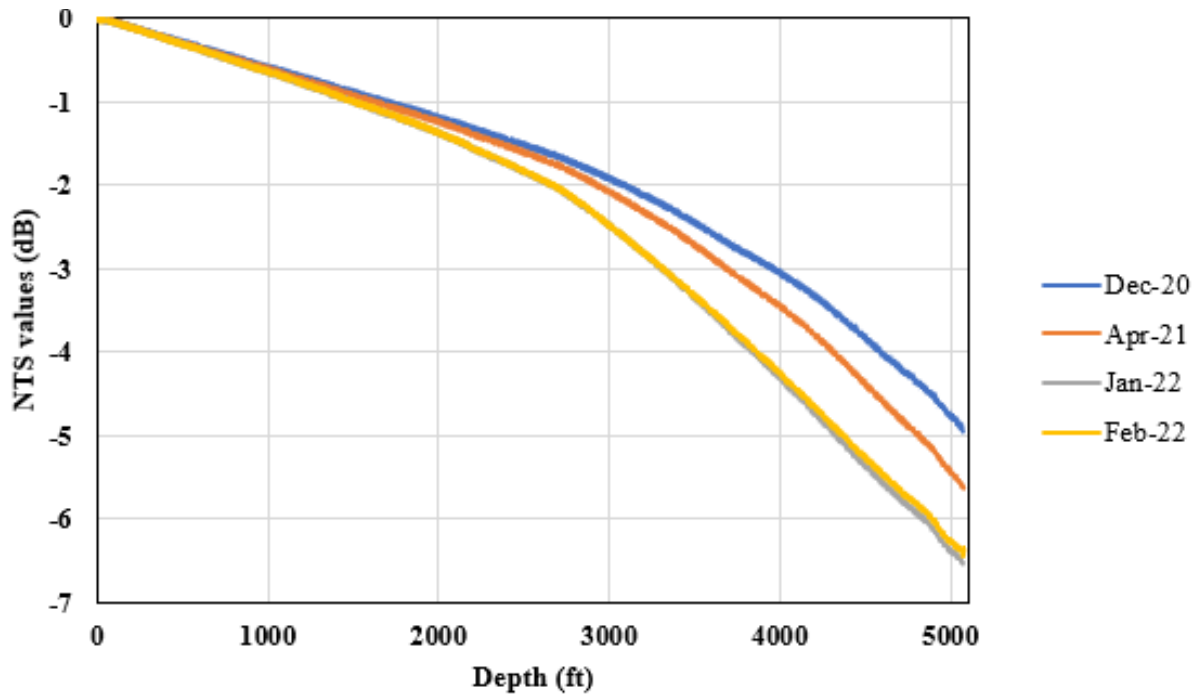


Figure 49. Time-lapse plot of NTS from the multimode fiber.

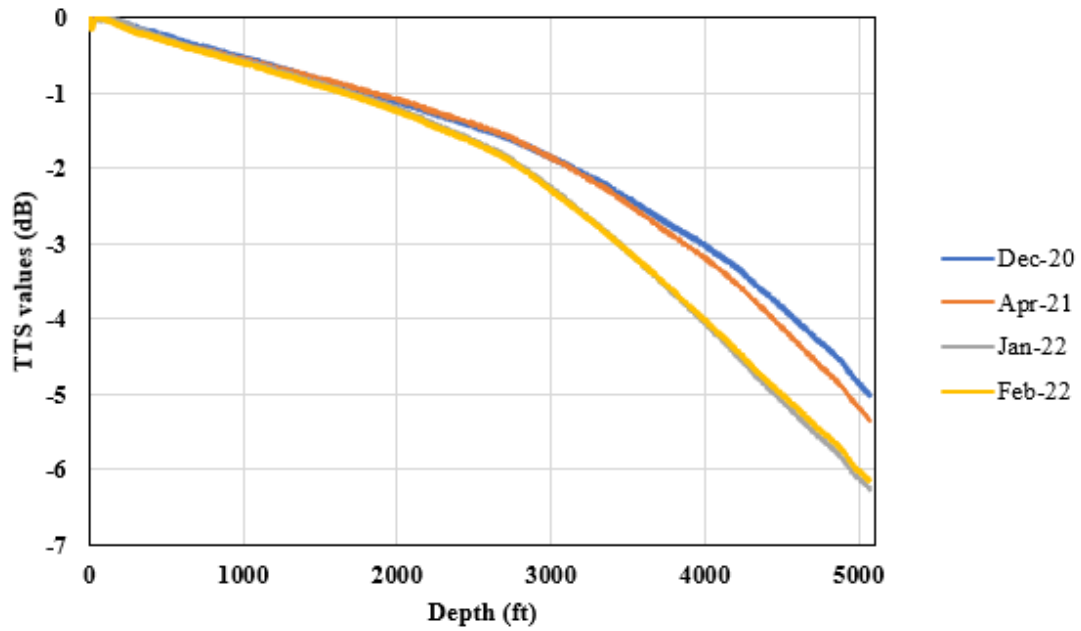


Figure 50. Time-lapse plot of TTS from the multimode fiber.

5.4. Signal-to-Noise (SNR) Estimation

A simple SNR estimation‡ approach was adopted to quantify the effect of the gas kick volume and migration on the SNR of DAS measurements. Since the objective was to estimate gas rise velocity, the “signal” of interest for the SNR calculation was selected as the FBE traces at different time steps during the gas rise in the annulus. This “signal” was compared against a reference DAS FBE trace (or the “noise”) which was selected about an hour after the gas had completely migrated out of the wellbore, while similar operating conditions (such as circulation rates, choke, and pump speed) were maintained. The reference “noise” FBE will naturally include the effect of all the noise sources discussed above, which are always present, in addition to the background noise caused by circulation, but not include the effect of gas which is our target “signal” for the SNR analysis. The background noise for each trial was selected about an hour after the gas had migrated out of the wellbore based on the observations from the DAS, DTS, and downhole gauges. We ensured that the selected timesteps for the background (reference “noise”) were at similar operating conditions such as circulating rates and choke position to the timesteps selected for the “signal” traces (gas presence). To estimate the SNR, the FBE values for the “signal” traces were divided by the FBE values for the background “noise” trace and then a moving window averaging filter was applied to reduce the spikiness of the curves. DAS results from six sets of well-scale tests are presented to highlight the effect of gas kick volumes (from 2 bbl. to 15 bbl.), circulation rates (from 0 to 100

‡ Section 6.4 was previously published as some sections in J Sharma, OL Santos, O Ogunsanwo, GK Ekechukwu, T Cuny, M Almeida, Y. Chen "Fiber-Optic DAS and DTS for monitoring riser gas migration" in *Journal of Petroleum Science and Engineering*, 2023. Volume 220, Part B, 111157, <https://doi.org/10.1016/j.petrol.2022.111157>.

GPM) and injection method (either through the chemical line or the tubing) on gas rise dynamics in a wellbore. The experimental parameters are summarized in Table 10.

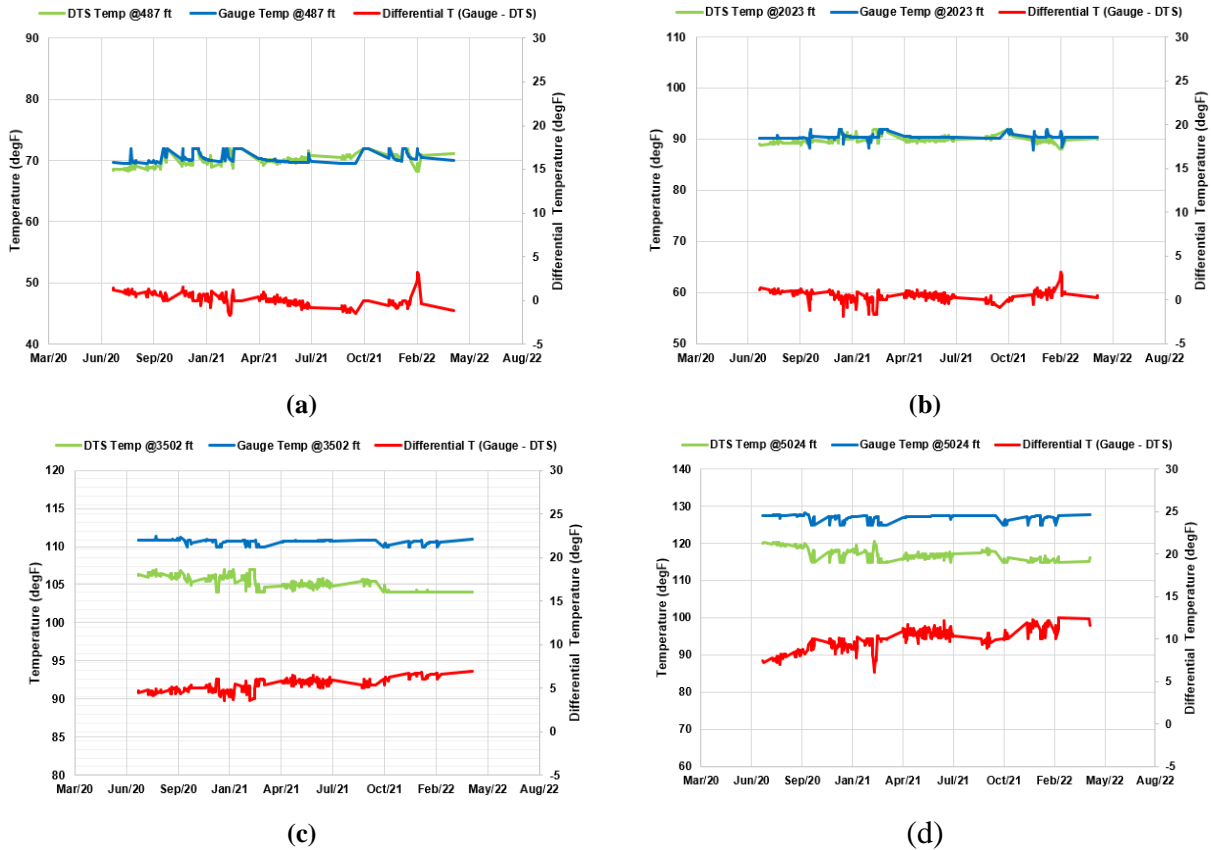


Figure 51. DTS and gauge temperature readings over time at four different depths at (a) 487 ft (b) 2023 ft (c) 3502 ft and (d) 5024 ft.

The FBE Band 0 (2–5,000 Hz) plot of the six trials is shown in Figure 52 below. The signal-to-noise ratios (SNR) of the DAS data for the six experiments are also compared to understand the effect of operational parameters, fiber degradation, and optical noise on DAS sensitivity. The SNR results are presented in Figure 53 for three representative timesteps, which demonstrate the rising gas in the wellbore over time evident from the spike in the SNR versus depth curves. In all trials, the SNR reduces over time as the gas gets closer to the surface (third timestep) and higher at the

deeper depth intervals (first and second timesteps) due to the dispersion of the gas phase because of lower pressure and gas expansion as it travels upwards in the annulus.

Table 10. Flow parameters for experimental runs used in this section.

Trial nomenclature	A1	A2	A3	A4	A5	A6
Circulation rate (GPM)	100	100	0	0	0	0
Gas kick volume (bbl.)	10.1	2	10	2	15.1	5
Injection method	Line	Line	Line	Line	Tubing	Tubing

The SNR observed in the static water column is much higher (trials A3 and A4) as compared to the trials with water circulation (A1 and A2) which increases the background acoustic noise resulting from the flowing water. The results show that the SNR is not significantly affected by the injected gas volume. For instance, the SNR over time for trials A1 (10 bbl. kick) and A2 (2 bbl. kick) are comparable. The SNR results provide another means to detect gas in the presence of another wellbore fluid and demonstrate that our ability to monitor gas kick is affected by the location of the gas influx along the wellbore as well as the wellbore circulation rates.

SNR was also estimated for the trials injected through the tubing (A5 and A6) using a similar methodology as the first four trials (A1-A4). For trials, A5 and A6, the gas rise signature was evident in the SNR versus depth curves over time, which showed higher SNR at deeper intervals in the wellbore and lower SNR as the gas traveled upward and got increasingly dispersed. The results demonstrate that the SNR and our ability to detect gas are also affected by the method of delivery in other words, whether the gas enters the annulus through a small opening (as simulated by the injection line) or a larger formation section (as simulated by the injection through the tubing).

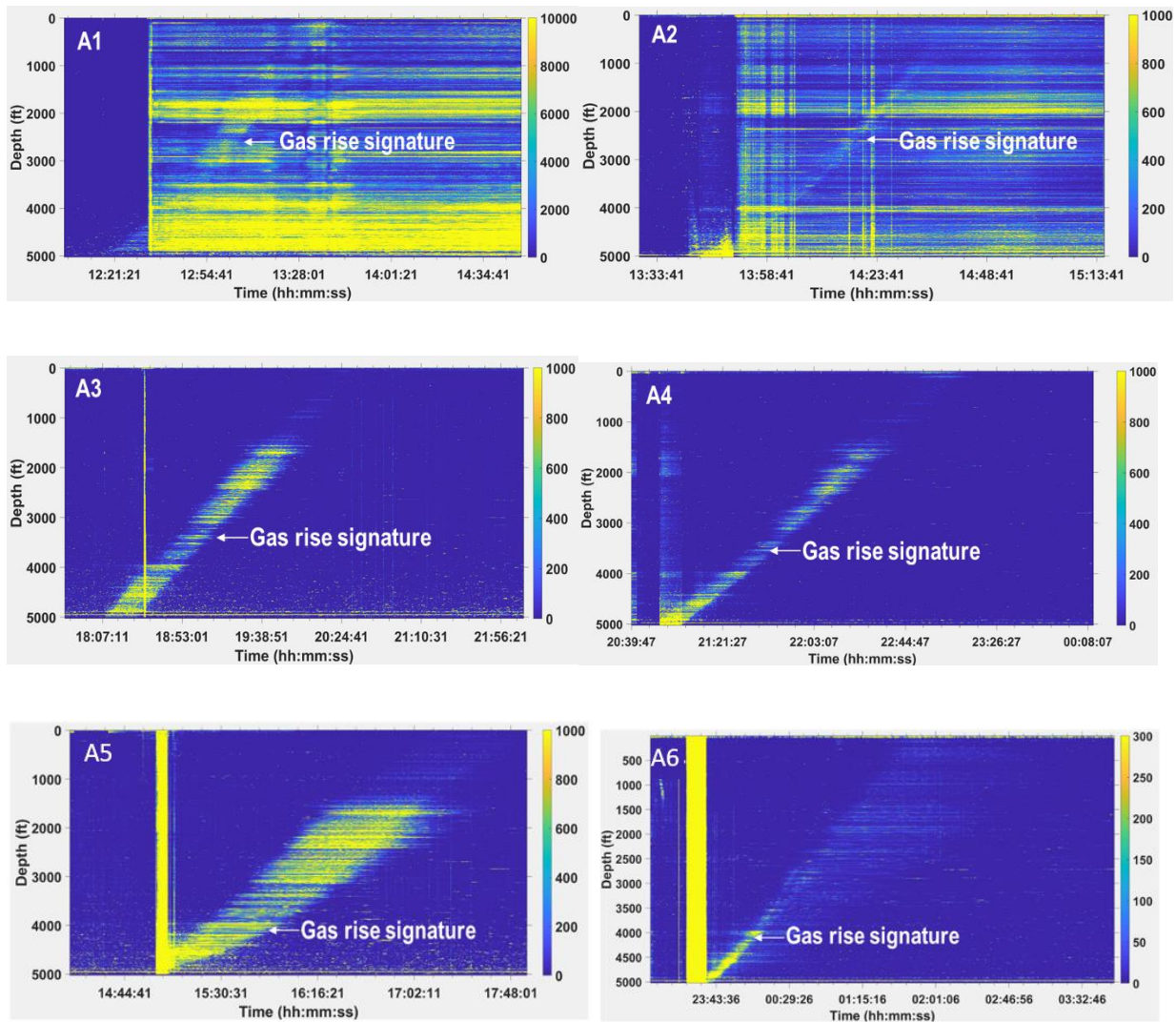


Figure 52. DAS Band 0 (2–5000 Hz) FBE waterfall plots for trials A1 to A6.

5.5. Summary

This study presents a detailed analysis to understand the root cause of the fiber degradation observed in the single- and multi-mode fibers installed in a 5125-ft-deep test well. Optical losses and resulting degradation were measured using multi-wavelength, periodic OTDR analysis. Additionally, the time-lapsed Raman backscatter was evaluated to further understand the degradation in the multimode fiber. The analysis showed that the degradation was likely not caused

due to hydrogen darkening, fluid ingress, or macrobending. The evidence pointed to microbending as the main cause of degradation.

Based on the assessment of degradation observed in the single-mode and multimode fibers in the test well, the following protocols are recommended for any of our future installations:

- Make use of gel-filled fiber cable of suitable coating diameter. The gels should be waterproof and thixotropic so that they can cover up even tiny spaces.
- Tight-buffered fiber-optics cable should also be considered, and the use of IPA can be avoided.
- The coated fiber cable needs to be tested for microbending and chemical resistance before deployment downhole.
- Frequent OTDR after deployment.
- Minimize end of fiber Fresnel reflection by proper termination.
- Double-ended configuration can also be considered.

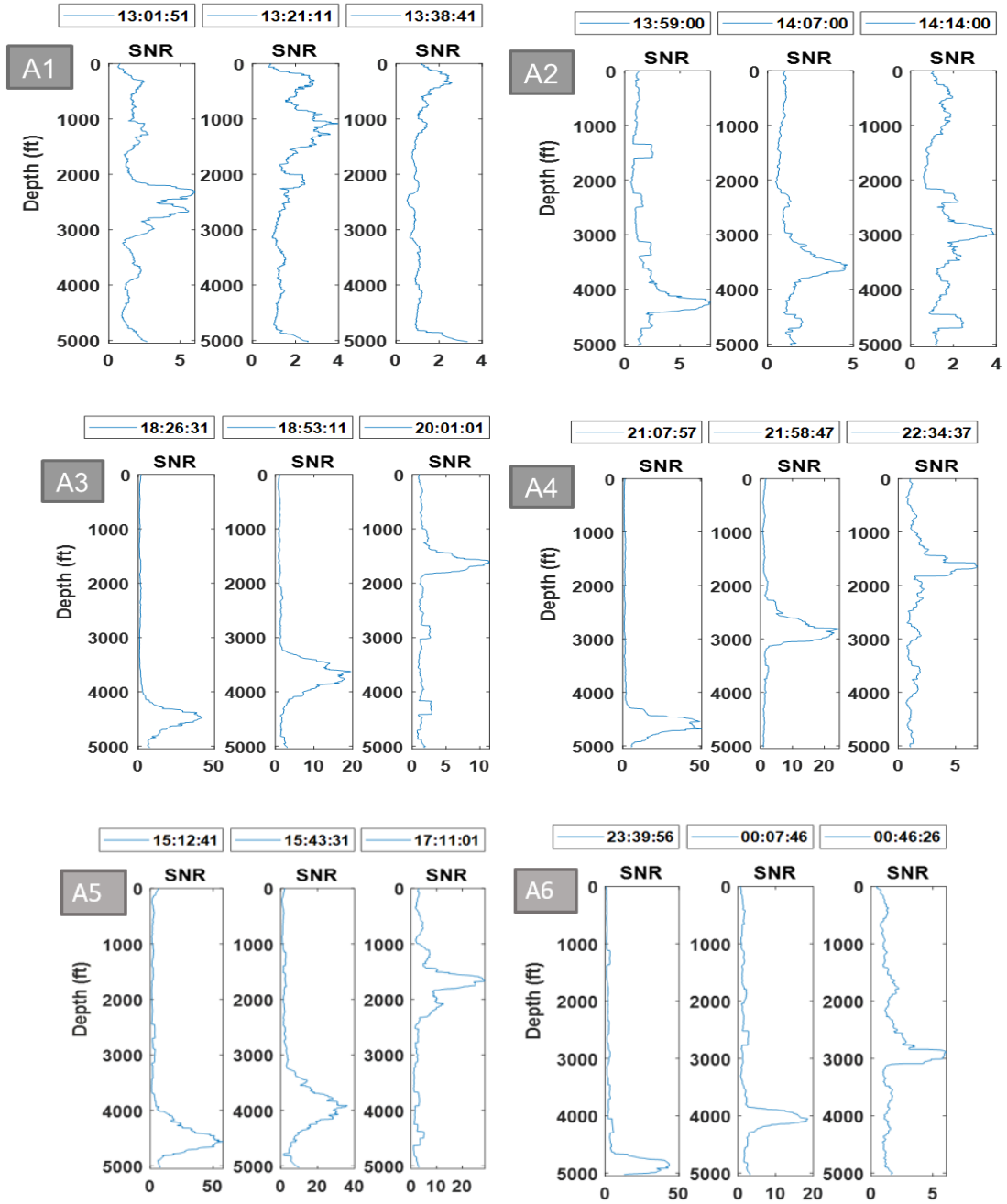


Figure 53. SNR plots for DAS FBE (Band 0) for trials A1 to A6.

Chapter 6. Conclusions and Recommendations for Future Work

6.1. Summary

In this research, a range of novel workflows are presented that include signal processing, time- and frequency-domain filtering, and machine learning methodologies that can be implemented on DAS and DTS datasets for a range of applications. In Chapter 2, a combination of machine learning and signal processing workflow was developed to measure distributed pressure across wellbore using DAS and DTS data. The workflow was successfully demonstrated for pressure estimation in two experimental datasets, corresponding to different gas injection volumes, backpressure, injection methods, and water circulation rates. The workflow utilizes the random forest algorithm and involves a two-step process for distributed pressure prediction. In the first step, single-depth predictive modeling is performed to explore the underlying relationship between the DAS (in seven different frequency bands), DTS, and the gauge pressures at the four downhole locations. The single-depth analysis showed that the low-frequency components (< 2 Hz) of the DAS data, when combined with DTS, consistently demonstrate a superior capability in predicting pressure as compared to the higher frequency bands for both the datasets achieving an average coefficient of determination (or R^2) of 0.96. This can be explained by the unique characteristic of low-frequency DAS, which is sensitive to both strain and temperature perturbations. In the second step, the DTS and the low-frequency DAS data from two gauge locations were used to predict pressures at different depths. The distributed pressure modeling achieved an average R^2 of 0.95, and an average root mean squared error (RMSE) of 24 psi for the two datasets across the depths analyzed, demonstrating the distributed pressure measurement capability using the proposed workflow. Most of the current DAS applications rely on higher frequency components. This study presents a novel

application of the low-frequency DAS combined with DTS for distributed pressure measurement on a well-scale.

In Chapter 3, a unique workflow that utilizes signal processing techniques such as the Hough Transform and f-k transform is proposed to identify gas-kick and estimate gas influx velocity using real-time downhole data from an optical fiber-based DAS deployed in a wellbore. Popular gas-kick monitoring techniques such as pit gains, increases in flow rate from a well at constant pump speed, and pumps-off flow from the well are surface indicators that suffer from time delay in detecting conditions between the surface and the downhole. These surface-based approaches may also have inadequate accuracy when dealing with small overflows. The Hough transform, which is a feature extraction approach for grouping edge points into object candidates via a vote operation across a set of parameterized picture objects, is employed in the workflow. The Hough transform is applied to frequency-wavenumber (f-k) graphs to estimate the gas influx velocity in real time, as discussed in the next section. In this study, an automatic technique to detect the real-time influx of gas into a well-bore is presented. This method is an improvement over the current techniques in which the gas velocity is detected mostly by surface-based techniques that suffer from time delay in the monitoring between the surface and the wellbore or by manual calculations from the F-K plot.

In Chapter 4, a combination of time- and frequency-domain filtering techniques are presented that comprise the VBE workflow to identify the gas-fluid interface and the SOS in DAS vibration data to estimate gas void fraction are presented. The workflow involves a sequential application of several signal processing techniques (including gradient computation, f-k filtering, automatic gain control, phase velocity filtering, autocorrelation, stacking, and RMS computation) on DAS vibration data. The outputs from the VBE workflow are used as inputs into two

independent techniques to estimate the gas-water mixture length and gas void fraction or liquid holdup. The first method is the use of combined pressure-difference and DFOS data to estimate gas fraction. The second method uses the speed of sound (SOS) method for determining the gas fraction in the wellbore. The findings of our research will be beneficial to improve and validate fiber-optics-based production logging algorithms, detection, and quantification of gas leak volumes in the wellbore, as well as pipeline flow monitoring.

In Chapter 5, a root-cause analysis was performed to understand the main cause of observed degradation in both the single mode and multimode fibers installed in our test well as well as to study the impact of the degradation on the DAS and DTS data quality over time, both qualitatively and quantitatively. A concise summary of the potential cause of fiber degradation was first presented. Multi-wavelength OTDR measurements were employed to identify the most likely culprit causing the fiber degradation in both single-mode and multi-mode fibers in our well. In addition, Raman Spectral analysis was conducted to further analyze the degradation in the multimode fiber. The analysis showed that the degradation was likely not caused due to hydrogen darkening, fluid ingress, or macrobending. All evidence pointed to microbending as the main cause of degradation. The last section of this chapter highlights a simple signal-to-noise (SNR) estimation technique used to quantify the effect of the gas kick volume and migration on the SNR of DAS measurements.

6.2. Recommendations for Future Work

Some suggestions for future research work are highlighted below:

- One limitation of the current study is that the VBE workflow for gas tracking does not perform well with high noise. This could be due to the fiber degradation observed at the bottom of the well. The true capability of the workflow needs to be reevaluated once the

DFOS cables are replaced with probably a tight-buffered fiber, which could reduce the non-uniform coupling of the pumped fiber.

- Machine learning can also be explored for gas-liquid interface tracking. The model can be trained on the previously labeled DAS data with the presence of gas. The trained model can then be used to predict the gas-liquid interface in a test dataset.
- The results of the gas fractions obtained in this study can also be compared with results obtained using other techniques, such as numerical simulation.
- Additional datasets can be utilized for further validation of the proposed gas detection workflow presented in Chapter 2 as we were only able to demonstrate it on a single data set.
- An investigation of the impact of mud properties on the DAS measurements can also be performed. Actual drilling is done with drilling muds that can be either water-based or oil-based. These muds have solid particles that may cause more vibration that could affect the DAS response and the SNR in a different way.
- The methodologies proposed in this research can be tested in producing or injecting well scenarios since the workflows in this study were primarily tested on dataset from a cased wellbore (that is not producing from a formation).
- Nitrogen gas was used in this work for the multiphase flow datasets. The solubility of nitrogen in water is quite low. It will be important to check how the proposed methodologies would perform when a highly soluble gas such as CO₂ is used in the experiments. This will become extremely important for projects that involve CO₂ plume monitoring.

Appendix. Copyright Information

A.1. Scientific Reports Journal Copyright

License agreement and author copyright

Scientific Reports does not require authors to assign copyright of their published original research papers to the journal. Articles are published under a [CC BY license](#) (Creative Commons Attribution 4.0 International License). The CC BY license allows for maximum dissemination and re-use of open access materials and is preferred by many research funding bodies. Under this license, users are free to share (copy, distribute and transmit) and remix (adapt) the contribution including for commercial purposes, providing they attribute the contribution in the manner specified by the author or licensor ([read full legal code](#)).

Visit our open research site for more information about [Creative Commons licensing](#).

<https://www.nature.com/srep/journal-policies/editorial-policies#license-agreement>

scientific reports

[Explore content](#) ▾ [About the journal](#) ▾ [Publish with us](#) ▾

[nature](#) > [scientific reports](#) > [articles](#) > article

Article | [Open Access](#) | [Published: 14 June 2021](#)

Well-scale demonstration of distributed pressure sensing using fiber-optic DAS and DTS

[Gerald K. Ekechukwu](#) & [Jyotsna Sharma](#) 

[Scientific Reports](#) **11**, Article number: 12505 (2021) | [Cite this article](#)

3359 Accesses | **10** Citations | **7** Altmetric | [Metrics](#)

A.2. Optical Publishing group Copyright Information

Request for Publication rights



Gerald K Ekechukwu
To: copyright@optica.org

Wed 11/23/2022 10:57 AM

Dear Sir/Ma

I am completing a doctoral dissertation at Louisiana State University.

I am requesting permission to use the contents of my 2021 paper titled "Automated Detection and Quantification of Gas Influx Velocity in Wellbore from Fiber-Optic Sensor Data" in my dissertation, which is in preparation for my graduation in December 2022.

Please contact me if you have any questions or need additional information.

Thank you.

Sincerely,
Gerald Ekechukwu



Optica Publishing Group Copyright <copyright@osa.org>
To: Gerald K Ekechukwu; Optica Publishing Group Copyright <copyright@osa.org>

Thu 12/1/2022 9:04 AM

You don't often get email from copyright@osa.org. [Learn why this is important](#)

Dear Gerald Ekechukwu,

Thank you for contacting Optica Publishing Group.

For the use of material from G. K. Ekechukwu and J. Sharma, "Automated Detection and Quantification of Gas Influx Velocity in Wellbore from Fiber-Optic Sensor Data," in OSA Optical Sensors and Sensing Congress 2021 (AIS, FTS, HISE, SENSORS, ES), S. Buckley, F. Vanier, S. Shi, K. Walker, I. Coddington, S. Paine, K. Lok Chan, W. Moses, S. Qian, P. Pellegrino, F. Vollmer, G. , J. Jágerská, R. Menzies, L. Emmenegger, and J. Westberg, eds., OSA Technical Digest (Optica Publishing Group, 2021), paper JTh6A.11:

Optica Publishing Group only has copyright for the compilation of the conference proceedings, not the individual papers themselves. As the authors retain copyright to the individual paper, an credit statement is not needed, although we do request a complete citation be included in any publication or adjacent to any posting.

Please let me know if you have any questions.

Kind Regards,
Hannah Greenwood

Hannah Greenwood
December 1, 2022
Authorized Agent, Optica Publishing Group

OPTICA
PUBLISHING GROUP | Formerly
OSA

A.3. Journal of Petroleum Science and Engineering Copyright Information



Fiber-Optic DAS and DTS for monitoring riser gas migration

Author: Jyotsna Sharma, Otto Santos, O. Ogunsanwo, Gerald K. Ekechukwu, T. Cuny, M. Almeida, Y. Chen

Publication: Journal of Petroleum Science and Engineering

Publisher: Elsevier

Date: January 2023

© 2022 Elsevier B.V. All rights reserved.

Journal Author Rights

Please note that, as the author of this Elsevier article, you retain the right to include it in a thesis or dissertation, provided it is not published commercially. Permission is not required, but please ensure that you reference the journal as the original source. For more information on this and on your other retained rights, please visit: <https://www.elsevier.com/about/our-business/policies/copyright#Author-rights>

References

- [1] H. Guo, G. Xiao, N. Mrad, and J. Yao, "Fiber Optic Sensors for Structural Health Monitoring of Air Platforms," *Sensors*, vol. 11, no. 4, pp. 3687–3705, Mar. 2011, doi: 10.3390/s110403687.
- [2] K. Soga and L. Luo, "Distributed fiber optics sensors for civil engineering infrastructure sensing," *J. Struct. Integr. Maint.*, vol. 3, no. 1, pp. 1–21, Jan. 2018, doi: 10.1080/24705314.2018.1426138.
- [3] T. Yoshino, K. Kurosawa, K. Itoh, and T. Ose, "Fiber-Optic Fabry-Perot Interferometer and its Sensor Applications," *IEEE Trans. Microw. Theory Tech.*, vol. 30, no. 10, pp. 1612–1621, Oct. 1982, doi: 10.1109/TMTT.1982.1131298.
- [4] D. Inaudi, "Combined static and dynamic monitoring of civil structures with long-gauge fiber optic sensor," in *IMAC XXIII Conference and Exposition on Structural Dynamics, Orlando, 2005*, p. 3.
- [5] O. Othonos, A. Kalli, *Fiber Bragg Gratings: fundamentals and applications in telecommunications and sensing*. Norwood, 1999.
- [6] A. Hartog, *An Introduction to Distributed Optical Fibre Sensors*. CRC Press Taylor & Francis Group, 2017.
- [7] D. Hill, "Distributed Acoustic Sensing (DAS): Theory and Applications," in *Frontiers in Optics 2015*, 2015, p. FTh4E.1, doi: 10.1364/FIO.2015.FTh4E.1.
- [8] L. B. Liokumovich, N. A. Ushakov, O. I. Kotov, M. A. Bisyarin, and A. H. Hartog, "Fundamentals of Optical Fiber Sensing Schemes Based on Coherent Optical Time Domain Reflectometry: Signal Model Under Static Fiber Conditions," *J. Light. Technol.*, vol. 33, no. 17, pp. 3660–3671, Sep. 2015, doi: 10.1109/JLT.2015.2449085.
- [9] K. Miah and D. Potter, "A Review of Hybrid Fiber-Optic Distributed Simultaneous Vibration and Temperature Sensing Technology and Its Geophysical Applications," *Sensors*, vol. 17, no. 11, p. 2511, Nov. 2017, doi: 10.3390/s17112511.
- [10] D. Gloge, "Weakly Guiding Fibers," *Appl. Opt.*, vol. 10, no. 10, p. 2252, Oct. 1971, doi: 10.1364/AO.10.002252.
- [11] R. Oshana, "Overview of Digital Signal Processing Algorithms," in *DSP Software Development Techniques for Embedded and Real-Time Systems*, Elsevier, 2006, pp. 59–

121.

- [12] J. Sharma, T. Cuny, O. Ogunsanwo, and O. Santos, “Low-Frequency Distributed Acoustic Sensing for Early Gas Detection in a Wellbore,” *IEEE Sens. J.*, pp. 1–1, 2020, doi: 10.1109/JSEN.2020.3038738.
- [13] A. J. Rogers, S. V. Shatalin, and S. E. Kanellopoulos, “Distributed measurement of fluid pressure via optical-fibre backscatter polarimetry,” May 2005, p. 230, doi: 10.1117/12.623804.
- [14] A. J. Rogers, “Distributed optical-fibre sensors for the measurement of pressure, strain and temperature,” *J. Inst. Electron. Radio Eng.*, vol. 58, no. 5S, p. S113, 1988, doi: 10.1049/jiere.1988.0048.
- [15] C. S. Baldwin, “Brief history of fiber optic sensing in the oil field industry,” Jun. 2014, p. 909803, doi: 10.1117/12.2050550.
- [16] M. M. Molenaar, D. Hill, P. Webster, E. Fidan, and B. Birch, “First Downhole Application of Distributed Acoustic Sensing for Hydraulic-Fracturing Monitoring and Diagnostics,” *SPE Drill. Complet.*, vol. 27, no. 01, pp. 32–38, Mar. 2012, doi: 10.2118/140561-PA.
- [17] K. Johannessen, B. K. Drakeley, and M. Farhadiroushan, “Distributed Acoustic Sensing - A New Way of Listening to Your Well/Reservoir,” Apr. 2012, doi: 10.2118/149602-MS.
- [18] A. Chaudhuri, C. F. Osterhoudt, and D. N. Sinha, “An Algorithm for Determining Volume Fractions in Two-Phase Liquid Flows by Measuring Sound Speed,” *J. Fluids Eng.*, vol. 134, no. 10, Oct. 2012, doi: 10.1115/1.4007265.
- [19] R. Paleja *et al.*, “Velocity Tracking for Flow Monitoring and Production Profiling Using Distributed Acoustic Sensing,” Sep. 2015, doi: 10.2118/174823-MS.
- [20] J. Xiao *et al.*, “Dynamic Water Injection Profiling in Intelligent Wells Using Distributed Acoustic Sensor with Multimode Optical Fibers,” Sep. 2015, doi: 10.2118/174865-MS.
- [21] S. K. Bakku, M. Fehler, and P. Wills, “Monitoring hydraulic fracturing using distributed acoustic sensing in a treatment well,” in *SEG Technical Program Expanded Abstracts 2014*, Aug. 2014, pp. 5003–5008, doi: 10.1190/segam2014-1280.1.
- [22] D. Denney, “Distributed Acoustic Sensing for Hydraulic- Fracturing Monitoring and Diagnostics,” *J. Pet. Technol.*, vol. 64, no. 03, pp. 68–74, Mar. 2012, doi: 10.2118/0312-0068-JPT.

- [23] W. F. P. MacPhail, B. Lisoway, and K. Banks, “Fiber Optic Distributed Acoustic Sensing of Multiple Fractures in a Horizontal Well,” Apr. 2012, doi: 10.2118/152422-MS.
- [24] R. Martinez, A. D. Hill, and D. Zhu, “Diagnosis of Fracture Flow Conditions With Acoustic Sensing,” Feb. 2014, doi: 10.2118/168601-MS.
- [25] M. M. Molenaar and B. E. Cox, “Field Cases of Hydraulic Fracture Stimulation Diagnostics Using Fiber Optic Distributed Acoustic Sensing (DAS) Measurements and Analyses,” Jan. 2013, doi: 10.2118/164030-MS.
- [26] I. Nizkous, S. Gerritsen, D. Kiyashchenko, and D. Joinson, “Distributed Acoustic Sensing (DAS) VSP for Imaging and Velocity Model Building,” Dec. 2015, doi: 10.2523/IPTC-18483-MS.
- [27] G. A. Ugueto *et al.*, “Application of Integrated Advanced Diagnostics and Modeling To Improve Hydraulic Fracture Stimulation Analysis and Optimization,” Feb. 2014, doi: 10.2118/168603-MS.
- [28] P. Webster, J. Wall, C. Perkins, and M. Molenaar, “Micro-seismic detection using distributed acoustic sensing,” in *SEG Technical Program Expanded Abstracts 2013*, Sep. 2013, pp. 2459–2463, doi: 10.1190/segam2013-0182.1.
- [29] M. Karrenbach *et al.*, “DAS Microseismic Monitoring and Integration With Strain Measurements in Hydraulic Fracture Profiling,” 2017, doi: 10.15530/urtec-2017-2670716.
- [30] C. Allanic *et al.*, “Distributed Acoustic Sensing For ESP Understanding And Surveillance,” Oct. 2013, doi: 10.2118/167501-MS.
- [31] K. Boone, A. Ridge, R. Crickmore, and D. Onen, “Detecting Leaks in Abandoned Gas Wells with Fibre-Optic Distributed Acoustic Sensing,” Jan. 2014, doi: 10.2523/IPTC-17530-MS.
- [32] P. Thodi, M. Paulin, L. Forster, J. Burke, and G. Lanan, “Arctic Pipeline Leak Detection using Fiber Optic Cable Distributed Sensing Systems,” Feb. 2014, doi: 10.4043/24589-MS.
- [33] M. Becker, T. Coleman, C. Ciervo, M. Cole, and M. Mondanos, “Fluid pressure sensing with fiber-optic distributed acoustic sensing,” *Lead. Edge*, vol. 36, no. 12, pp. 1018–1023, Dec. 2017, doi: 10.1190/tle36121018.1.
- [34] P. In ’t Panhuis *et al.*, “Flow Monitoring and Production Profiling using DAS,” Oct. 2014, doi: 10.2118/170917-MS.

- [35] T. Giallorenzi *et al.*, “Optical fiber sensor technology,” *IEEE J. Quantum Electron.*, vol. 18, no. 4, pp. 626–665, Apr. 1982, doi: 10.1109/JQE.1982.1071566.
- [36] A. J. Rogers, “Polarisation optical time domain reflectometry,” *Electron. Lett.*, vol. 16, no. 13, p. 489, 1980, doi: 10.1049/el:19800341.
- [37] A. J. Rogers, “Polarization-optical time domain reflectometry: a technique for the measurement of field distributions,” *Appl. Opt.*, vol. 20, no. 6, p. 1060, Mar. 1981, doi: 10.1364/AO.20.001060.
- [38] B. Budiansky, D. C. Drucker, G. S. Kino, and J. R. Rice, “Pressure sensitivity of a clad optical fiber,” *Appl. Opt.*, vol. 18, no. 24, p. 4085, Dec. 1979, doi: 10.1364/AO.18.004085.
- [39] G. B. Hocker, “Fiber-optic sensing of pressure and temperature,” *Appl. Opt.*, vol. 18, no. 9, p. 1445, May 1979, doi: 10.1364/AO.18.001445.
- [40] J. A. Bucaro, H. D. Dardy, and E. F. Carome, “Fiber-optic hydrophone,” *J. Acoust. Soc. Am.*, vol. 62, no. 5, pp. 1302–1304, Nov. 1977, doi: 10.1121/1.381624.
- [41] SEAFOM, “Measuring Sensor Performance Document – 02 (SEAFOM MSP-02),” 2018.
- [42] L. Schenato, A. Pasuto, A. Galtarossa, and L. Palmieri, “An Optical Fiber Distributed Pressure Sensing Cable With Pa-Sensitivity and Enhanced Spatial Resolution,” *IEEE Sens. J.*, vol. 20, no. 11, pp. 5900–5908, Jun. 2020, doi: 10.1109/JSEN.2020.2972057.
- [43] H. H. Evinger and M. Muskat, “Calculation of Theoretical Productivity Factor,” *Trans. AIME*, vol. 146, no. 01, pp. 126–139, Dec. 1942, doi: 10.2118/942126-G.
- [44] J. V. Vogel, “Inflow Performance Relationships for Solution-Gas Drive Wells,” *J. Pet. Technol.*, vol. 20, no. 01, pp. 83–92, Jan. 1968, doi: 10.2118/1476-PA.
- [45] R. O. Baker, H. W. Yarranton, and J. L. Jensen, “Basic Reservoir Engineering Calculations,” in *Practical Reservoir Engineering and Characterization*, Elsevier, 2015, pp. 67–92.
- [46] P. M. Bruijnen, “Nodal Analysis by Use of ESP Intake and Discharge Pressure Gauges,” *SPE Prod. Oper.*, vol. 31, no. 01, pp. 76–84, Feb. 2016, doi: 10.2118/178433-PA.
- [47] L. Jin and A. K. Wojtanowicz, “Performance Analysis of Wells With Downhole Water Loop Installation for Water Coning Control,” *J. Can. Pet. Technol.*, vol. 49, no. 06, pp. 38–45, Jun. 2010, doi: 10.2118/138402-PA.

- [48] E. . Anthony, S. . Elaila, N. . Al-Maqsseed, and M. . Areekat, “Inverted ESP Changing the Game in Water Coning Control in Water Drive Reservoirs - North Kuwait Case Study,” Oct. 2017, doi: 10.2118/187292-MS.
- [49] C. . Staveley *et al.*, “Development and Field Application of a Permanent Fiberoptic Wellbore Fluid Level Monitoring System,” Nov. 2017, doi: 10.2118/188868-MS.
- [50] G. Feo, J. Sharma, O. Santos, W. Williams, and T. Ogunsanwo, “Multiphase Flow Characterization and Modeling Using Distributed Fiber Optic Sensors to Prevent Well Blowout,” in *Optical Sensors and Sensing Congress*, 2020, p. EM3C.5, doi: 10.1364/ES.2020.EM3C.5.
- [51] R. T. Armstrong and S. Berg, “Interfacial velocities and capillary pressure gradients during Haines jumps,” *Phys. Rev. E - Stat. Nonlinear, Soft Matter Phys.*, vol. 88, no. 4, pp. 1–9, 2013, doi: 10.1103/PhysRevE.88.043010.
- [52] J. Ekechukwu, Gerald:Sharma, “Well-Scale Demonstration of Distributed Pressure Sensing using Fiber-Optic DAS and DTS,” *Sci. Rep.*, vol. (Under Rev, 2021.
- [53] J. H. Friedman, “machine.,” *Ann. Stat.*, vol. 29, no. 5, pp. 1189–1232, Oct. 2001, doi: 10.1214/aos/1013203451.
- [54] J. H. Friedman, “Stochastic gradient boosting,” *Comput. Stat. Data Anal.*, vol. 38, no. 4, pp. 367–378, Feb. 2002, doi: 10.1016/S0167-9473(01)00065-2.
- [55] T. Chen and C. Guestrin, “XGBoost,” in *Proceedings of the 22nd ACM SIGKDD International Conference on Knowledge Discovery and Data Mining*, Aug. 2016, pp. 785–794, doi: 10.1145/2939672.2939785.
- [56] C. Cortes and V. Vapnik, “Support-vector networks,” *Mach. Learn.*, vol. 20, no. 3, pp. 273–297, Sep. 1995, doi: 10.1007/BF00994018.
- [57] V. Vapnik, *The Nature of Statistical Learning Theory*. New York: Springer, 1995.
- [58] W. S. McCulloch and W. Pitts, “A logical calculus of the ideas immanent in nervous activity,” *Bull. Math. Biophys.*, vol. 5, no. 4, pp. 115–133, Dec. 1943, doi: 10.1007/BF02478259.
- [59] J. Schmidhuber, “Deep learning in neural networks: An overview,” *Neural Networks*, vol. 61, pp. 85–117, Jan. 2015, doi: 10.1016/j.neunet.2014.09.003.

- [60] L. Breiman, “Random Forests,” *Mach. Learn.*, vol. 45, pp. 5–32, 2001.
- [61] L. Breiman, J. H. Friedman, R. A. Olshen, and C. J. Stone, *Classification And Regression Trees*. Routledge, 2017.
- [62] L. Chandrasekar and G. Durga, “Implementation of Hough Transform for image processing applications,” in *2014 International Conference on Communication and Signal Processing*, Apr. 2014, pp. 843–847, doi: 10.1109/ICCSP.2014.6949962.
- [63] G. K. Ekechukwu and J. Sharma, “Automated Detection and Quantification of Gas Influx Velocity in Wellbore from Fiber-Optic Sensor Data,” in *OSA Optical Sensors and Sensing Congress 2021 (AIS, FTS, HISE, SENSORS, ES)*, 2021, p. JTh6A.11, doi: 10.1364/AIS.2021.JTh6A.11.
- [64] G. Feo, J. Sharma, D. Kortukov, W. Williams, and T. Ogunsanwo, “Distributed Fiber Optic Sensing for Real-Time Monitoring of Gas in Riser during Offshore Drilling,” *Sensors*, vol. 20, no. 1, p. 267, Jan. 2020, doi: 10.3390/s20010267.
- [65] J. Sharma, O. L. A. Santos, G. Feo, O. Ogunsanwo, and W. Williams, “Well-scale multiphase flow characterization and validation using distributed fiber-optic sensors for gas kick monitoring,” *Opt. Express*, vol. 28, no. 26, p. 38773, Dec. 2020, doi: 10.1364/OE.404981.
- [66] A. Bukhamsin and R. Horne, “Cointerpretation of Distributed Acoustic and Temperature Sensing for Improved Smart Well Inflow Profiling,” May 2016, doi: 10.2118/180465-MS.
- [67] M. F. Silva, K. M. Muradov, and D. R. Davies, “Review, Analysis and Comparison of Intelligent Well Monitoring Systems,” Mar. 2012, doi: 10.2118/150195-MS.
- [68] D. Dondurur, *Acquisition and Processing of Marine Seismic Data*. Elsevier, 2018.
- [69] D. Li, J. Castagna, and G. Goloshubin, “Investigation of generalized S-transform analysis windows for time-frequency analysis of seismic reflection data,” *GEOPHYSICS*, vol. 81, no. 3, pp. V235–V247, May 2016, doi: 10.1190/geo2015-0551.1.
- [70] C. G. Blount, K. E. Frieauf, B. E. Smith, D. P. Smith, M. Jaaskelainen, and C. S. Baldwin, “Improving Fiber-Optic System Reliability in Permanent Installations,” Sep. 2015, doi: 10.2118/174928-MS.
- [71] G. Oulundsen, D. Hennessey, and M. Conroy, “Fiber for Remote Sensing: Downhole Sensing Applications Enhanced by Specialty Optical Fibers,” *Laser Focus World*, 2015.

- [72] J. A. Jay, “An Overview of Macrobending and Microbending of Optical Fibers,” *Corning*, no. December, pp. 1–21, 2010.
- [73] B. Guzowski, G. Tosik, and Z. Makiewicz, “Pressure sensor based on optical fiber with reduced coating diameter,” *Prz. Elektrotechniczny*, vol. 90, no. March, pp. 113–115, 2014, doi: 10.12915/pe.2014.11.31.
- [74] C. Wu, K. Sun, Y. Xu, S. Zhang, X. Huang, and S. Zeng, “Concrete crack detection method based on optical fiber sensing network and microbending principle,” *Saf. Sci.*, vol. 117, no. May, pp. 299–304, 2019, doi: 10.1016/j.ssci.2019.04.020.
- [75] M. Njegovec, V. Budinski, B. Macuh, and D. Donlagic, “Microbend point and distributed fiber optic corrosion sensing,” *IEEE Trans. Instrum. Meas.*, vol. 71, 2022, doi: 10.1109/TIM.2022.3203450.
- [76] Y. Zheng, W. Xiao, and Z. W. Zhu, “A simple macro-bending loss optical fiber crack sensor for the use over a large displacement range,” *Opt. Fiber Technol.*, vol. 58, no. April, p. 102280, 2020, doi: 10.1016/j.yofte.2020.102280.
- [77] L. Cheng, F. Song, K. Zhang, Y. Li, and J. Yang, “A U-shaped-wound fiber macro-bending loss crack sensor improved by an optical splitter,” *Opt. Fiber Technol.*, vol. 58, no. March, p. 102259, 2020, doi: 10.1016/j.yofte.2020.102259.
- [78] R. M. López *et al.*, “Coherent optical frequency domain reflectometry for interrogation of bend-based fiber optic hydrocarbon sensors,” *Opt. Fiber Technol.*, vol. 10, no. 1, pp. 79–90, 2004, doi: 10.1016/j.yofte.2003.09.003.
- [79] M. Roman, C. Zhu, R. J. O’Malley, R. E. Gerald, and J. Huang, “Distributed Fiber-Optic Sensing with Low Bending Loss Based on Thin-Core Fiber,” *IEEE Sens. J.*, vol. 21, no. 6, pp. 7672–7680, 2021, doi: 10.1109/JSEN.2021.3050702.
- [80] O. Santos, M. Almeida, J. Sharma, M. Kunju, Y. Chen, and P. Waltrich, “New Experimental Results Show the Application of Fiber Optic to Detect and to Track Gas Position in Marine Risers and Shed Lights on the Gas Migration Phenomenon Inside a Closed Well,” *Mar.* 2022, doi: 10.2118/208682-MS.
- [81] J. Crisp, “Introduction to fiber optics,” *Introd. to fiber Opt.*, 1998, doi: 10.1017/cbo9781139174770.
- [82] J. lamperski, “Fundamentals of Optical Fiber Technology and Systems,” *Internet-based vocational training of communication students, engineers, and technicians*. http://www.invocom.et.put.poznan.pl/~invocom/C/P1-9/swiatlowody_en/p1-1_2_2.htm.

- [83] J. Stone, A. R. Chraplyvy, and C. A. Burrus, “Gas-in-glass—a new Raman-gain medium: molecular hydrogen in solid-silica optical fibers,” *Opt. Lett.*, vol. 7, no. 6, p. 297, Jun. 1982, doi: 10.1364/OL.7.000297.
- [84] K. Noguchi, N. Shibata, N. Uesugi, K. Ishihara, and Y. Negishi, “Optical fiber loss increase due to hydrogen and long-term loss stability for optical fiber cables,” *Electron. Commun. Japan (Part II Electron.)*, vol. 69, no. 5, pp. 1–9, 1986, doi: 10.1002/ecjb.4420690501.
- [85] J. Jacobs, “The Impact of Hydrogen on Optical Fibers,” 2004.
- [86] M. A. Malik, “Dissociation of water,” 2022. [https://chem.libretexts.org/Bookshelves/Introductory_Chemistry/Introduction_to_General_Chemistry_\(Malik\)/06%3A_Acids_and_bases/6.05%3A_Dissociation_of_water#:~:text=About one water molecule in,proton to another water molecule.](https://chem.libretexts.org/Bookshelves/Introductory_Chemistry/Introduction_to_General_Chemistry_(Malik)/06%3A_Acids_and_bases/6.05%3A_Dissociation_of_water#:~:text=About one water molecule in,proton to another water molecule.)
- [87] W. Jacobsen *et al.*, “Beyond 300°C: Reliable long-term measurement of temperature for supercritical geothermal systems,” *Trans. - Geotherm. Resour. Counc.*, vol. 41, pp. 704–721, 2017.
- [88] E. A. Bonnell, “Temperature Dependent Behavior of Optical Loss from Hydrogen Species in Optical Fibers at High Temperature,” no. April, 2015.
- [89] The Fiber Optics Association, “NECA/FOA 301-2016.”
- [90] S. Palit, “Schlumberger DTS Ultra User Manual: version 2.1,” 2020.
- [91] P. Parshin, A., Hilton, G., Wallace, “Schlumberger Hyperion Operations Manual,” 2017.
- [92] Anritsu, “Understanding OTDRs,” 2011.

Vita

Gerald Ekechukwu joined the graduate program at Louisiana State University in Fall 2020 with curiosity and excitement to engage in interdisciplinary, fundamental, and original research. Gerald received his B.Sc. and M.Sc. degrees from the University of Ibadan (Nigeria) and Imperial College London (United Kingdom) in 2014 and 2017, respectively. Gerald has work experiences with ExxonMobil (Nigeria), Sterling Oil (Nigeria), and TotalEnergies (France and USA). Also, he has prior research experience at the University of Wyoming. He anticipates graduating with a Ph.D. major in Petroleum engineering and a Ph.D. minor in Electrical engineering.